



# VCU

Virginia Commonwealth University  
VCU Scholars Compass

---

Theses and Dissertations

Graduate School

---

2019

## Capillary Forces in Partially Saturated Thin Fibrous Media

Ali Moghadam

Follow this and additional works at: <https://scholarscompass.vcu.edu/etd>

 Part of the [Mechanical Engineering Commons](#), [Membrane Science Commons](#), and the [Transport Phenomena Commons](#)

© The Author

---

Downloaded from

<https://scholarscompass.vcu.edu/etd/6110>

This Dissertation is brought to you for free and open access by the Graduate School at VCU Scholars Compass. It has been accepted for inclusion in Theses and Dissertations by an authorized administrator of VCU Scholars Compass. For more information, please contact [libcompass@vcu.edu](mailto:libcompass@vcu.edu).



# **Capillary Forces in Partially Saturated Thin Fibrous Media**

A dissertation submitted in partial fulfillment of the requirements for the degree of Doctor of  
Philosophy at Virginia Commonwealth University

by

Ali Moghadam

M.S. Mechanical Engineering, University of Tehran, Iran, 2016

Director: Hooman V. Tafreshi

Professor, Department of Mechanical and Nuclear Engineering

Virginia Commonwealth University

Richmond, Virginia

December 2019

## **Dedication**

I would like to dedicate this work to my family, especially to my parents. I could not have come this far without their unconditional support.

## Acknowledgment

I wish to express my sincere thanks to Prof. Hooman V. Tafreshi, my advisor, for his continuous support, valuable guidance and encouragement throughout the course of my research. I would not have been able to finish this work without his support and unfailing faith in me.

I would also like to extend my feeling of gratitude to my Ph.D. committee members, Prof. Gary C. Tepper, Prof. Ram B. Gupta, Prof. Michael J. Cabral, and Prof. Karla M. Mossi for their insightful questions, valuable suggestions and comments which have helped strengthen my work.

I am thankful to my friends and labmates and the Costellos (Matt, Nancy and Travis) for making my life in VCU and Richmond memorable.

I would like to express my gratitude to my family for their endless support. I am thankful to my parents (Ahmad and Kheshan), my siblings (Shiva, Shahin and Shima) and brother in-laws (Reza and Hamid) for always supporting me and encouraging me to follow my dreams.

I would also like to thank the Nonwovens Institute at NC State University and VCU School of Engineering for financial support.

## Table of Contents

Dedication .....	ii
Acknowledgment .....	iii
Table of Contents .....	iv
List of Figures .....	vii
Abstract .....	x
Chapter 1. Introduction .....	1
1.1 Background information .....	1
1.1.1 Capillarity, surface tension, contact angle .....	1
1.1.2 Liquid entry pressure.....	3
1.1.3 Capillary forces between fibrous surfaces .....	5
1.2 Overall Objectives of This Thesis .....	7
Chapter 2. Characterizing nonwoven materials via realistic microstructural modeling.....	10
2.1 Introduction .....	10
2.2 Virtual fibrous media with realistic microstructures .....	12
2.3 Liquid entry pressure calculation .....	15
2.3.1 Parametric representation of fibers.....	19
2.3.2 Fiber intersection with a planar air–water interface .....	22
2.4 Results and discussion.....	25
2.5 Conclusions .....	33
Chapter 3. A new approach to modeling liquid intrusion in hydrophobic fibrous membranes with heterogeneous wettabilities.....	34

3.1 Introduction .....	34
3.2 Interface tracking: force balance vs. energy minimization .....	36
3.3 Numerical treatment of interface–interface or interface–solid interactions .....	39
3.4 Simulation method and experimental validation.....	41
3.4.1 Comparison with experiment .....	43
3.4.2 Comparison with previous 2-D simulations.....	46
3.5 Results and Discussion.....	47
3.5.1 Interface modeling in membranes with semi-ordered orthogonal parallel fibers .....	47
3.5.2 Intrusion pressure vs. penetration depth.....	52
3.6 Conclusions .....	58
Chapter 4. On liquid bridge adhesion to fibrous surfaces under normal and shear forces .....	59
4.1 Introduction .....	59
4.2 Experimental setup and materials .....	61
4.2.1 Test setup.....	61
4.2.2 Electrospinning fibrous coatings .....	62
4.3 Theoretical analysis.....	63
4.3.1 Balance of forces on a liquid bridge.....	63
4.3.2 Numerical simulation .....	65
4.4 Results and discussion.....	69
4.4.1 Liquid bridge between PS-coated horizontal plates under compression or stretching .....	69
4.4.2 Liquid bridge between PU-coated vertical plates under shear .....	79
4.5 Conclusions .....	87
Chapter 5. Overall Conclusion .....	88

Chapter 6. References .....	90
Appendix A: Vita .....	103

### List of Figures

<b>Fig. 2.1</b>	An example of our virtual fibrous structures having a fiber diameter of 10 $\mu\text{m}$ , a basis weight of 76 $\text{g}/\text{m}^2$ , and a SVF of 0.18.
<b>Fig. 2.2</b>	A schematic illustration of our mass-spring-damper model and a free body diagram for the forces acting on a single bead are shown in (a) and (b), respectively.
<b>Fig. 2.3</b>	Our curve fitting process is shown with an example where a fiber is single out and colored blue in (a). The center of mass for the beads constituting the blue fiber is shown in their original plane (b) and after transformation to the $x'$ , $y'$ , $z'$ coordinates system (c). The inset Figure in (b) is a magnified view of the curve-fit relative to the original data points.
<b>Fig. 2.4</b>	The curve-fit function representing the blue fiber of Figure 2.3a is shown in (a) as it intersects with a horizontal plane. Shown in the inset is the resulting fiber elliptical cross-sections. An example of a slicing AWI is shown in (b) along with the resulting fiber elliptical cross-sections in (c).
<b>Fig. 2.5</b>	Effects of fibers' through-plane orientation (characterized by a mean value of $\mu_{t,p} = 0$ but standard deviation ranging from $\sigma_{t,p} = 10$ to $30^\circ$ ) on SVF and LEP for media with a basis weight of 45 $\text{g}/\text{m}^2$ and a YLCA of $120^\circ$ . Two sample structures with a fiber diameter of 10 $\mu\text{m}$ but different standard deviation of $\sigma_{t,p} = 15$ , and $30^\circ$ are also shown for illustration.
<b>Fig. 2.6</b>	LEP results for media comprised of fibers with a diameter of 5 $\mu\text{m}$ but two different YLCA of 120 and $150^\circ$ are given in (a). SVF and LEP results media comprised of fibers with two different diameters of 10 and 15 $\mu\text{m}$ but a common YLCA of $120^\circ$ are given in (b). Examples of bimodal media studied in (b) are also given for better illustration.
<b>Fig. 2.7</b>	Effects of fibers' in-plane orientation (characterized by a mean value of $\mu_{i,p} = 0$ but standard deviations of $\sigma_{i,p} = 22$ and $45^\circ$ ) on SVF and LEP for media with a basis weight of 45 $\text{g}/\text{m}^2$ and a YLCA of $120^\circ$ . Also shown in this figure are two sample structures with a fiber diameter of 15 $\mu\text{m}$ but different in-plane fiber orientations.
<b>Fig. 2.8</b>	Effects of an external body force on SVF and LEP for media with a basis weight of 45 $\text{g}/\text{m}^2$ and a YLCA of $120^\circ$ . Morphology of the structures in the absence and presence of a body force (albeit chosen arbitrarily at $F = 0.012 \text{ N}/\text{kg}$ ) are also shown for comparison.
<b>Fig. 3.1</b>	Free body diagram of the forces acting on the AWI between two horizontal parallel fibers.
<b>Fig. 3.2</b>	Burst instability mechanism is shown in (a) for the AWI between fibers 3 and 4. The touch instability mechanism is shown in (b) for the interface that comes into contact with fiber 4. The coalescence instability mechanism is shown in (c) for the two interfaces meeting each other under fiber 1. Formation of an island between three and two fibers is shown in (d) and (e), respectively.
<b>Fig. 3.3</b>	Geometric variables used in Equations 3.5–3.8 are shown in (a) using a schematic drawing of the air–water interface in contact with a fiber. Modifications needed for correct non-wetting phase volume calculation in

	Surface Evolver is shown graphically in (b).
<b>Fig. 3.4</b>	The experimental setup used for validating our numerical simulation is shown in the top left figure. Average fiber diameter and fiber-to-fiber spacing are about 250 and 1000 $\mu\text{m}$ , respectively. The figures on the top right show the air–water interface at a pressure of about 320 Pa (slightly below the failure pressure) at two different magnifications. The bottom figures show the air–water interface from numerical simulation at a pressure of about 300 Pa (slightly below the failure pressure). A YLCA of about $123^\circ$ was measured experimentally and used in the simulations.
<b>Fig. 3.5</b>	Comparison between the AWIs obtained from force balance method reported in [124] (a) and the current energy method (b) for a unidirectional fibrous structure with an SVF of 0.15 and a fiber diameter of 10 $\mu\text{m}$ at an intrusion pressure 6.6 kPa. Red and black fibers have different YLCAs of $35^\circ$ and $65^\circ$ with the wetting phase ( $145^\circ$ and $115^\circ$ with the non-wetting phase), respectively.
<b>Fig. 3.6</b>	Simulation of AWI inside a structure with an SVF of 0.23, a fiber diameter of 10 $\mu\text{m}$ , and a YLCA of $150^\circ$ at different intrusion pressures from 6.5 kPa through 12.5 kPa shown in (a) through (d), respectively. The intrusion pressure vs. penetration depth simulation results are given in (e).
<b>Fig. 3.7</b>	The burst and coalescence failure mechanisms are shown in (a) and (b), respectively.
<b>Fig. 3.8</b>	Flowchart for the simulation algorithm.
<b>Fig. 3.9</b>	Simulation of AWI inside Bimodal-D structures with an SVF of 0.23 but different volume fractions of fine (10 $\mu\text{m}$ ) or coarse (20 $\mu\text{m}$ ) fibers. The YLCA of the fibers is assumed to be $120^\circ$ and the intrusion pressure is set at 5 kPa. Volume fraction of fine fibers is 50% and 25% in (a) and (b), respectively. The intrusion pressure vs. penetration depth simulation results are plotted in (c).
<b>Fig. 3.10</b>	Simulation of AWI inside Bimodal-CA structures with an SVF of 0.23 and a fiber diameter of 10 $\mu\text{m}$ but different fiber YLCAs of 150 and 120 degrees. The intrusion pressure is set at 9.5 kPa. Volume fraction of more hydrophobic fibers is 66% and 34% in (a) and (b), respectively. The intrusion pressure vs. penetration depth simulation results are given in (c).
<b>Fig. 3.11</b>	The intrusion pressure vs. penetration depth results for Bimodal-D-CA membranes with an SVF of 0.23. Simulation of AWI inside Bimodal-D-CA membranes with an SVF of 0.23 at an intrusion pressure of 7.5 kPa is shown in the inset. The structures are composed of fibers with a diameter 10 $\mu\text{m}$ and a YLCA of 150 (shown in red) and fibers with a diameter 20 $\mu\text{m}$ and a YLCA of 120 (shown in blue).
<b>Fig. 4.1</b>	Schematic drawings for the setup used for liquid bridge experiments.
<b>Fig. 4.2</b>	Schematic drawings for the setup used for polystyrene electrospinning. The inset SEM image is an example of our PS coatings comprised of orthogonally-layered fibers.
<b>Fig. 4.3</b>	Free body diagram for a liquid bridge between two horizontal plates.

<b>Fig. 4.4</b>	A virtual liquid bridge between two horizontal plates with the facets on the lower TCL shown in red.
<b>Fig. 4.5</b>	Snapshots of a liquid bridge with a volume of 2 $\mu\text{L}$ are shown at different spacing distance between two identical plates with advancing and receding CAs of 80 and 40°, respectively. Spacing between the plates, radius of the contact area, and the liquid CA are given underneath each subfigure.
<b>Fig. 4.6</b>	Surface energy of the system is given in (a). Also, shown in (a) is the R-constant and $\theta$ -constant lines. Comparison between the current numerical simulations and those from [66] are given in (b) in a force–spacing diagram.
<b>Fig. 4.7</b>	Snapshots of a liquid bridge between two horizontal plates coated with electrospun PS fibers (with advancing and receding CAs of 131° and 125°, respectively) are given in (a) along with their computational counterparts in (b) at different spacing.
<b>Fig. 4.8</b>	The measured and predicted adhesion forces on the lower plate are shown in (a). Predicted capillary and pressure forces on the lower plate are compared with one another in (b).
<b>Fig. 4.9</b>	Panel (a) shows the predicted adhesion force on the lower plate for when a liquid bridge with a volume of 7 $\mu\text{L}$ is compressed to different minimum spacing values before stretching. Panel (b) shows similar results for liquid bridge with different volumes but an identical minimum spacing of 940 $\mu\text{m}$ .
<b>Fig. 4.10</b>	Schematic drawings for the setup used for liquid bridge shear experiment.
<b>Fig. 4.11</b>	Geometrical assumptions considered in setting up a numerical simulation to predict the behavior of a liquid bridge under shear and in the presence of gravity.
<b>Fig. 4.12</b>	Snapshots of the experiment with a liquid bridge with a volume of 7 $\mu\text{L}$ between two vertical plates having a spacing of 1,400 $\mu\text{m}$ and coated with electrospun PU fibers are shown in (a). Predictions of the liquid bridge profile from our numerical simulations are given in (b) for different plate displacements.
<b>Fig. 4.13</b>	Illustration of the facets on the TCL (red) considered to find the local direction of the surface tension forces around the TCL is given in (a) along with a free body diagram for the forces acting on a liquid bridge under vertical shear. Tangential forces exerted from left and right to a liquid bridge with a volume of 7 $\mu\text{L}$ placed between two vertical plates coated with electrospun PU fibers with a spacing of 1,400 $\mu\text{m}$ are shown in (b). Shear force exerted on the left plate by a liquid bridge with a volume of 7 $\mu\text{L}$ at different spacings are shown in (c). Shear force exerted on the left plate by liquid bridges with different volumes but for a fixed spacing of 1,200 $\mu\text{m}$ between the plates are given in (d). The solid lines are the force predictions from simulations (obtained with the assumption of pinned TCL throughout the process) and the symbols are from experiment.

## **Abstract**

### Capillary Forces in Partially Saturated Thin Fibrous Media

By Ali Moghadam, Ph.D.

A dissertation submitted in partial fulfillment of the requirements for the degree of Doctor of Philosophy at Virginia Commonwealth University.

Virginia Commonwealth University, 2019

Director: Hooman V. Tafreshi  
Professor, Department of Mechanical and Nuclear Engineering

Capillarity is often exploited in self-cleaning, drag reducing and fluid absorption/storage (sanitary products) purposes just to name a few. Formulating the underlying physics of capillarity helps future design and development of optimized structures. This work reports on developing computational models to quantify the capillary pressure and capillary forces on the fibrous surfaces. To this end, the current study utilizes a novel mass-spring-damper approach to incorporate the mechanical properties of the fibers in generating virtual fibrous structures that can best represent fibrous membranes. Such virtual fibrous structures are then subjected to a pressure estimation model, developed for the first time in this work, to estimate the liquid entry pressure (LEP) for a hydrophobic fibrous membrane. As for accurate prediction (and not just estimation) of the capillary pressure, this work also presents an energy minimization method, implemented in the Surface Evolver code, for tracking the air–water interface intrusion in a hydrophobic fibrous membrane comprised of orthogonally oriented fibers. This novel interface tracking algorithm is used to investigate the effects of the membrane’s microstructure and wetting properties on its resistance to water intrusion (i.e., LEP). The simulation method developed in this work is computationally affordable and it is accurate in its predictions of the

air–water interface shape and position inside the membrane as a function of pressure. Application of the simulation method in studying effects of fiber diameter or contact angle heterogeneity on water intrusion pressure is reported for demonstration purposes.

Capillary forces between fibrous surfaces are also studied experimentally and numerically via the liquid bridge between two parallel plates coated with electrospun fibers. In the experiment, a droplet was placed on one of the polystyrene- or polyurethane-coated plates and then compressed, stretched, or sheared using the other plate and the force was measured using a sensitive scale. In the simulation, the liquid bridge was mathematically defined for the Surface Evolver finite element code to predict its 3-D shape and resistance to normal and shearing forces, respectively, in presence of the contact angle hysteresis effect. Despite the inherent non-uniformity of the fibrous surfaces used in the experiments and the simplifying assumptions considered for the simulations, reasonable agreement was observed between the experiments and simulations. Results reveal that both normal and shear force on the plates increase by increasing the liquid volume, or decreasing the spacing between the plates.

## **Chapter 1. Introduction**

### **1.1 Background information**

Capillarity is the driving force that plays an important role in the displacement of one fluid (e.g., air) by another (e.g., water) at the microscale in a porous media. Two important measure of capillarity are the capillary pressure and capillary force. Materials with positive capillary pressure are hydrophobic and can be used for self-cleaning or drag reducing applications [1–4] whereas materials with negative capillary pressure are hydrophilic and are more suitable for fluid absorption/storage (hygiene products) [5–10]. Capillary forces are results of surface tension forces between two immiscible fluids, as well as different interactions of the solid surfaces of the porous media with each of the fluids. Capillary force is responsible for adhesion of wet surfaces/layers to one another. Frogs and insects employ a capillary force to climb a vertical surface [11-13]. It is also of great importance in many industrial applications like printing, papermaking and atomic force microscopy [14-18].

Brief background information about surface tension, Young-Laplace contact angle, modeling capillary-controlled liquid intrusion inside a fibrous surface, and capillary (adhesion) forces between fibrous coatings are discussed in the following subsections.

#### **1.1.1 Capillarity, surface tension, contact angle**

Capillarity is the most important factor in characterizing the nature of fluid interaction with a porous material at the microscale. It is caused by the surface tension forces between the two immiscible fluids, as well as the affinity of the solid surface of the porous medium for one fluid over the other. Surface tension of a fluid-fluid interface is a fluid property which causes the

interface to shrink into a surface with the minimum surface area possible. Because of the differences between solid-liquid and solid-gas surface tensions, contact angle forms when a liquid-gas interface (LGI) intersects with a solid-liquid interface (SLI). Contact angle is the angle that the tangent to the LGI makes with tangent to the SLI at the triple phase contact line. For ideal surfaces this contact angle is referred to as intrinsic contact angle or the Young-Laplace contact angle (YLCA). Considering the balance of forces on the triple phase contact line, one can relate the contact angle to surface tension as [19,20]:

$$\cos \theta^{YL} = \frac{\sigma_{SG} - \sigma_{SL}}{\sigma_{LG}} \quad (1.1)$$

Here  $\theta^{YL}$  is the YLCA,  $\sigma_{LG}$  (also referred to as  $\sigma$ ),  $\sigma_{SG}$ , and  $\sigma_{SL}$  are the liquid-gas, solid-gas, solid-liquid surface tensions, respectively. Another important quantity in the context of capillarity is the Laplace pressure, which is the pressure difference across the liquid-fluid interface. The Laplace pressure can be related to the curvature of the liquid-fluid interface through the Young-Laplace equation:

$$\Delta p = 2\sigma H \quad (1.2)$$

here  $H$  is the interface mean curvature. In other words, the liquid-fluid interface reaches an equilibrium configuration in which capillary forces are balanced with the forces from the Laplace pressure. Young-Laplace equation subjected to different boundary conditions has attracted researchers to solve interfacial phenomenon problems [21-24].

YLCA is a material property, and determines the extent of a surface wettability and is only defined for ideal surfaces. In practice, because of the surface roughness, the contact angle that a liquid

makes with a surface departs from the ideal YLCA. The observed contact angle (with the naked eye) from imaging is called the apparent contact angle.

Surfaces with an apparent contact angle of less than  $90^\circ$  are called hydrophilic, and those with apparent contact angles of larger than  $90^\circ$  are referred to as hydrophobic. An interesting category of hydrophobic surfaces is the superhydrophobic surfaces (contact angle larger than  $150^\circ$ ), which are known for their ability to reduce the wetted area (contact area between liquid and the solid surface). The reduced contact area makes such surfaces suitable for applications such as self-cleaning, drag-reduction and anti-icing [1-4] among many others.

### **1.1.2 Liquid entry pressure**

Superhydrophobic surfaces are often produced by microfabrication of small roughness on a smooth surface and addition of a hydrophobic chemistry to the surface [25,26]. A cost-effective approach is via coating the smooth surface with a porous hydrophobic material, e.g., Polystyrene fibers or aerogel particles [4,27-31]. A droplet on a rough surface may exhibit two stable wetting states; Cassie (almost dry) or Wenzel (Wetted) state [32-35]. In other words, Wenzel corresponds to the state where surface asperities are completely submerged in the liquid, while Cassie represent the state where a layer of air is entrapped underneath the liquid between the peaks of the asperities [2,36-38]. The pressure at which a surface starts departing from the Cassie state is referred to as the critical pressure or the Cassie-Wenzel transition pressure [39], where the entrapped air is dissolved into water resulting in the wetting of the surface. Closely related to the concept of Cassie-Wenzel transition is the liquid entry pressure (LEP) in fibrous membranes. Fibrous membranes are alternatives to porous films for many separation applications thanks to their high porosity and mechanical strength [40–51]. When a hydrophobic fibrous membrane is in contact with water, the

hydrophobic fibers resist against water intrusion into the void space between fibers inside the membrane. When a hydrophobic fibrous membrane is submerged in water, it cannot remain dry under excessive pressures. This is because the AWI (the interface between the water outside the membrane and the air inside the membrane) becomes unstable under elevated pressures, which in turn results in water entering the pores of the membrane (i.e., the membrane's capillary pressure fails to balance the intrusion pressure) [2-3,42-43,51-52]. The pressure at which water enters the membrane is generally referred to as LEP. Understanding effects of a membrane's microstructural and wetting properties on the LEP is of great importance for engineering the next generation of fibrous membranes to ensure a maximum entry pressure while remaining highly porous.

Predicting the shape and location of the AWI inside a fibrous membrane requires solving the Young-Laplace equation. While there exist analytical and numerical solutions of the Young-Laplace equation for simple geometries such as 2-D or axisymmetric problems, it is extremely challenging to solve for a group of fibers (in the fibrous membranes) orthogonally oriented or structures comprised of randomly oriented fibers. For such cases the energy minimization method of the public domain Surface Evolver (SE) finite element code [53] is a promising alternative for solving the Young-Laplace equation and predicting the equilibrium AWI. This approach is on the basis of dividing the AWI into small triangles (called facets), and iteratively moving the nodes (vertices) of these facets to minimize the energy of the system given as:

$$E = p \iiint_V dV + \sigma \iint_{A_{LG}} dA_{LG} - \sigma \sum_{i=1}^n \cos\theta_i \iint_{A_{SL}^i} dA_{SL}^i \quad (1.3)$$

where  $p$ ,  $\sigma$ , and  $\theta_i$  are pressure difference across the AWI, surface tension, and the YLCA of fiber  $i$ , respectively. Subscripts S, L, and G refer to solid, liquid, and gas, respectively. The minimized energy of Equation 1.3 corresponds to the equilibrium air-water interface.

### 1.1.3 Capillary forces between fibrous surfaces

The wet adhesion forces (capillary forces) between two surfaces are seen in nature, e.g., frogs, insects, or geckoes create an adhesion force to climb a wall [11–13] or in building sand castles wet beach sands adhere to one another by the adhesion between sand particles [54]. Adhesion force has also industrial applications like printing, papermaking, or atomic force microscopy [14–18] just to name a few.

The capillary force between two surfaces happens with the aid of a column of liquid between them referred to as the liquid bridge. Therefore, the study of the adhesion force requires solving the Young-Laplace equation for the liquid bridge subjected to the boundary conditions on the triple contact line on each surface. There exist extensive relevant works solving Young–Laplace equation for the liquid bridge between different geometries such as flat plates, cylinders or spheres [55-63] and predicting the forces acting on the liquid bridge as a function of the spacing between the surfaces or their wetting properties. The shortcoming of all these studies is that they all assigned a single equilibrium contact angle to the liquid–air interface at the contact line. However, in practice, because of the surface roughness [64] or heterogeneity [65], a surface shows a range of contact angles (with the minimum and maximum values this range being referred to as the receding and advancing contact angles and the difference between these values being called as the contact angle hysteresis, CAH) rather than a single value. The receding contact angle is seen when the contact line is shrinking/receding, and the advancing value is seen when it is advancing/expanding. Most of the works in the literature was devoted to the case of a moving contact line with a single-valued contact angle (advancing or receding) as the boundary condition, when studying the compression or stretching of a liquid bridge between parallel plates. In other words,

the adhesion force-spacing plots were made up of a single  $\theta$ -constant line. The only work to incorporate the CAH in modeling the liquid bridge was developed by Chen et al. [66–68]. These authors used a pinned contact line boundary condition, when the contact angle was between the receding and advancing values, and a moving (unpinned) contact line boundary condition, when the contact angle had reached the advancing or receding values. As per importance of the force-spacing plots in the aforementioned applications and in understanding the state of the liquid bridge at different spacings, in this study, we employ the algorithm of [66] to describe how contact line pinning/unpinning affects the behavior of a liquid bridge between parallel plates coated with electrospun fibers during compression or stretching using  $R$ -constant (pinned TCLs) and  $\theta$ -constant (moving TCLs) lines. As will be discussed later in this work, such  $R$ -constant and  $\theta$ -constant lines are crucial components to map the compression–stretching process and to predict the fate of the liquid bridge under a compression–stretching cycle.

Another significance of the capillary forces is the tangential wet adhesion forces which can result in reducing surface friction. It is deemed that ancient Egyptians employed wet adhesion by creating capillary bridges upon pouring water on sands. Using this approach, they could reduce surface friction and move heavy statues and pyramid stones. [69]. Prediction of the tangential wet adhesion force is not a trivial task, as the solution of the Young–Laplace equation becomes challenging when the contact angle varies around the contact line due to liquid bridge profile becoming asymmetric during the shearing process. The current study is also devised to measure and predict the tangential adhesion force for the first time and to simulate shearing of the liquid bridge to better understand the forces in this process. This is done by programming the liquid contact line along with some simplifying assumptions in the Surface Evolver finite element code and solving the Young–Laplace equation via the energy minimization method.

## 1.2 Overall Objectives of This Thesis

This dissertation is intended to investigate the capillary forces/ capillary pressure in fibrous coatings. More specifically, to understand effects of surface microstructural and wetting properties on the capillary pressure (e.g., entry pressure for a liquid to penetrate a fibrous structures) as well as the capillary forces (wet adhesion forces) between fibrous surfaces. To this aim, this study consists of distinct objectives as 1) Modelling the morphology of 3-D fibrous structures comprised of soft fibers and developing an approach to estimate the entry pressure in such structures. 2) Developing a framework for modeling liquid (or air) intrusion inside a fibrous structure saturated with air (or water) to predict the entry pressure. 3) Modeling and measuring the capillary forces in the axial and tangential directions between fibrous surfaces.

First, a novel method to characterize 3-D fibrous structures with no unrealistic fiber-fiber interpenetration is developed. The idea behind structure generation in most of the previous work was adding randomly oriented rigid cylinders inside a structure until the desired solid volume fraction (i.e. ratio of solid volume to the structure volume) was obtained, which obviously the fiber-fiber overlaps were inevitable at high SVFs. The algorithm in the current study, on the other hand, does not need SVF as an input. Instead one can input the basis weight and bending rigidity and obtain the SVF and thickness as the outputs of the algorithm. The algorithm is on the basis of treating each fiber as an array of point masses interconnected to one another by springs and dampers, and is used to investigate the effects of fiber rigidity, diameters, and orientation on the SVF and thickness of the fibrous structure. The generated structures are then used to estimate the liquid entry pressure for separation membrane applications to investigate the effects of different parameters on the pressure at which water enters the membrane. This is discussed in details in

Chapter 2.

Chapter 3 reports on tracking the air–water interface (AWI) intrusion in an orthogonally-layered hydrophobic fibrous membrane via an energy minimization method, implemented in the Surface Evolver code. The developed simulation method is computationally affordable compared to methods in literature as it only considers the interface. It is accurate in its predictions of the entry pressure for heterogeneous structures, i.e. structures comprised of fibers with different wettabilities (fibers of different polymers). Furthermore, as will be discussed later in this work, the current interface tracking method is capable of simulating the breakup of interface into smaller parts as it penetrates inside a fibrous membrane. The simulation method also provides information about the relationship between intrusion pressure and depth of water penetration into the membrane which is of great significance for designing the microstructure of a fibrous membrane to maximize its LEP. The framework elaborated in Chapter 3, while addressing the AWI instabilities and breakup inside a fibrous structure could be applied to more complex structures (e.g., those generated in Chapter 2), which is beyond the scope of this study and can be investigated in a future work.

Chapter 4 investigates the capillarity of fibrous surfaces by reporting on the capillary forces between surfaces coated with electrospun polystyrene- or polyurethane fibers. This is done by studying the forces applied to a liquid bridge between surfaces both experimentally and computationally. To this aim one of the coated plates was compressed, stretched, or sheared using the other plate, and the forces applied to the plates were measured throughout the process. As for the computational component, the liquid bridge along with appropriate boundary conditions on each plate is mathematically programmed in the Surface Evolver finite element code to predict its 3-D shape and resistance to normal and shearing forces, respectively, in presence of the contact

angle hysteresis effect. In addition, the hysteresis behavior of a liquid bridge during a compression-stretching process is mapped in an energy or force diagram versus spacing between the plates using radius-constant and angle-constant lines describing the triple contact line. Finally, the overall conclusions of this dissertation are presented in Chapter 5.

## **Chapter 2. Characterizing nonwoven materials via realistic microstructural modeling**

### **2.1 Introduction**

Fibrous materials are unique in possessing three different attributes simultaneously: they are porous, they are flexible, and they are strong. For this reason, fibrous materials have been used in a variety of applications including, but not limited to, air or liquid filtration (see e.g., [70–74]), membrane separation (see e.g., [43,46,48–49]), and fluid absorbency (see e.g., [7,75–76]) to name a few. Engineering the next generation of fibrous materials for the above applications will have to rely on the ability to model the microstructure of the media and to optimize it for the specific environment of the targeted application. In the context of particle/fluid filtration modeling, the first journal publication to report the use of 3-D fibrous structures as the simulation domain was the work of Wang et al. [77] in 2006. In this work (and a series of proceeding publications focused on particle filtration [78–85], fluid absorption [86,87], or heat insulation [88,89]), the fibrous media were treated as an un-bonded web of loose fibers, in which cylindrical objects (resembling rigid fibers) were dispersed in a 3-D domain with random in-plane and/or through-plane orientations. With the size of the computational domain held constant, the number of fibers was increased incrementally to reach the desired solid volume fraction (SVF) for the virtual media. In generating such fibrous structures, one could allow the fibers to interpenetrate into one another (unrealistic of course) or prevent that by monitoring the minimum distance between the fibers during fiber generation. Overlapping fibers are not of much concerns in simulations aimed at modeling fluid, particle, or heat transfer in the space between the fibers (e.g., [77–88]), but they should not be allowed when fiber–fiber contact plays an important role, e.g., in modeling heat conduction through fibers (e.g., [90]) or mechanical strength of the material (e.g., [91–93]). In a recent

publication, a new method to create virtual fibrous structures with reduced (but not prevented) fiber–fiber overlaps and arbitrary random curvatures has been reported in [94]. Generating nonoverlapping fibrous structures using a random-walk algorithm has also been reported in [95] and used as a computational domain in some subsequent studies (e.g. [96-98]). However, resemblance of a structure created by the trajectory of a randomly moving particle to the microstructure of a real fibrous material is not immediately obvious. It is also not clear how mechanical properties of a fiber or the effects of the process by which the fibrous material is manufactured can be simulated by a random-walk-based model. It is worth mentioning that there exist some image-based approaches to obtain a realistic computational domain for fluid flow simulation in fibrous media (see e.g., [8,99-105]). However, the very basic requirement of an image-based method is that the material should exist (so that it can be imaged) before the model can be constructed, which obviously negates the whole notion of using simulation as a design tool for manufacturing new materials. The only work to report an algorithm to generate fibrous materials comprised of non-overlapping fibers with curvatures obtained from a physics-based calculation is the work of Venkateshan et al. [106]. Treating the fibers as an array of beads connected to one another with springs and dampers, these authors simulated the effects of fiber rigidity on thickness and porosity of thin electrospun coatings. In the current study, the mass-spring-damper (MSD) model of [106] is further enhanced to simulate the effects of external forces (e.g., hydrodynamic forces) on the fibers and thereby model the morphology of “bonded” nonwoven fabrics. We also use these virtual media for simulating liquid entry pressure (LEP) in fibrous membranes to demonstrate an example for the utility of such virtual media in designing real fibrous media.

In the remainder of this chapter, we first present our virtual structure generation algorithm in Section 2.2, and then move on to discuss our proposed LEP calculation method in Section 2.3. Results of our numerical simulations are presented and discussed in Section 2.4 followed by the conclusions drawn from the study in Section 2.5.

## **2.2 Virtual fibrous media with realistic microstructures**

As mentioned earlier, unlike almost all previously reported studies, the structure generation algorithm developed in this work can produce fibrous media with non-overlapping fibers (no fiber-fiber interpenetration) and with fiber curvatures obtained from a physics-based calculation method that takes the bending rigidity of the fibers into account. More specifically for the current study, we developed virtual structures by sequentially depositing fibers on top of one another and allowing the fibers to bend at the crossovers whenever needed without creating non-physical fiber-fiber overlaps (see Figure 2.1).

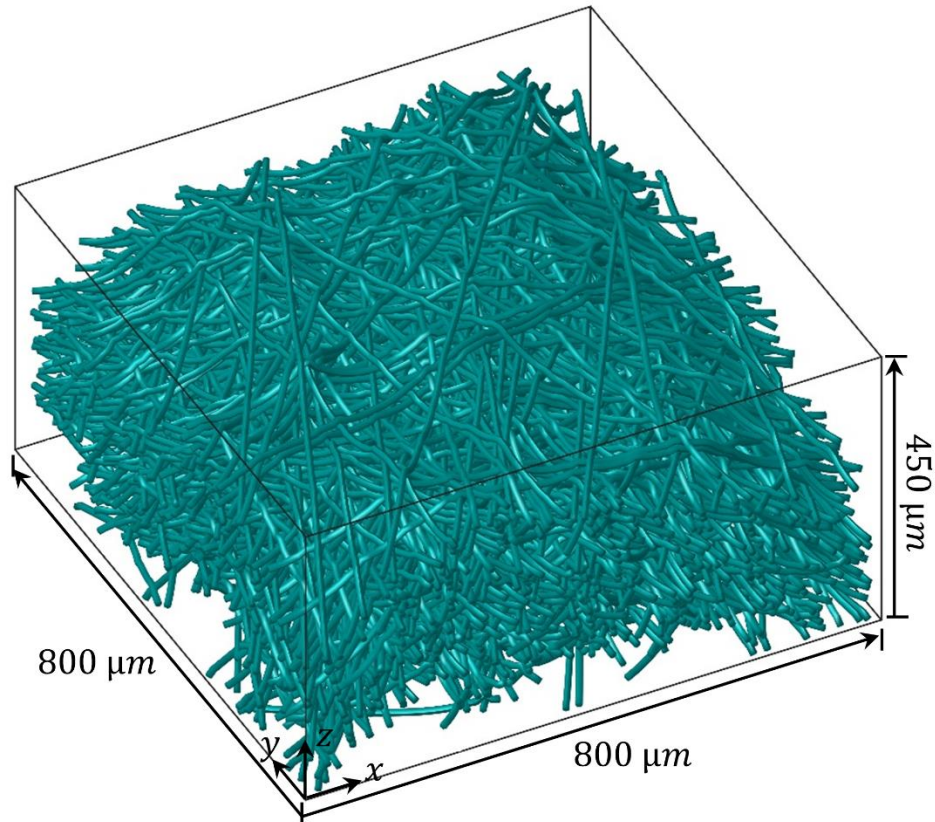


**Fig. 2.1:** An example of our virtual fibrous structures having a fiber diameter of  $10\ \mu\text{m}$ , a basis weight of  $76\ \text{g/m}^2$ , and a SVF of 0.18.

Generating such realistic-looking virtual structures was made possible by treating a fiber as a viscoelastic material, modeled as an array of beads having a diameter equal to that of the fiber and connected to one another with springs and dampers as shown in Figure 2.2a (see [106] for more details). Upon writing the balance of forces acting on each bead  $P_i$  in a fiber (see Figure 2.2b) and solving the resulting coupled system of 2<sup>nd</sup> order ordinary differential equations (ODEs) numerically, one can obtain the speed and position of the fiber.

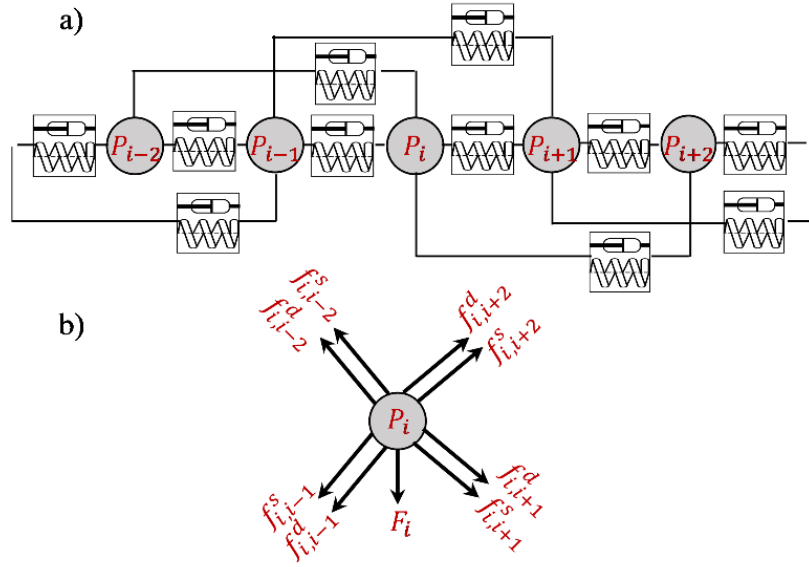


**Fig. 2.2:** A schematic illustration of our mass-spring-damper model and a free body diagram for the forces acting on a single bead are shown in (a) and (b), respectively.

To do so, each of the 2<sup>nd</sup> order ODEs is decomposed into two 1<sup>st</sup> order ODEs for the bead's position and velocity as,

$$\frac{d}{dt} \begin{bmatrix} \vec{v}_i \\ \vec{p}_i \end{bmatrix} = \begin{bmatrix} \vec{f}_i^{net} \\ m_i \vec{v}_i \end{bmatrix} \quad (2.1)$$

where  $\vec{p}_i$ ,  $\vec{v}_i$ , and  $m_i$  are position, velocity and mass of bead  $i$ , respectively.  $\vec{f}_i^{net}$  is sum of forces applied to bead  $i$ , which can be derived as,

$$\vec{f}_i^{net} = \vec{f}_{i,i-2}^s + \vec{f}_{i,i-1}^s + \vec{f}_{i,i+1}^s + \vec{f}_{i,i+2}^s + \vec{f}_{i,i-2}^d + \vec{f}_{i,i-1}^d + \vec{f}_{i,i+1}^d + \vec{f}_{i,i+2}^d - F_i \hat{e}_k \quad (2.2)$$

The damper and spring forces can be calculated as,

$$\vec{f}_{i,i+1}^d = -k_d(\vec{v}_i - \vec{v}_{i+1}) \quad (2.3)$$

$$\vec{f}_{i,i+1}^s = -k_s(\|\vec{p}_i - \vec{p}_{i+1}\| - l_r) \frac{(\vec{p}_i - \vec{p}_{i+1})}{\|\vec{p}_i - \vec{p}_{i+1}\|} \quad (2.4)$$

where  $k_d$ ,  $k_s$  are damping and spring constants, respectively, and  $l_r$  is the un-stretched length of the spring.  $F_i$  is a body force applied to each bead in the z-direction, and it can represent the forces acting on the fiber during media manufacturing (e.g., electrostatic force in electrospinning, or the aerodynamic/hydrodynamic force in nonwoven manufacturing methods like wet-laying, air-laying, melt blowing, ...). The system of ODEs given in Equation 2.1 is solved using a 4<sup>th</sup> order Runge–Kutta method with a time step of 10 ns. To ensure that the fibers do not interpenetrate as they deposit on each other, one should check whether there is a collision between the beads of a depositing fiber and those of the already deposited fibers at each time step. If the distance between two beads is less than a fiber diameter, then the beads are interpenetrating and their positions should be adjusted to remove the overlap.

In generating the virtual structures considered in this study, fibers having different orientations, characterized by their in-plane and through-plane angles, fall toward a horizontal flat substrate with an initial vertical velocity of 5 m/s. Unless otherwise stated, these angles are obtained from normal-variate random distributions with a zero mean value for the in-plane and through-plane angles ( $\mu_{i,p} = 0$  and  $\mu_{t,p} = 0$ ). Also, the standard deviation is taken to be 45° for the in-plane and 10° for the through-plane angles ( $\sigma_{i,p} = 45^\circ$  and  $\sigma_{t,p} = 10^\circ$ ). The computational domain generated with the abovementioned approach can be composed of fibers of the same or different contact angles (or diameters) which corresponds to unimodal and multi-modal media. The present study considers only unimodal and bimodal fibrous media for the sake of brevity.

### **2.3 Liquid entry pressure calculation**

Capillary pressure or capillarity is often used as a measure of a material's tendency to absorb, repel, or retain a body of fluid. Capillarity is the driving force behind immiscible fluids (e.g., air

and water) replacing one another in a fibrous material and was first formulated using the Lucas–Washburn (LW) equation [107,108]. Typical Lucas–Washburn models treat a porous medium as groups of parallel cylindrical pores having a single Young–Laplace contact angle (YLCA) [109-111]. This is a crude approximation, as there is actually no cylindrical pore in a 3-D fibrous structure (and the fibers may have different YLCAs) and so such approaches have been criticized in the literature [109-113]. Accurate alternatives to LW models for fluid transport prediction in a porous material are the Lattice Boltzmann (LB) [114,115] and the Volume of Fluid (VOF) methods [116-118]. Both LB and VOF are numerical methods to solve the partial differential equations (PDEs) describing the flow of immiscible fluids in a porous medium (time-dependent 3-D two-phase flow calculations). The obvious shortcoming of the LB and VOF simulations is their prohibitively expensive computational time, even with the current high-speed CPUs. A breakthrough in developing affordable (CPU-friendly) 3-D fluid flow simulations in porous media was the development of the Full Morphology (FM) method in which a quasi-static distribution of wetting and non-wetting phases in a 3-D domain was obtained via a purely geometric approach [119-121]. FM relies on a sphere-caging algorithm to relate the size of the largest sphere that can fit into the void space between the fibers at any point in the 3-D domain to a fictitious capillary pressure obtained from the Young–Laplace equation written for a capillary tube. By marking the fraction of the total void space that is made up of “pores” of certain diameter, the FM method obtains a capillary pressure–moisture content relationship for the whole medium [8,86-87,100,122]. Using the FM method, one can find a moisture content fraction for a given capillary pressure by dividing the volume made up of the spheres of a certain diameter (corresponding to the given capillary pressure) by the total void volume in the structure. Repeating this procedure for different pressures, one can obtain a capillary pressure–moisture relationship for porous media

[8,86-87,100,122]. Despite its very desirable CPU time, the FM method is a geometry-based approximate method that ignores the actual wetting properties (i.e., contact angle) of the fibers constituting the media. This is in contrast to the physics-based air–water interface (AWI) tracking method of [123-125] where formation, breakup, and coalescence of AWI inside fibrous structures comprised of parallel or orthogonal fibers with heterogeneous contact angles were simulated realistically. Unfortunately, however, generalizing the model of [123-125] to fibrous structures comprised of fibers with random orientations or curvatures is a very formidable task. The approach considered in the current work is an approximate method that can be used to obtain some insight into the capillarity of a fibrous medium comprised of fibers with different contact angles or complex morphology, where the other methods are not applicable or become computationally expensive. For simplification, we ignore the actual shape (or the breakup) of the AWI inside the media i.e., we assume a planar AWI for the penetrating fluid front. We calculate local capillary pressures at different horizontal planes slicing the media at different depths (scanning the entire thickness of the media) and consider the largest pressure as an estimate of the LEP for that specific structure. We start by assuming that the medium is initially filled with air (wetting phase). The medium is then put into contact with a fictitious reservoir of pressurized water such that water can penetrate into the medium and fill the pores with a capillary pressure smaller than the intrusion (reservoir) pressure. Increasing the intrusion pressure incrementally, water eventually replaces the air in the medium. As was mentioned earlier, we assume the AWI to be planar in this work to simplify an otherwise challenging computational task. In reality, the AWI conforms to a three-dimensional shape around an inclined (or vertical) fiber, and our assumption of planar AWI is merely a simplification considered to ease the LEP calculation in fibrous geometries with disordered 3-D structures. We consider symmetric boundary conditions for the sides of our

computational domain (all having fixed in-plane dimensions of  $800 \times 800 \mu\text{m}$  but a thickness ranging from 250 to 550  $\mu\text{m}$  depending on the inputs used for the structure generation) for its simplicity. Clearly, there is no plane of symmetry in a real fibrous medium having disordered fibers. However, if the in-plane size of the simulation domain is large and the simulations are repeated over an ensemble of statistically identical structures, one can significantly reduce (or eliminate) the edge effect error in the results (see [86-90]). Considering the balance of forces acting on a planar AWI inside a fibrous structure, one expects the capillary forces from the fibers to balance the intrusion force at the equilibrium [122-125], i.e.,

$$\sum_{i=1}^n F_i = p(A - \sum_{i=1}^n A_i) \quad (2.5)$$

where the right-hand side is the force caused by the intrusion pressure, and the left-hand side is the summation of the vertical components of the capillary force provided by the fibers. In a recent study, Raufaste and Cox [126] investigated deformation of the AWI by an inclined fiber for different values of inclination and YLCAs. They concluded that the net force on an inclined fiber is in the vertical direction and its magnitude is obtained by

$$F = \frac{\sigma \pi d \cos \theta}{\cos \alpha} \quad (2.6)$$

where  $\sigma$ ,  $d$ ,  $\theta$  and  $\alpha$  are surface tension, fiber diameter, YLCA, and inclination angle (the angle between the fiber and the  $z$ -axis), respectively. Substituting Equation 2.6 into Equation 2.5, one can obtain an expression for the intrusion pressure as,

$$p = \frac{\sigma \pi \sum_{i=1}^n \frac{d_i \cos(\theta_i)}{\cos(\alpha_i)}}{A - \sum_{i=1}^n A_i} \quad (2.7)$$

Here  $\alpha_i$  and  $A_i$  are the local inclination angle with the  $z$ -axis and the inclined cross-sectional area of fiber  $i$ . To obtain  $\alpha_i$  and  $A_i$  for each and every fiber in the domain, we have developed a unique

algorithm as described in the next subsection. Note that, as can be seen in Equation 2.7, fibers with an inclination angle of  $\alpha_i = 90^\circ$  (fibers lying perfectly in one horizontal plane across the entire simulation domain) cannot be handled with the method proposed here. Given the curvature of the fibers however, this happens very seldom (see Figure 2.1).

### 2.3.1 Parametric representation of fibers

Consider an individual fiber in a medium as shown in Figure 2.3a (a fiber near the top for better illustration). The center of mass positions for the beads constituting this fiber are shown in Figure 2.3b. Our strategy to obtain  $\alpha_i$  and  $A_i$  is to produce an accurate curve fit to these points so that the centerline of the fiber can mathematically be presented in a 3-D Cartesian coordinates system. Repeating this procedure to have the shape of every fiber in the domain represented by an equation, it is then easy to obtain  $i$  and  $A_i$  for each fiber by intersecting that fiber with a horizontal plane. In generating our fibrous structures, fibers enter the simulation domain as straight cylinders but they bend upon depositing on the fibers below them. Therefore, the fibers in the resulting mats do not have any significant horizontal curvatures (main curvatures are in vertical planes) as can be seen in Figure 2.3b. The plane of each fiber however, is different from that of the others. Unit normal vector of these planes can be obtained from a vector product of any two non-parallel vectors made using any of the beads on that fiber, i.e.,

$$\hat{n} = \frac{\vec{v}_1 \times \vec{v}_2}{\|\vec{v}_1 \times \vec{v}_2\|} \quad (2.8)$$

where  $\vec{v}_1$  and  $\vec{v}_2$  are two non-parallel vectors. The fiber in this plane can mathematically be presented as  $z = z(x, y)$ . To further simplify the curve fitting process, we rotate the fiber data points around some vertical axis on that plane so that the transformed points will be in an  $y' = \text{const.}$  plane, as shown with a green plane in Figure 2.3c (having a unit normal vector of  $\hat{m} =$

(0,1,0)). The axis of this rotation must exist in both the red and green planes, and it should be perpendicular to the normal unit vectors of both planes  $\hat{n}$  and  $\hat{m}$ , respectively, i.e.,  $\hat{u} = \hat{n} \times \hat{m}$ . The angle of rotation  $\phi$  can be obtained from  $\phi = \arccos(\hat{n} \cdot \hat{m})$ . Knowing the axis, and the angle of rotation, the transformation matrix can be defined as:

$$R_{\hat{u}}(\phi) = \begin{bmatrix} u_1 u_1 (1 - \cos \phi) + \cos \phi & u_1 u_2 (1 - \cos \phi) - u_3 \sin \phi & u_1 u_3 (1 - \cos \phi) + u_2 \sin \phi \\ u_2 u_1 (1 - \cos \phi) + u_3 \sin \phi & u_2 u_2 (1 - \cos \phi) + \cos \phi & u_2 u_3 (1 - \cos \phi) - u_1 \sin \phi \\ u_3 u_1 (1 - \cos \phi) - u_2 \sin \phi & u_3 u_2 (1 - \cos \phi) + u_1 \sin \phi & u_3 u_3 (1 - \cos \phi) + \cos \phi \end{bmatrix} \quad (2.9)$$

where  $u_1$ ,  $u_2$ , and  $u_3$  are the  $x$ ,  $y$ , and  $z$  components of vector  $\hat{u}$ , respectively. For instance, for the special case of rotation around the  $x$ -axis, one can simply substitute the unit vector ( $u_1 = 1, u_2 = 0, u_3 = 0$ ) in Equation 2.9.

Following this procedure, the coordinates of the beads along the fiber will be in the form of  $(x', \text{const}, z')$  after the transformation, and so the curve fitting process will be in the form of  $z' = z'(x', \text{const})$ . We then curve fit a multi-term Sine function to the transformed data points  $x'$  and  $z'$  (see Figure 2.3c), as,

$$z' = \sum_{i=1}^8 a_i \sin(b_i x' + c_i) \quad (2.10)$$

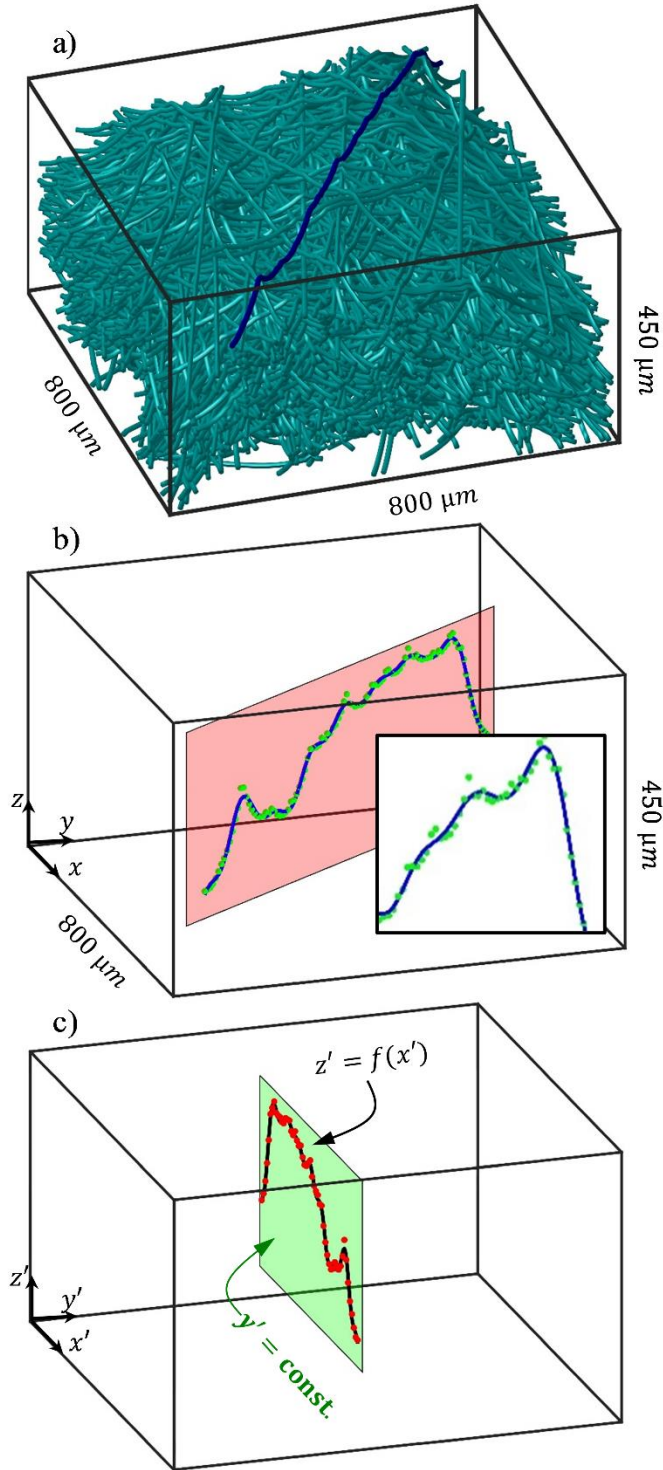


**Fig. 2.3:** Our curve fitting process is shown with an example where a fiber is single out and colored blue in (a). The center of mass for the beads constituting the blue fiber is shown in their original plane (b) and after transformation to the  $x'$ ,  $y'$ ,  $z'$  coordinates system (c). The inset Figure in (b) is a magnified view of the curve-fit relative to the original data points.

where  $a_i$ ,  $b_i$ , and  $c_i$  with  $i = 1, \dots, 8$  are coefficients of the curve fit equation. The coordinates of the rotated points are in forms of  $(x', \text{const}, \sum_{i=1}^8 a_i \sin(b_i x' + c_i))$ . With the curve fitting task completed, one has to rotate the data back to the original plane, using an inverse transformation matrix. This produces the points in a parametric form of  $x = x(x')$ ,  $y = y(x')$ ,  $z = z(x')$ , i.e.,

$$\begin{bmatrix} x \\ y \\ z \end{bmatrix} = R_{\hat{u}}^{-1}(\phi) \begin{bmatrix} x' \\ \text{const} \\ \sum_{i=1}^8 a_i \sin(b_i x' + c_i) \end{bmatrix} \quad (2.11)$$

This parametric curve can now serve as a curve fit to the fiber in the original red plane (Figure 2.3b).

### 2.3.2 Fiber intersection with a planar air–water interface

With each and every fiber presented mathematically, it is now easy to intersect them with different horizontal planes (planar AWIs corresponding to different horizontal sections in the media) to obtain  $\alpha_i$  and  $A_i$  for Equation 2.7. Intersecting the fibers with a horizontal plane  $z(x') - z_0 = 0$  is in fact a root finding exercise which can be performed using a built-in function (e.g., *fzero* command) in MATLAB. The Newton–Raphson-based root finding methods such as *fzero* require an initial guess at the location of the root. We used the minimum  $x$ -coordinate of the points constituting the fiber as our initial guess. However, since a typical fiber can have more than one intersection point with the slicing plane, our initial guess was incrementally moved along the length of the fiber, and the root finding procedure was repeated in every step to find all possible intersection points. Once all the roots were found, those outside the computational domain (or those recorded more than once) were discarded. The  $x'$  roots from solving  $z(x') - z_0 = 0$  were then substituted in Equation 2.11, to calculate the  $x$ – $y$  coordinates of the intersection points

between the fiber and the plane. For instance, consider the blue fiber shown in Figure 2.3a. This fiber intersects with the  $z = 405 \mu\text{m}$  plane at four points (see Figure 2.4a) with the elliptical cross-sections as shown in the magnified inset in Figure 2.4a. Dimensions of these ellipses were obtained by knowing the local inclination angle of the fiber at the intersection point (i.e., the angle between the  $z$ -axis and the tangent to the fiber at the intersection point). The tangent unit vector for a fiber represented in the parametric form of  $\vec{r}(x') = (x(x'), y(x'), z(x'))$  can be obtained as,

$$\hat{t}(x') = \frac{\vec{r}'(x')}{\|\vec{r}'(x')\|} \quad (2.12)$$

Substituting the  $x'$  roots in Equation 2.12, one can find the local inclination angle of the fiber from  $\alpha_i = \text{acos}(\hat{t} \cdot \hat{e}_k)$ , where  $\hat{e}_k$  is the unit vector in the  $z$ -direction. With this information, the major axis, minor axis, and the area of the elliptical cross-sections can be obtained as  $a_i = d_i / \cos \alpha_i$ ,  $b_i = d_i$ , and  $A_i = \pi a_i b_i / 4$ , respectively (see Figures 2.4b and 2.4c). The sum of  $A_i$  obtained for each intersecting fiber was then used to estimate the intrusion pressure.

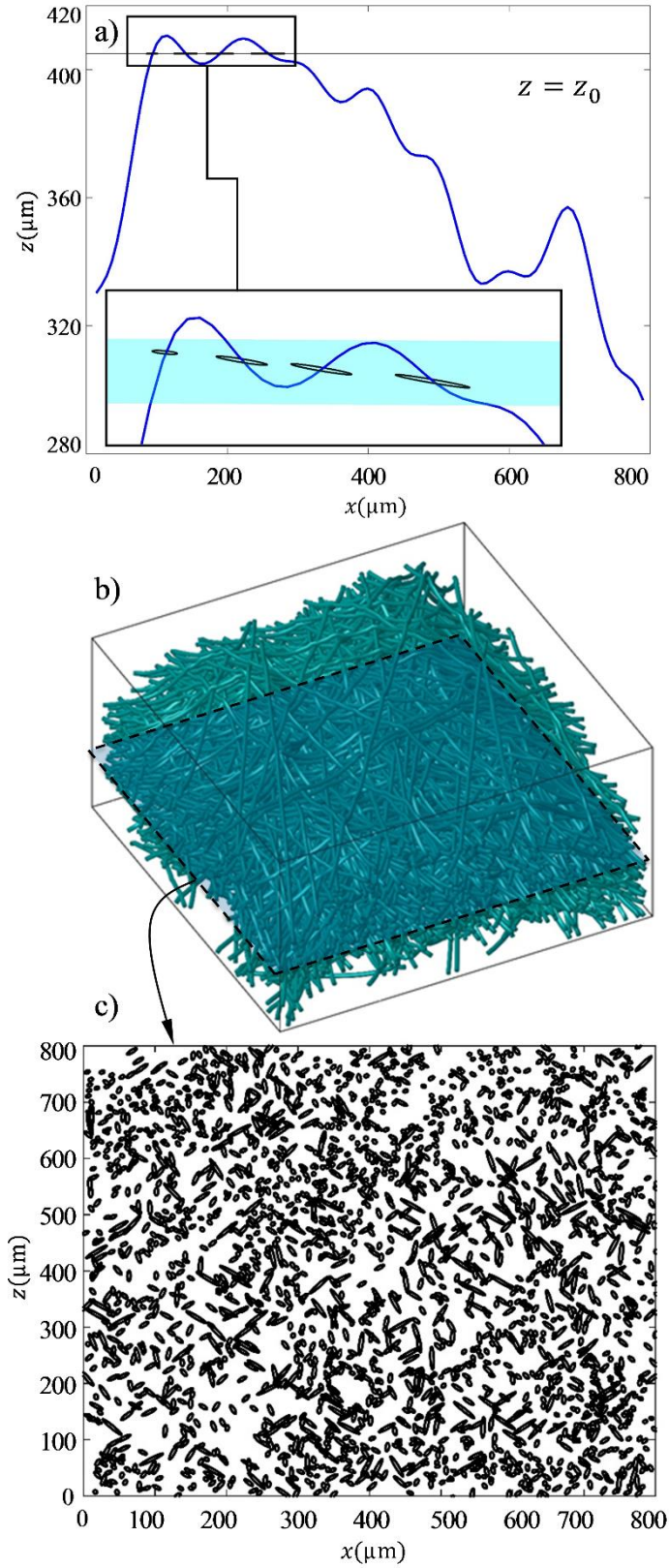


**Fig. 2.4:** The curve-fit function representing the blue fiber of Figure 2.3a is shown in (a) as it intersects with a horizontal plane. Shown in the inset is the resulting fiber elliptical cross-sections. An example of a slicing AWI is shown in (b) along with the resulting fiber elliptical cross-sections in (c).

As mentioned earlier, to find the LEP for each structure, we cut the structure with horizontal planes of different z-levels, and calculate an average pressure at each plane using Equation 2.7. The maximum pressure obtained from this calculation corresponds to the plane with highest number of fiber intersections, and hence, smallest planar pore area. For simplicity, we refer to this pressure as the LEP for that structure.

## 2.4 Results and discussion

In this section, we study the effects of fiber diameter and contact angle heterogeneity on LEP as an example of the enabling capabilities provided by our structure generation algorithm. For all simulations reported in this chapter, an in-plane domain size of  $800 \mu\text{m} \times 800 \mu\text{m}$  was considered. An initial fiber deposition velocity of 5 m/s as well as spring and damping constant of  $k_s/m_i = 2 \times 10^{10} \frac{\text{N}}{\text{m.kg}}$  and  $k_d/m_i = 5 \times 10^6 \frac{\text{N.s}}{\text{m.kg}}$  are also arbitrarily chosen for this study. Each data point reported in this study represents an ensemble of no less than three statistically identical simulations. An example of such simulations is given in Figure 2.5 where effects of through-plane angle on SVF and LEP are presented for media with different fiber diameters but a basis weight of  $45 \text{ g/m}^2$ . Note that a unique feature of the simulation method presented being a required input, which has been the case for all previous structure generation algorithms (e.g., [80-89]). It is interesting to note in Figure 2.5 that both the LEP and SVF decrease with increasing the fiber diameter. This counterintuitive result is due to the ability of the fibers to deform (bend) during the deposition process (fine fibers are softer and so they bend more). Figure 2.5 also shows that decreasing fibers' through-plane angle results in a denser structure leading to a higher LEP. This is because at higher SVFs, the "pores" in the media are smaller and so a higher intrusion pressure is required for the AWI to penetrate into the structure. In other words, a higher SVF generally

translates to a larger number of fiber–AWI intersections, and so a greater capillary force. For illustration purposes, two sample fibrous structures having an identical basis weight of  $45 \text{ g/m}^2$  and a fiber diameter of  $10 \text{ }\mu\text{m}$  but different random through-plane angles are also shown in Figure 2.5. Through-plane angles in both structures are characterized by zero mean value ( $\mu_{t,p} = 0$ ), but different standard deviation of  $\sigma_{t,p} = 15$  and  $30^\circ$ .

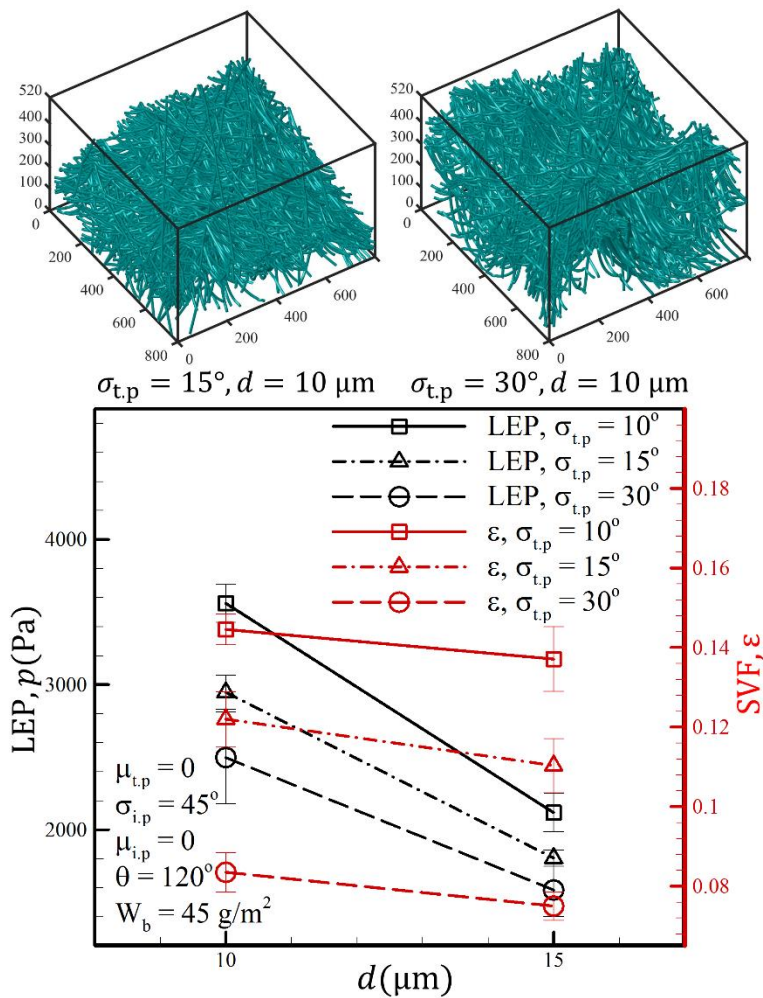


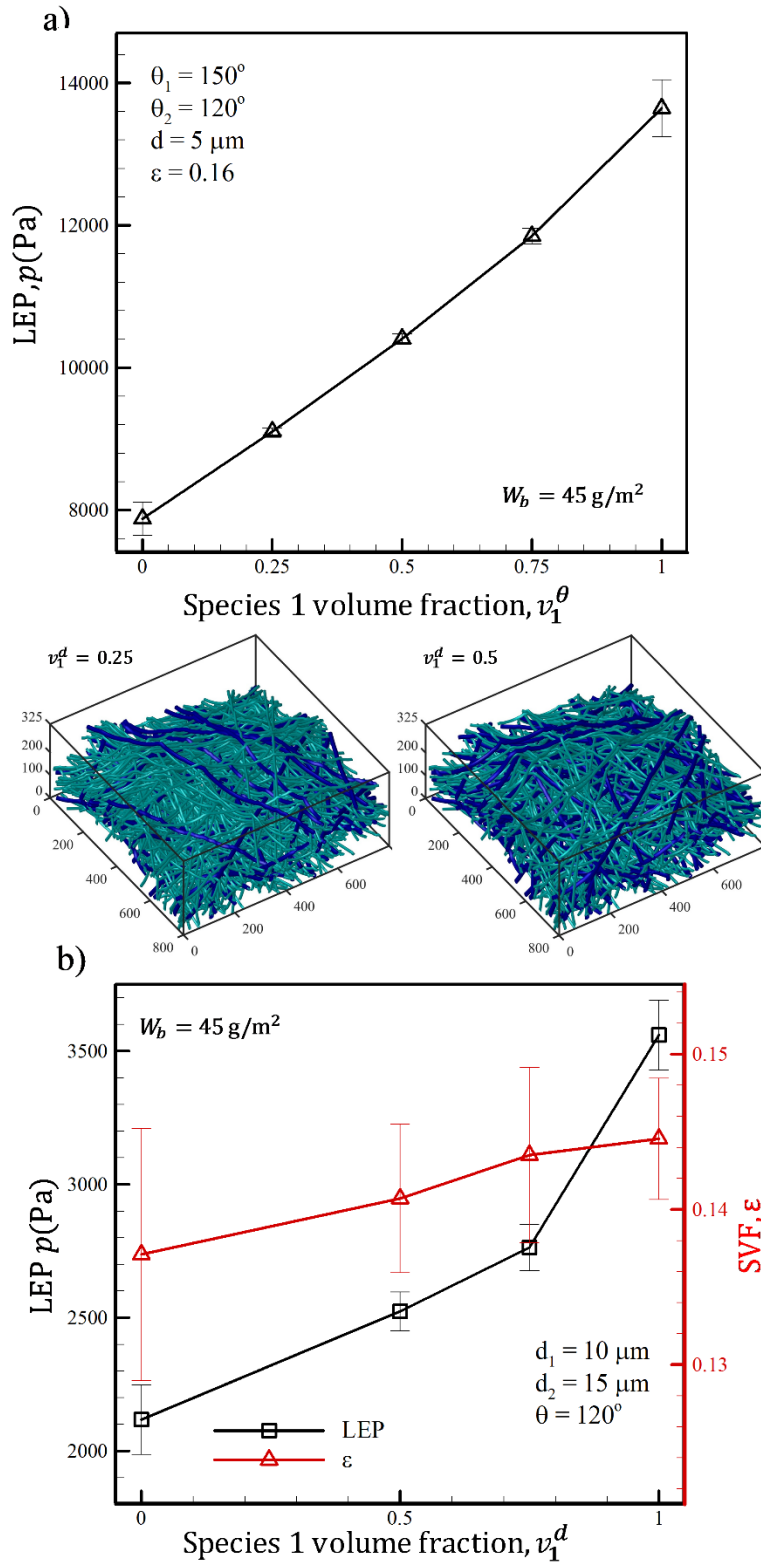
**Fig. 2.5:** Effects of fibers' through-plane orientation (characterized by a mean value of  $\mu_{t,p} = 0$  but standard deviation ranging from  $\sigma_{t,p} = 10$  to  $30^\circ$ ) on SVF and LEP for media with a basis weight of  $45 \text{ g/m}^2$  and a YLCA of  $120^\circ$ . Two sample structures with a fiber diameter of  $10 \text{ }\mu\text{m}$  but different standard deviation of  $\sigma_{t,p} = 15$ , and  $30^\circ$  are also shown for illustration.

Effects of contact angle heterogeneity (e.g., media made of different polymers) on LEP are also investigated in this study. For the sake of brevity, we only consider media with only two different YLCAs (bimodal media) but there is no limit on the number of YLCAs that can be considered. Figure 2.6a presents LEP for media with an SVF of  $\epsilon = 0.16$  and a fiber diameter of  $d_1 = 5 \mu\text{m}$ , but two different YLCAs of  $\theta_1 = 150^\circ$  and  $\theta_2 = 120^\circ$  randomly assigned to the fibers. It can be seen that intrusion pressure increases with increasing the volume fraction of the more hydrophobic fibers (denoted with  $v_1^\theta$ ). This is because more hydrophobic fibers have less affinity to water and a higher pressure is needed for the water to penetrate into membranes composed of such fibers (see also Equation 2.7). It is interesting to note that the data shown in Figure 2.6a can all be derived from a single point if the pressure values are divided by a scaling factor obtained by weight averaging the cosines of the YLCAs. i.e.,

$$p = p_1 f_p \quad (2.13)$$

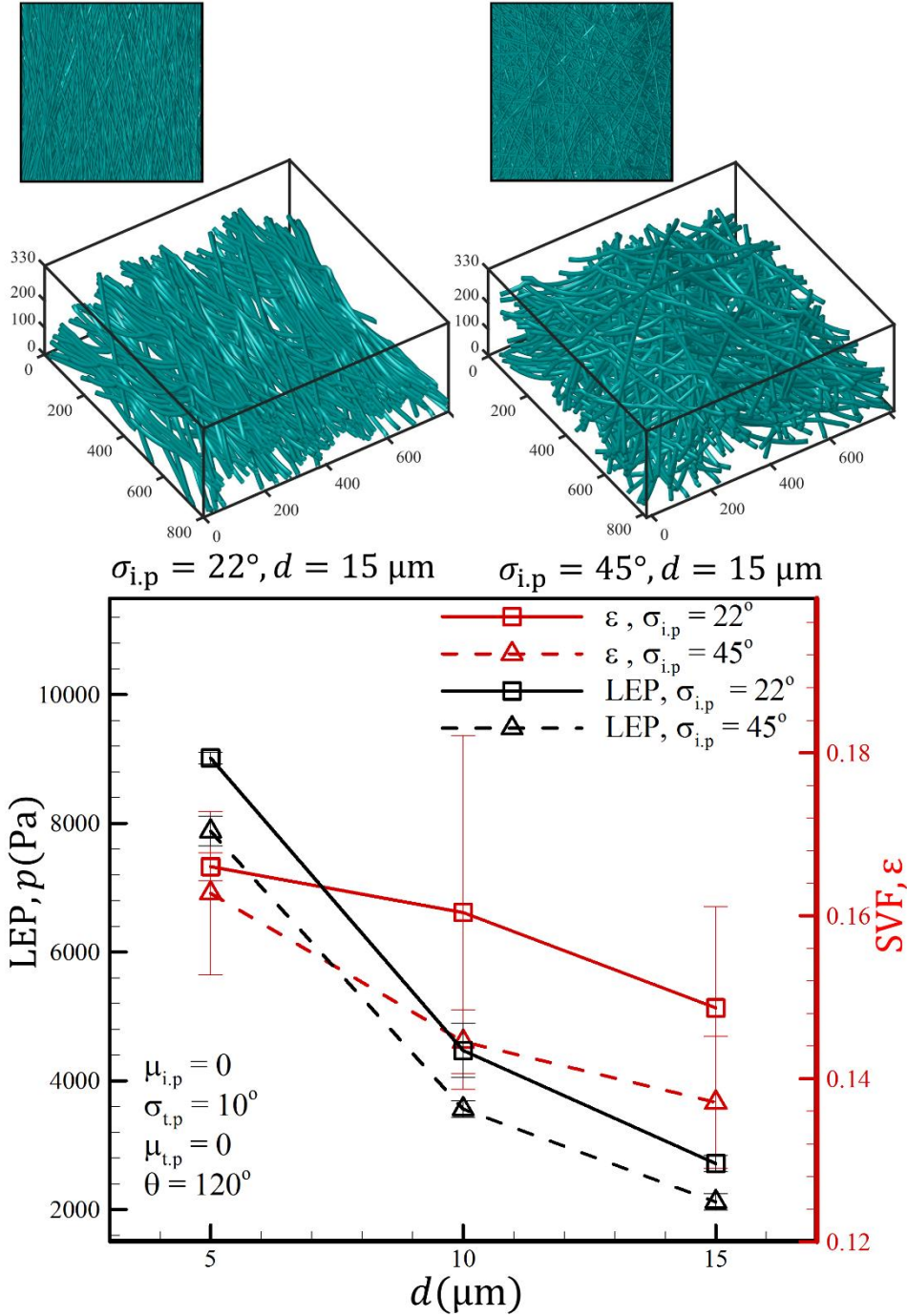
with  $f_p = v_1^\theta + (1 - v_1^\theta) \frac{\cos\theta_2}{\cos\theta_1}$ . In this equation,  $p$  is the LEP of the bimodal structure having a species-1 volume fraction  $v_1^\theta$ , and  $p_1$  is the capillary pressure of the same structure but when  $v_1^\theta = 1$ . This indicates that one can scale the LEP obtained for a given membrane with a single YLCA to estimate an LEP for media composed of fibers with the same fiber diameter but different YLCAs. It should however be noted that, the above simple scaling rule was achieved only after approximating the AWI as a planar interface which remains intact as it penetrates into the structure (see [124,125] for more discussion on AWI breakup in fibrous media). To generate virtual structures comprised of intimately blended fibers of different diameters (here bimodal for simplicity), we first estimate the number of randomly oriented fine and coarse fibers that are required to satisfy the desired basis weight and species volume fractions. We then deposit the fibers with the right diameter successively. Examples of media with bimodal diameters (10 and 15  $\mu\text{m}$ )

but different volume fractions are shown in Figure 2.6b. This figure also presents simulation results obtained for media with a basis weight of  $45 \text{ g/m}^2$ , comprised of fibers with a YLCA of  $\theta = 120^\circ$ . As expected, LEP is higher for media with larger volume fractions of fine fibers (denoted with  $v_1^d$ ). This is because fine fibers tend to bend more at fiber–fiber crossovers resulting in media with higher SVFs and consequently higher LEPs, as discussed earlier (see also Equation 2.7).



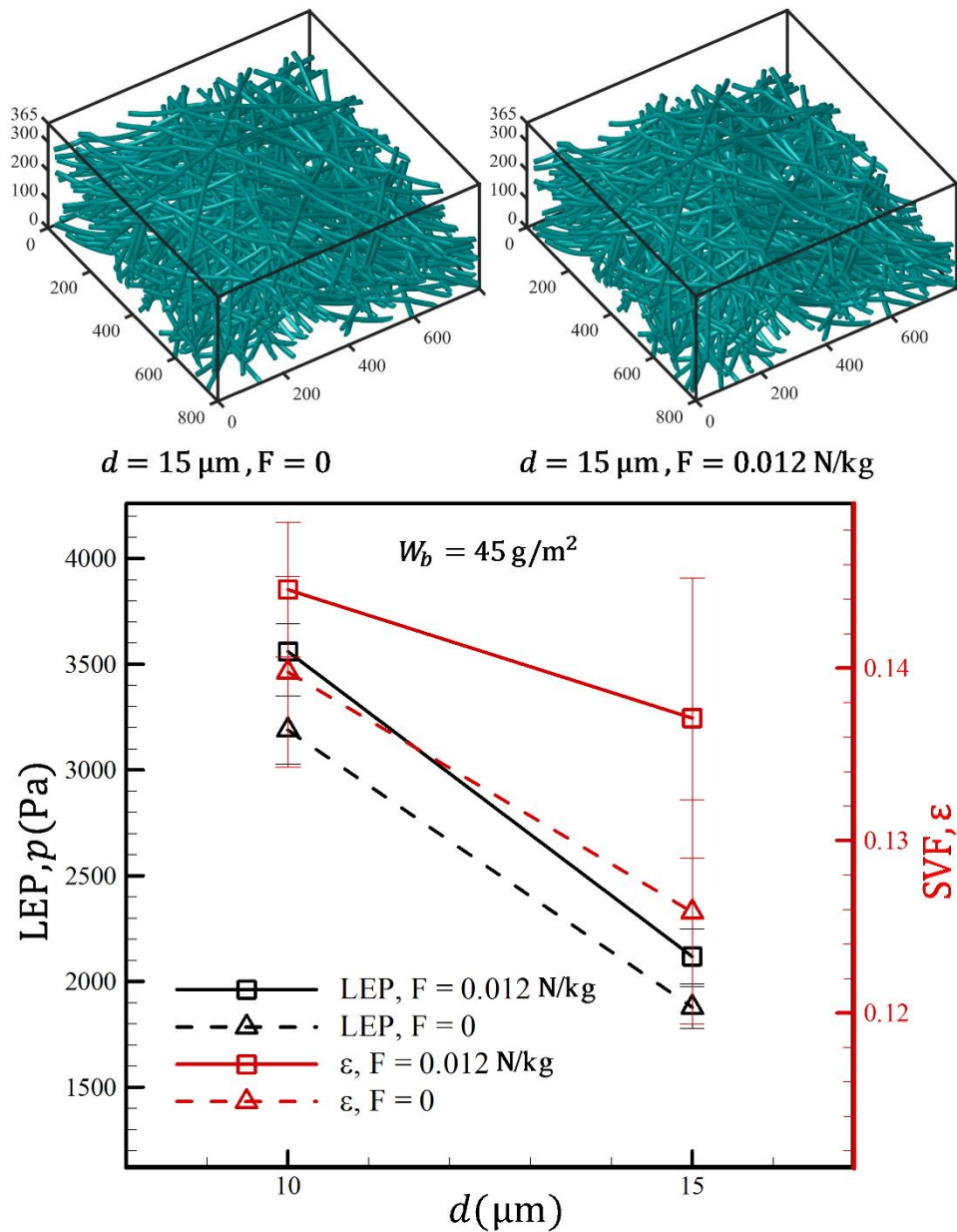
**Fig. 2.6:** LEP results for media comprised of fibers with a diameter of  $5 \mu\text{m}$  but two different YLCA of  $120$  and  $150^\circ$  are given in (a). SVF and LEP results media comprised of fibers with two different diameters of  $10$  and  $15 \mu\text{m}$  but a common YLCA of  $120^\circ$  are given in (b). Examples of bimodal media studied in (b) are also given for better illustration.

Figure 2.7 shows the effects of in-plane angle on LEP and SVF for structures of different diameters. It can be seen that decreasing fibers' in-plane angle increases the SVF of the resulting structure as fibers can better pack in each layer, and this in turn increases the LEP of the media. Examples of such media are given in Figure 2.7 for better illustration. As mentioned earlier, our structure generation algorithm can also incorporate the presence of additional forces acting on the fibers during deposition. These forces can resemble the air/water drag force on fibers during manufacturing (e.g., in air-laying, melt-blowing, or wet-laying processes) or electrostatic attraction force in electrospinning process, to name a few.



**Fig. 2.7:** Effects of fibers' in-plane orientation (characterized by a mean value of  $\mu_{i,p} = 0$  but standard deviations of  $\sigma_{i,p} = 22$  and  $45^\circ$ ) on SVF and LEP for media with a basis weight of  $45 \text{ g/m}^2$  and a YLCA of  $120^\circ$ . Also shown in this figure are two sample structures with a fiber diameter of  $15 \mu\text{m}$  but different in-plane fiber orientations.

Figure 2.8 shows how a non-zero downward body force (taken arbitrarily as 0.012 N/kg) can result in structures with higher SVFs and so higher LEPs (compare the thickness of the sample structures given in Figure 2.8 for  $F=0$  and  $F=0.012$  N/kg).



**Fig. 2.8:** Effects of an external body force on SVF and LEP for media with a basis weight of 45 g/m<sup>2</sup> and a YLCA of 120°. Morphology of the structures in the absence and presence of a body force (albeit chosen arbitrarily at  $F=0.012$  N/kg) are also shown for comparison.

## 2.5 Conclusions

In this chapter, we presented a physics-based model to generate virtual fibrous structures. Treating each fiber as an array of beads, this model can realistically simulate bending of the fibers at fiber–fiber crossovers, and is therefore capable of avoiding fiber–fiber overlaps. We have also developed a model to estimate a liquid entry pressure (LEP) for hydrophobic fibrous media. This model uses the balance of forces acting on the air–water interface (AWI) to relate media’s capillary resistance to intrusion pressure. The analysis is based on a simplifying assumption that the AWI remains both planar and intact as it penetrates inside the media. This assumption makes it possible to estimate an LEP for media with complex morphological or wetting properties (an otherwise very challenging problem). For model demonstration, we have investigated the effects of varying microstructural parameters of a fibrous medium (e.g., fiber diameters, fiber contact angles...) on its LEP. Our results show that the LEP of a fibrous membrane increases upon decreasing the diameter or increasing the contact angle of its constituting fibers.

## **Chapter 3. A new approach to modeling liquid intrusion in hydrophobic fibrous membranes with heterogeneous wettabilities**

### **3.1 Introduction**

Capillarity is the major factor in characterizing the nature of fluid interaction with a porous material. Fibrous materials with positive capillary pressure are hydrophobic and they can be used as a membrane or as a water-resisting barrier for a variety of applications [40-51]. Precise capillary pressure prediction is also important for proper design of gas diffusion layers (GDLs) for fuel cells [127-131] or for applications involving fluid–fluid or fluid–gas separation [71,72,132,133]. Fibrous membranes are promising alternatives to porous films for many separation applications due to their coupled high porosity and mechanical strength [40-51]. When a hydrophobic fibrous membrane (e.g., a distillation membrane used in direct contact membrane distillation) is brought into contact with water, the hydrophobic fibers resist against water intrusion into the pores of the membrane (space between the fibers). Nevertheless, a submerged hydrophobic membrane cannot remain dry under elevated pressures. This is because the interface between the water outside the membrane and the air inside the membrane becomes unstable under excessive pressures, leading to water entering the pores of the membrane (i.e., the membrane’s capillary pressure fails to balance the intrusion pressure) [2,3,42,43,51,52]. The pressure at which water enters the membrane is generally referred to as liquid entry pressure (LEP). While LEP is an easy-to-use single number to characterize hydrophobic membranes, it does not provide much information about the relationship between intrusion pressure and depth of water penetration into the membrane (important for engineering the microstructure of a membrane to maximize LEP while remaining highly porous). Extensive research has been conducted in the past decades to simulate

the intrusion of a non-wetting fluid into a 3-D fibrous membrane. Methods such as Lattice Boltzmann (LB) and Volume of Fluid (VOF) [53,114,116-118,128-130,134] are among the most popular numerical methods utilized for such simulations. The LB and VOF methods both solve the flow field in the wetting and non-wetting phases in a porous media and can be used directly to simulate penetration of a fluid in porous materials as a function of time and space. Such calculations however, are very time consuming, especially in 3-D, even with the current high-speed CPUs. A breakthrough in developing affordable (CPU-friendly) 3-D fluid flow simulations in porous media was the development of the Full Morphology (FM) method in which a quasi-static distribution of wetting and non-wetting phases in a 3-D domain was obtained via a purely geometric approach [119-121]. The FM method uses a sphere caging algorithm to produce a range of intrusion pressures that would have been needed for a non-wetting fluid to enter a 3-D structure if it was made up of a series of fictitious “cylindrical pores” with different diameters. By marking the fraction of the total void space that is made up of “pores” of certain diameter, the FM method obtains a capillary pressure–saturation relationship for the whole media using the Laplace equation written for a cylindrical pore [29,86,100,119-122]. The FM method, while extremely attractive from the viewpoint of saving the CPU time, is nonetheless a geometry-based approach that approximates the irregular void space between the fibers with straight cylindrical pores. In addition, the FM method is not sensitive to wetting properties of the individual fibers (although improved recently [135]). In reality, the 3-D shape and position of the interface between the wetting and non-wetting phases (needed for instance to correctly simulate the breakup of the interface inside the media) depends strongly on both the local geometry and the wettability of the surfaces involved. The simulation method presented in this chapter is based on minimizing the surface energy of the three-phase system (wetting phase, non-wetting phase, and solid surface),

and thereby obtaining the shape and position of the interface inside the membrane as a function of intrusion pressure. This method only tracks the interface between the phases, and so it is computationally faster than the VOF or LB methods, but it is still not as fast as FM method. Unlike the VOF and LB methods (but similar to the FM method), the energy minimization method cannot simulate the dynamics of capillary intrusion (the calculations are time independent). The energy minimization method is programmed in the Surface Evolver (SE) finite element code, but the solver requires the specific volume and energy integrals as well as a series of constraints for each solid object in the domain. It is also important to mention that the implementation presented here is limited to simple 3-D fibrous geometries (e.g., straight fibers aligned in the x or y directions) due to complexities involved in modeling air–water interface (AWI) near fiber–fiber intersection points in purely three-dimensionally random structure. In the remainder of this chapter, we continue by discussing popular methods of interface tracking in fibrous media in Section 3.2. In Section 3.3, we discuss how interactions between two interfaces or between a solid surface and an interface have been handled in the current work. Section 3.4 discusses our simulation method in details and presents some validation studies. Our simulation results are discussed in detail in Section 3.5 followed by the conclusions in Section 3.6.

### **3.2 Interface tracking: force balance vs. energy minimization**

Consider the simple case of an interface between two parallel horizontal fibers with different Young–Laplace contact angles (YLCAs). Upon applying a pressure, the interface deforms to the shape of a circular arc with a radius of curvature that can be obtained using the Laplace equation:

$$p_c = \sigma \left( \frac{1}{R_1} + \frac{1}{R_2} \right) = 2\sigma H \quad (3.1)$$

where  $p$  is pressure,  $R_1$ , and  $R_2$  are principal radii of curvature of the interface,  $\sigma$  is surface tension, and  $H$  is the interface mean curvature (note that  $R_1 = \infty$  for an interface between parallel fibers). Considering the balance of vertical forces acting on this interface (capillary forces at the contact points with the fibers balancing the pressure from top), one can obtain (see Figure 3.1),

$$p_c L (s_f - r_f \sin \alpha_1 - r_f \sin \alpha_2) = \sigma L \left( \cos \left( \frac{3\pi}{2} - \alpha_1 - \theta_1 \right) + \cos \left( \frac{3\pi}{2} - \alpha_2 - \theta_2 \right) \right) \quad (3.2)$$

Simplifying Equation 3.2, one can find the capillary pressure:

$$p_c = -\sigma \frac{\sin(\alpha_1 + \theta_1) + \sin(\alpha_2 + \theta_2)}{s_f - r_f (\sin \alpha_1 + \sin \alpha_2)} \quad (3.3)$$

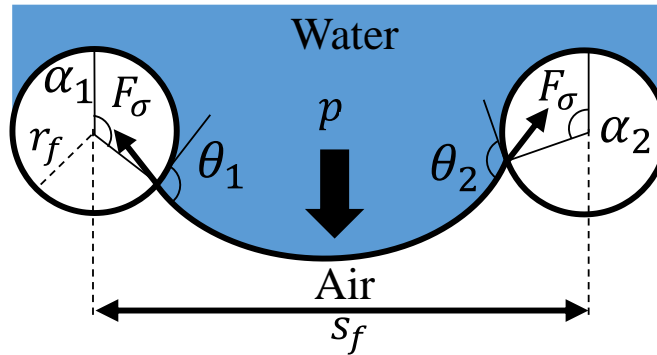


**Fig. 3.1:** Free body diagram of the forces acting on the AWI between two horizontal parallel fibers.

Here  $\theta_i$ ,  $s_f$ , and  $r_f$  are contact angle, center-to-center spacing between the fibers, and fiber radius, respectively. Parameters  $\alpha_1$  and  $\alpha_2$  denote the intrusion angle on each fiber, and they can be found using the method described in [124]. The maximum pressure obtained from Equation 3.3 is often referred to as the critical pressure (corresponding to a critical air–water interface radius of curvature), and it is the pressure above which no stable meniscus can exist between the fibers [122,124]. The 2-D approach described by Equations 3.2 and 3.3 is only a special case of a much more sophisticated problem of tracking AWI in a 3-D space between randomly oriented fibers (in a 2-D model the fibers are parallel with one another and the interface radius of curvature in the

fibers' direction approaches infinity). Representing the local z-coordinate (height) of the interface as  $z = f(x, y)$ , the Laplace equation results in a nonlinear partial differential equation for the shape and location of the interface inside a fibrous medium [4]:

$$f_{xx}(1 + f_y^2) + f_{yy}(1 + f_x^2) - 2f_{xy}f_yf_x = \frac{\rho g}{\sigma} (1 + f_x^2 + f_y^2)^{\frac{3}{2}} \quad (3.4)$$

Subscripts  $x$ , and  $y$  denote the partial derivative with respect to  $x$  and  $y$ , respectively. The only attempt in solving Equation 3.4 for the shape of an AWI in a 3-D disordered medium is the work reported in [136]. These authors solved Equation 3.4 numerically for the AWI between hydrophobic fibers with random or orthogonal in-plane orientations using a Dirichlet boundary condition. While the Dirichlet boundary condition simplifies the numerical solution procedure, it limits the interface tracking simulations to the case of very thin coatings, where displacement of the three-phase contact-line in the thickness direction is negligibly small, and so the AWI can be assumed to be “pinned” to the first layer of the fibers (see [125] for solving Equation 3.4 for an un-pinned AWI using the Neumann boundary condition). In a more recent study, Bucher et al. [125], used the energy minimization method, implemented in the Surface Evolver finite element code, to obtain a critical pressure for superhydrophobic coatings comprised of orthogonally-oriented fibers in ordered configurations. Using this method, they could simulate both the deflection and the displacement of the AWI through the top four layers of fibers in their superhydrophobic coatings. The simulation methodology developed in the present work however, is not limited to the structure's top layers (to thin fibrous membrane as in [4]). Interface tracking in a thick membrane comprised of semi-ordered fibers (albeit perfectly orthogonal) is a more challenging problem as different parts of the interface in such structures interact differently with one another (e.g., coalesce), and this can raise the complexity of the problem at hand significantly (see the next section).

### 3.3 Numerical treatment of interface–interface or interface–solid interactions

As mentioned earlier, AWI tracking in a thick (i.e., comprised of many layers of fibers) medium comprised of randomly distributed fibers involves developing numerical treatments for when the interface comes into contact with itself or with solid objects not previously in touch with the interface (in addition to singularities at the fiber–fiber intersection points). For the case of fluid invasion in a porous medium modeled as a 2-D array of disks arranged in ordered configurations, various numerical percolation-based models have been developed in the past decades [137-140]. In these studies, the interface motion is modeled by a sequence of stable meniscus configurations reached either by incrementally increasing the pressure difference between the invading and defending phases (non-wetting and wetting phase), namely pressure controlled invasion, as in [137], or by a flow-rate-controlled invasion model as in [138,139]. Following the terminology used in such percolation-based 2-D models for meniscus instability, we use “burst”, “touch”, and “coalescence” (overlap) as the three basic treatments of interface–interface or interface–solid interactions. Figure 3.2a shows the burst mechanism. If the prescribed pressure is more than the critical pressure for the AWI between two parallel fibers (Equation 3.3), the AWI grows without reaching an equilibrium position/shape and eventually bursts. This is because the AWI curvature continuously decreases, and so the meniscus expands indefinitely (the pressure can no longer be balanced by the interface curvature) unless it touches neighboring fibers. This usually results in the AWI moving forward (at a given intrusion pressure) to reach out to neighboring fibers. As can be seen in Figure 3.2a, the interface between fibers 3 and 4 expands (indefinitely) until it bursts and leaves an open path for the fluid to flow out of the media, the so-called bubble-point [100]. As an AWI moves inside the media, it comes into contact with new solid surfaces. Such interface–solid surface interactions are referred to here as “touch” interactions, following the terminology of

[137-140]. When an AWI comes into contact with a new fiber, a new AWI is formed and it obeys the YLCA of the new fiber at the new contact line at equilibrium. Depending on the number of fibers involved, the AWI may break up into two or more menisci in the pore space between the fibers (see the interface between fibers 1 and 2 in Figure 3.2b before and after coming into contact with fiber 4). Similar to the burst instability, touch instability is treated individually for each pair of fibers, and each new interface must acquire an equilibrium curvature corresponding to the applied capillarity; this was also discussed in [124]. When two neighboring AWIs come into contact with one another, they are treated as “coalescing” interfaces. In this case, the fiber in contact with both interfaces (fiber 1 in Figure 3.2c) will be submerged, and no longer plays a role in the capillarity of the system. The resultant equilibrium shape and position of the interface is obtained by temporarily removing this fiber from the simulation domain and repeating the same interface-tracking step (without that fiber) [124]. As will be seen later in Section 3.4.2, an AWI penetrating through a porous medium may leave island-like patches of dry fibers behind. To simulate this, we have considered two main possibilities as described in Figure 3.2d and 3.2e. The first case happens (especially in regions with densely packed fibers) when AWIs reach their equilibrium shapes between a group of fibers (e.g., fibers 1, 2, and 3 in Figure 3.2d) without coalescing with one another, and further penetration of the AWI into the media does not impact the stability of the island formed between this group of fibers. The second scenario is when the coalescing AWIs are not in contact with a common fiber as illustrated in Figure 3.2e.

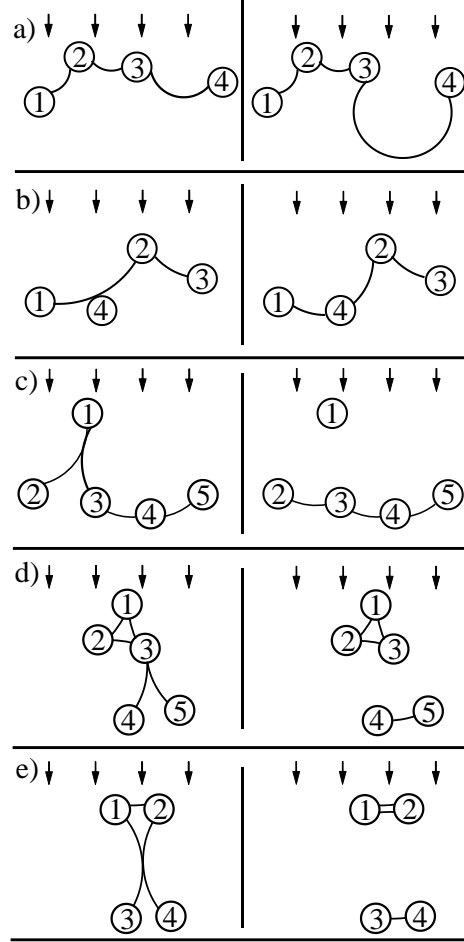


**Fig. 3.2:** Burst instability mechanism is shown in (a) for the AWI between fibers 3 and 4. The touch instability mechanism is shown in (b) for the interface that comes into contact with fiber 4. The coalescence instability mechanism is shown in (c) for the two interfaces meeting each other under fiber 1. Formation of an island between three and two fibers is shown in (d) and (e), respectively.

### 3.4 Simulation method and experimental validation

We use Surface Evolver to predict the shape and location of the AWI in our virtual fibrous media.

The basis of SE calculations is to divide the AWI interface into small triangles (facets), and to move the vertices of these facets iteratively to minimize the energy of the air water solid system given with the following equation [141].

$$E = p \iiint_V dV + \sigma \iint_{A_{LG}} dA_{LG} - \sigma \sum_{i=1}^n \cos\theta_i \iint_{A_{SL}^i} dA_{SL}^i \quad (3.5)$$

where  $p$ ,  $\sigma$ , and  $\theta_i$  are pressure difference across the AWI, surface tension, and the YLCA of fiber  $i$ , respectively. Subscripts S, L, and G refer to solid, liquid, and gas, respectively. The first term in this equation refers to the work done by intrusion pressure on the AWI, the second term is the surface energy of the AWI, and the last term is the solid surface energy on the fibers. The state of minimum energy for a given pressure corresponds to the equilibrium shape of the interface at that pressure. Calculation of system energy requires the integrand  $dA_{SL}$  in Equation 3.5 to be derived for each fiber. Considering an elemental area of the fiber, we have

$$dA = r_f \alpha dx \quad (3.6)$$

where  $r_f$  is fiber radius, and the  $\alpha$  is the intrusion (or immersion) angle given as (see Figure 3.3a),

$$\alpha = \arctan\left(\frac{y-y_0}{z-z_0}\right) \quad (3.7)$$

Calculation of the volume integrand in Equation 3.5 is not straightforward. Surface Evolver calculates the volume between the AWI and the  $z = 0$  plane (the volume with a cross-sectional area shown with ABCD in Figure 3.3b), but ignores the volume above the fiber (the volume with a cross-sectional area shown with ADEF in Figure 3.3b). We therefore modified the above-mentioned volume integrand by subtracting the volume shown with the cross-sectional area of OAF from the one with the trapezoidal cross-section OADE, i.e.,

$$dV = \frac{1}{2} \left( (z + z_0)(y - y_0) - \alpha r_f^2 \right) dx \quad (3.8)$$

With this modification, the volume of the non-wetting phase (water) can correctly be predicted by SE. The area and volume integrands for fibers aligned in the  $y$ -direction, can be derived in a similar way and programmed in SE.

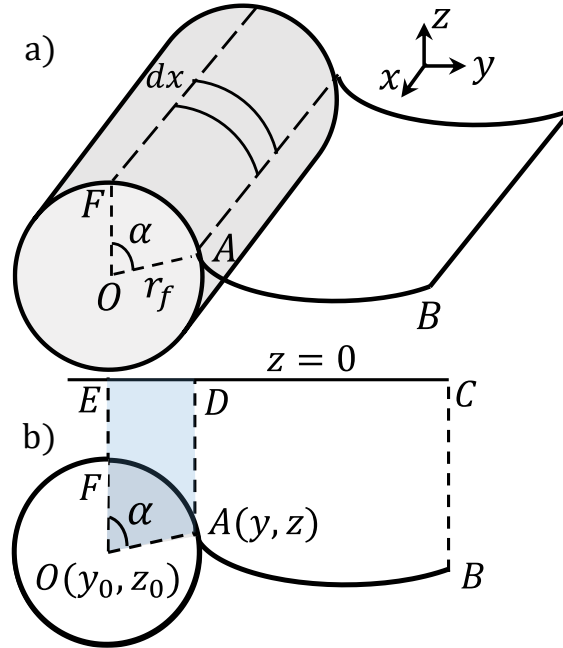


**Fig. 3.3:** Geometric variables used in Equations 3.5–3.8 are shown in (a) using a schematic drawing of the air–water interface in contact with a fiber. Modifications needed for correct non-wetting phase volume calculation in Surface Evolver is shown graphically in (b).

To examine the accuracy of our energy minimization-based simulations, we considered two validation studies. In the first validation, we produced 3-D printed two-layer structures composed of orthogonal fibers, and spray-coated them with a hydrophobic coating. The two-layer media were then used in a custom-made water entry pressure setup to image the AWI at different intrusion pressures and compare them to their numerical counterparts (Section 3.4.1). For the second validation, we obtained the shape and location of the AWI in a 2-D domain as a function of pressure. These predictions were then compared to those obtained in a previous study by Bucher et al. [124] using a force balance approach (Section 3.4.2).

### 3.4.1 Comparison with experiment

For the sole purpose of model validation, we produced a series of 3-D printed fiber layers and spray coated them with a hydrophobic coating, Ultra-Ever Dry from Ultratech Company. Before

applying the hydrophobic coating, an adhesive coating was applied to the fibers and the fibers were allowed to dry in ambient atmosphere for about 45 min. The coating was sprayed in a fine mist and as consistent as possible to maximize the uniformity of the coating. The coated fibers were left to dry for a full day before being used in an experiment. The same coating was also applied to a microscope slide and a YLCA of 123 degrees was observed with deionized water. The experimental setup is similar to the one described in [142], and it consists of an acrylic cylindrical vessel fed with water (dyed with food coloring for better imaging) through a u-tube mounted on an adjustable height gauge. The height gauge was used to adjust the pressure in the vessel by slowly raising the free end of the tube. The top of the vessel is comprised of a holder where the fibers can be mounted and sealed (see Figure 3.4). The height gauge was set to zero once the water level reached up to the fibers' surface (detected through a microscope) and the water level in the u-tube manometer became stable. The hydrostatic pressure applied to the fibers can be obtained as  $p = \rho gh$ , where  $\rho$  is water density,  $g$  is the gravitational acceleration, and  $h$  is the height of the water level column in the tube. The free end of the u-tube was slowly elevated and water penetration into the fiber-layer was monitored through the microscope. The elevated hydrostatic pressure at which water broke through the fiber-layer was then taken as the coalescence pressure.

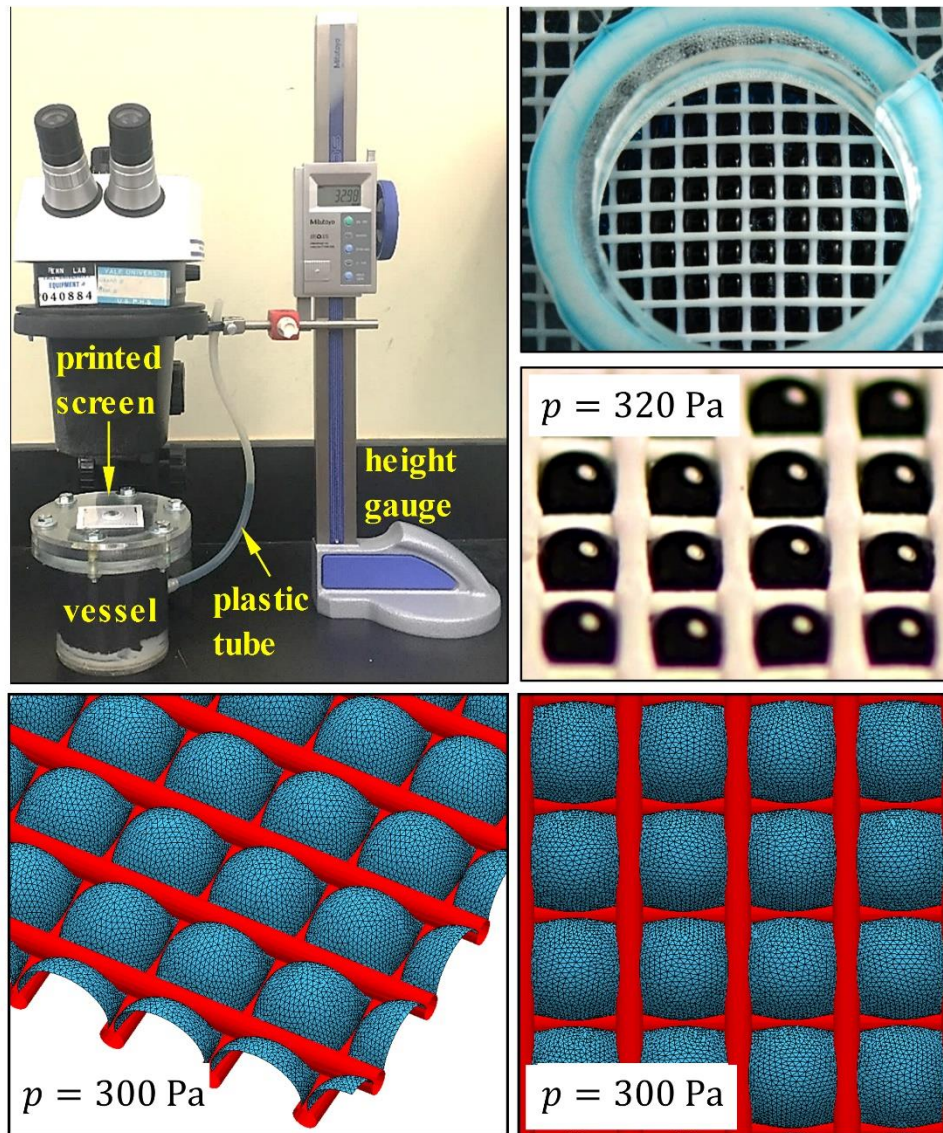


**Fig. 3.4:** The experimental setup used for validating our numerical simulation is shown in the top left figure. Average fiber diameter and fiber-to-fiber spacing are about 250 and 1000  $\mu\text{m}$ , respectively. The figures on the top right show the air–water interface at a pressure of about 320 Pa (slightly below the failure pressure) at two different magnifications. The bottom figures show the air–water interface from numerical simulation at a pressure of about 300 Pa (slightly below the failure pressure). A YLCA of about  $123^\circ$  was measured experimentally and used in the simulations.

For printed geometries comprised of orthogonal fibers with an average diameter of 250  $\mu\text{m}$  and an average center-to-center fiber spacing of 1000  $\mu\text{m}$ , we observed an average failure pressure of about 330 Pa with a standard deviation of 10 Pa ( $330 \pm 10$  Pa). These values were then compared with the numerical simulation results obtained for virtual fiber-layers with identical geometry.

Predictions of our numerical simulations were found to be within 10% of their experimental counterparts. Figure 3.4 shows examples of simulated and imaged AWIs near their failure pressures (320 Pa in experiment and 300 Pa in the simulation). The factors contributing to the mismatch between experimental and numerical results include, but are not limited to, non-uniformity of the coating, inconsistencies in zeroing the height gauge when water level touched the surface of the fibers, and imperfection in the geometry of the 3-D printed fiber-layers (surface roughness, non-circular fiber cross-section...).

### **3.4.2 Comparison with previous 2-D simulations**

As mentioned earlier, Equations 3.1–3.3 were used in [124] to track the penetration of a pressurized non-wetting fluid into 2-D fibrous structures filled with a wetting fluid. The predictions of the force balance approach of [124] are compared to those of our current approach in this section. Consider a 2-D virtual medium composed of unidirectional fibers with a solid volume fraction (SVF) of 0.15 and a fiber diameter of 10  $\mu\text{m}$  in a 500 $\times$ 667  $\mu\text{m}$  simulation domain. Assume the fibers to be made of two different materials having YLCAs of 35° and 65° with the wetting phase (or 145° and 115° with the non-wetting phase). Figure 3.5a shows the AWI reported in [124] at pressure of about 6600 Pa. Figure 3.5b shows similar simulation conducted using our energy-minimization method for the same fibrous domain and at the same exact pressure. Excellent agreement between the two simulation methods is evident from the figure.

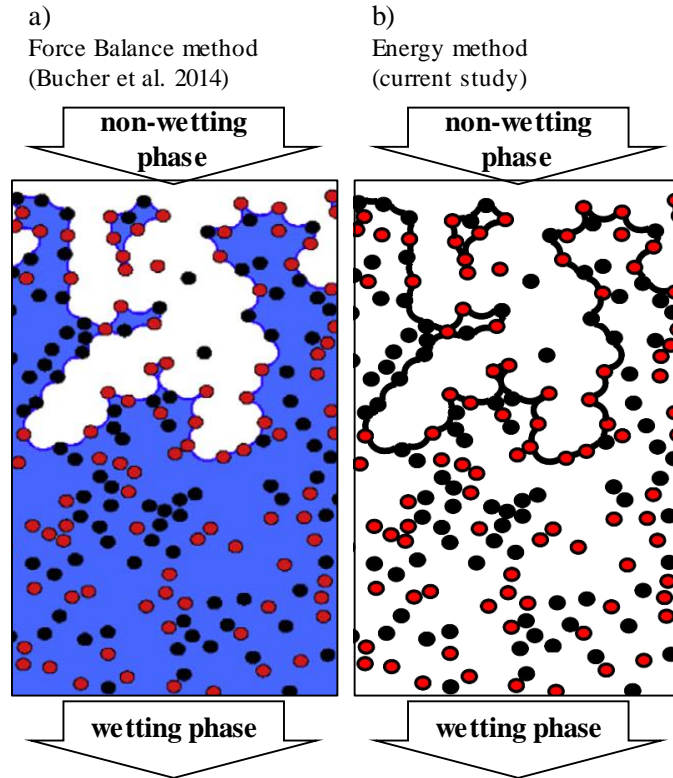


**Fig. 3.5:** Comparison between the AWIs obtained from force balance method reported in [124] (a) and the current energy method (b) for a unidirectional fibrous structure with an SVF of 0.15 and a fiber diameter of  $10\ \mu\text{m}$  at an intrusion pressure 6.6 kPa. Red and black fibers have different YLCAs of  $35^\circ$  and  $65^\circ$  with the wetting phase ( $145^\circ$  and  $115^\circ$  with the non-wetting phase), respectively.

### 3.5 Results and discussion

#### 3.5.1 Interface modeling in membranes with semi-ordered orthogonal parallel fibers

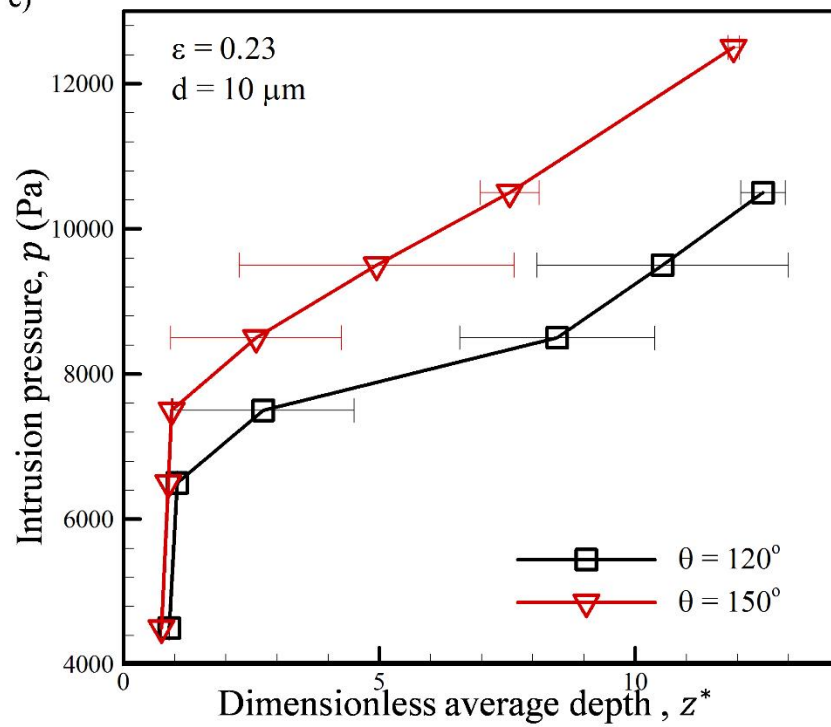
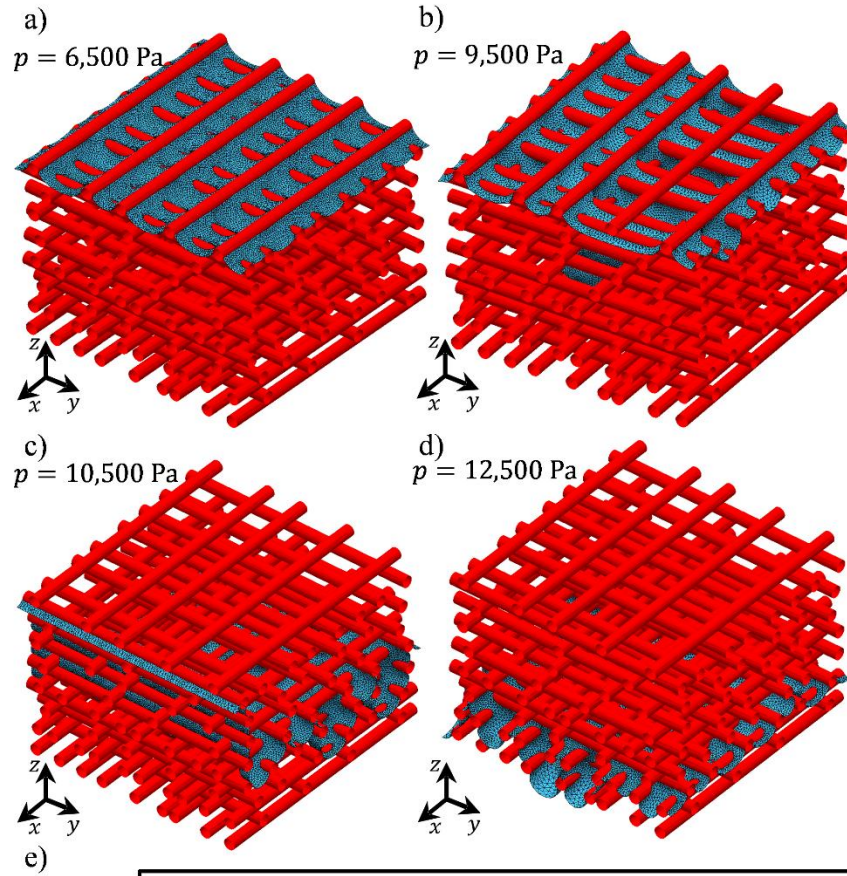
In this section, we demonstrate how the proposed energy-minimization method can be used to obtain the shape and position of the AWI in a multi-layer fibrous structure with orthogonally oriented fibers. For structures considered in this chapter, number of fibers does not change dramatically from one layer to the other (SVF of each layer is almost a constant number). To generate orthogonally oriented layers of semi-ordered parallel fibers, we first distributed the fibers in an orderly fashion, but then moved them randomly in the neighborhood of their original

positions (without changing their orientation) by adding an arbitrary “noise” to their locations. We considered a noise amplitude obtained from Equation 3.9 as was described previously in [122].

$$\delta = \min\left(\frac{\left(\frac{L}{n}\right)-d}{2}, \eta d\right) \quad (3.9)$$

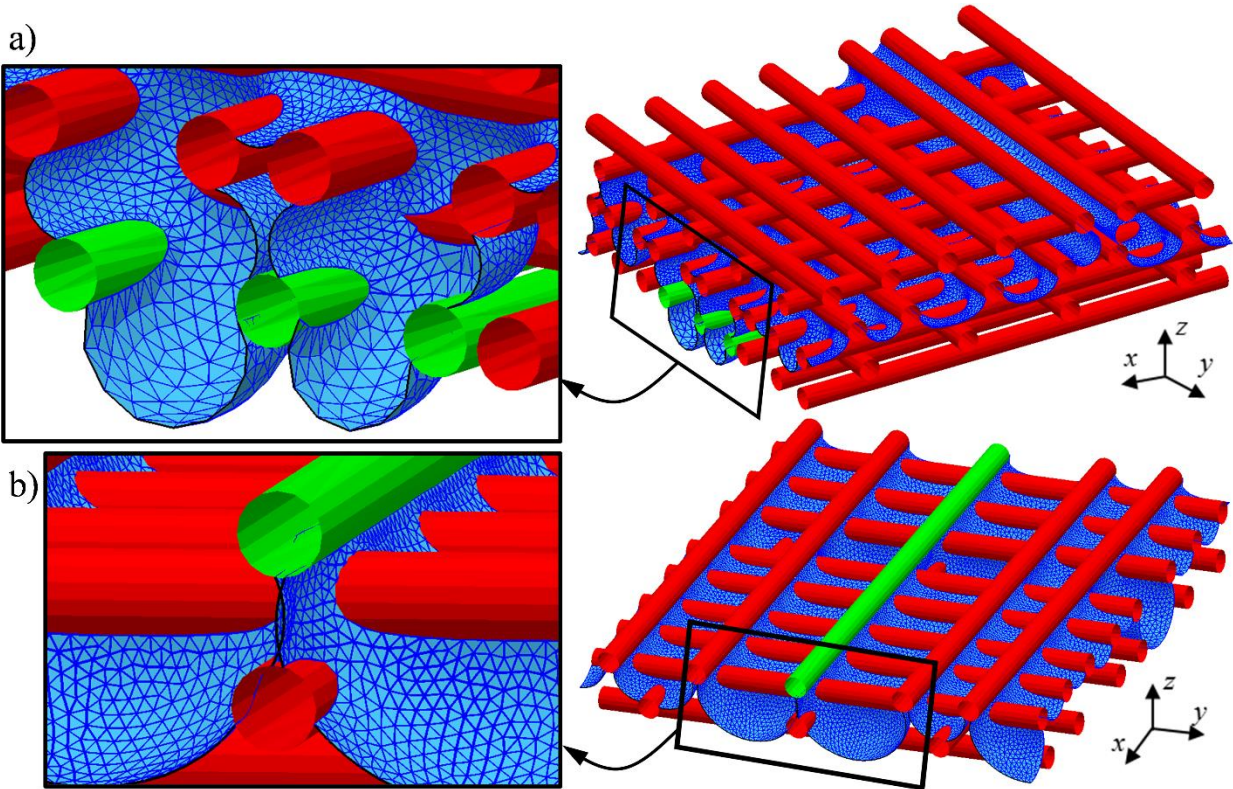
In this equation  $L$ ,  $n$ , and  $d$  are the in-plane size of the domain, number of fibers in the layer, and fiber diameter, respectively, and  $0 < \eta < 1$  is a computer-generated random number. Note that in implementing this method, special care was paid to exclude fiber positions resulting in a fiber–fiber overlap (non-physical) [122]. As mentioned earlier, the simulation method presented in this work is both accurate in terms of foundational physics and CPU friendly. We considered a computational domain having in-plane dimensions of  $210 \times 210 \mu\text{m}$  and a thickness of  $150 \mu\text{m}$  ( $z$ -direction), corresponding to 15 layers of fibers with a diameter of  $10 \mu\text{m}$  (resulting in a solid volume fraction of 23%) and an YLCA of 150 degrees. While the periodic boundary condition is the most appropriate type of boundary condition for the kind of study considered here, we chose to use symmetric boundary conditions for the lateral boundaries of our computational domain to ease the interface tracking in SE. Obviously, there is no plane of symmetry in a fibrous medium comprised of semi-ordered (albeit perfectly orthogonal) fibers. Therefore, special care should be taken to ensure that the in-plane dimensions of the simulation domain are large enough to statistically represent a real fibrous structure (negligible edge effects). Nevertheless, with finite computational power, simulations with a given set of parameters have to be repeated on an ensemble of statistically identical structures to ensure confidence in the results. The results presented in this study are averaged over an ensemble of no less than three structures. Figures 3.6a through 3.6d show examples of AWI shape and position inside the membrane under different intrusion pressures. The structures are assumed to be filled initially with air, and water is then pushed into them by incrementally increasing the intrusion pressure. It can be seen that the AWI

continues to penetrate into the structure with increasing the pressure from 6.5 to 12.5 kPa. With such detailed information about the shape and location of the AWI, one can calculate the average AWI penetration depth at any prescribed pressure (see Figure 3.6e). It can be seen in this figure that higher pressures are needed to force the AWI deeper into the membrane. The horizontal axis is the dimensionless penetration depth  $z^*$  (average penetration depth divided by equivalent fiber diameter). To investigate the effects of YLCA on intrusion pressure, simulation results for a membrane with identical structures but a YLCA of 120 degrees are also added to Figure 3.6e. As expected, intrusion pressure is less when the fibers are less hydrophobic. As was discussed earlier, interface tracking in a semi-ordered membrane is a challenging task due to meniscus instabilities. Conducting simulations like those reported in Figure 3.6 require close attention to the stability of the AWI as it penetrates through the structure.



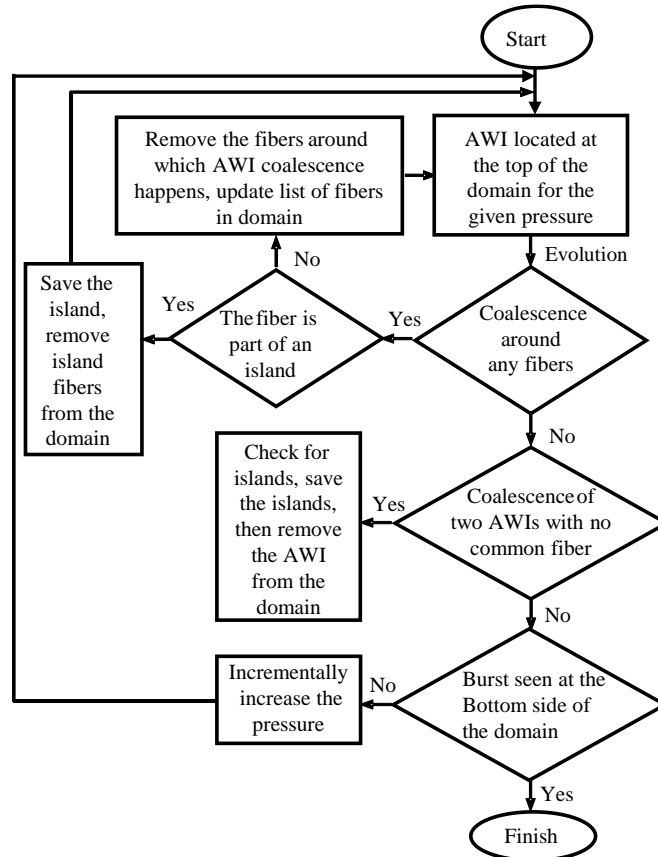
**Fig. 3.6:** Simulation of AWI inside a structure with an SVF of 0.23, a fiber diameter of 10  $\mu\text{m}$ , and a YLCA of 150° at different intrusion pressures from 6.5 kPa through 12.5 kPa shown in (a) through (d), respectively. The intrusion pressure vs. penetration depth simulation results are given in (e).

Figure 3.7a shows a magnified view of an AWI undergoing the burst instability near the bottom of the membrane previously discussed in Figure 3.6 (the fibers accommodating the bursting AWI are shown in green for better illustration). Figure 3.7b, shows a magnified view of two AWIs in contact with a common fiber (shown in green) undergoing coalescence instability. Coalescence of these AWIs results in the submersion of the green fiber in the wetting phase (the green fiber will be fully wet). It is important to mention that, for the sake of simplicity, we have assumed that the entire length of a fiber is submerged in the wetting phase once only a segment of its length is submerged (due for instance to AWI coalescence). This assumption helps to alleviate an otherwise challenging problem of modeling contact-line motion along the length of the fibers. We acknowledge that this approximation detracts from the versatility of the model as it relies on the geometrical regularity of the structure.



**Fig. 3.7:** The burst and coalescence failure mechanisms are shown in (a) and (b), respectively.

Our intrusion pressure simulation procedure is summarized in a flowchart shown in Figure 3.8. The simulations start by placing an AWI on the surface of the membrane for a very low intrusion pressure, and end once a local AWI burst is detected on the bottom side of the structure as the pressure is incrementally increased.



**Fig. 3.8:** Flowchart for the simulation algorithm.

### 3.5.2 Intrusion pressure vs. penetration depth

In this section, we study the effects of fiber size or contact angle heterogeneity on the intrusion pressure of fibrous media. We limit our study to fibrous membrane comprised only of two different species for the sake of brevity, but our approach can also be applied to membrane with multiple fibrous species. We use the terms Bimodal-D or Bimodal-CA to refer to a membrane with bimodal diameter or bimodal contact angle distributions, respectively. Fig. 9a and b show the AWI at an

intrusion pressure of  $p = 5$  kPa in two Bimodal-D structures with an SVF of  $\varepsilon = 0.23$ , and a fixed YLCA of  $\theta = 120^\circ$ . These structures are comprised of fine (shown in red) and coarse (shown in blue) fibers with a diameter of  $d = 10$  and  $20 \mu\text{m}$ , respectively. The fine fiber volume fraction is 50% for the structure shown in Figure 3.9a, and 25% for the one shown in Figure 3.9b. It can be seen that AWI penetrates deeper in the structure for which the fine-fiber volume fraction is less (Figure 3.9b), as the pores are generally larger in such media. Figure 3.9c shows the intrusion pressure versus dimensionless penetration depth for the above Bimodal-D membrane having different fine-fiber volume fractions (denoted as  $v_1^d$ ). Note that the horizontal axis in Figure 3.9c is the dimensionless penetration depth (average AWI penetration depth divided by equivalent diameter), and it refers to the average number of layers that are submerged in water. For structures considered here, the equivalent diameter is equal to  $10 \mu\text{m}$ ,  $13.33 \mu\text{m}$ ,  $13.33 \mu\text{m}$ , and  $20 \mu\text{m}$  for the  $v_1^d = 1$ ,  $v_1^d = 0.5$ ,  $v_1^d = 0.25$ , and  $v_1^d = 0$ , respectively.

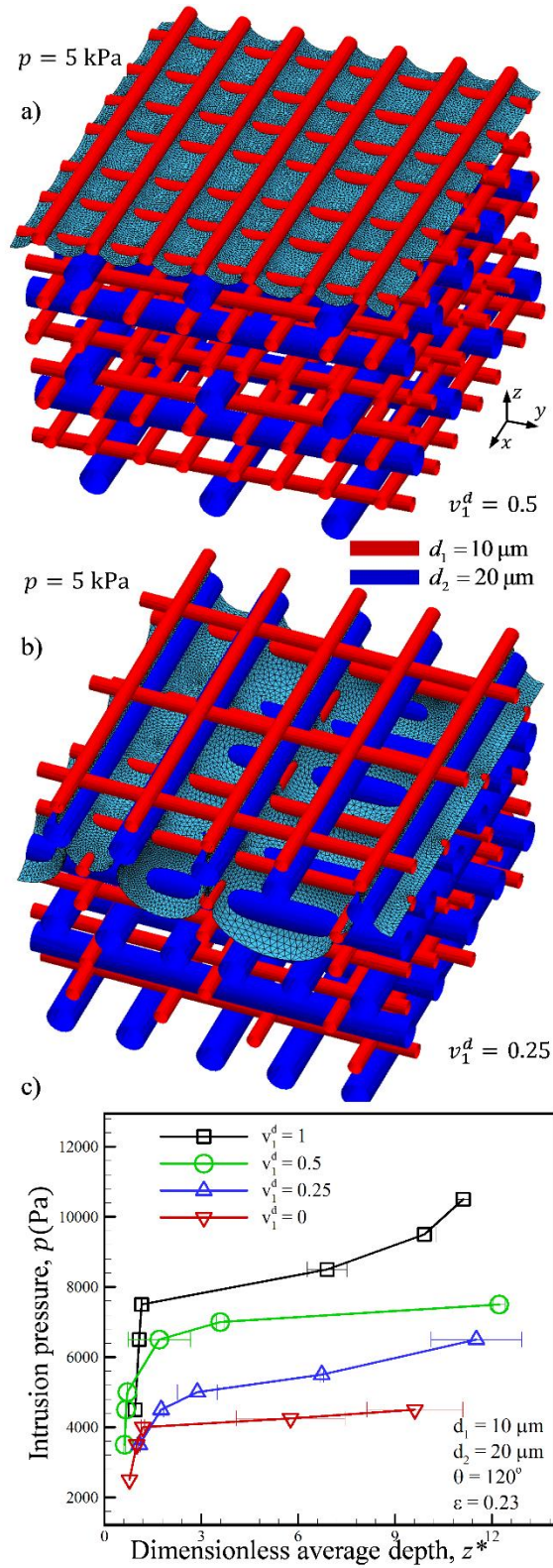


**Fig. 3.9:** Simulation of AWI inside Bimodal-D structures with an SVF of 0.23 but different volume fractions of fine ( $10 \mu\text{m}$ ) or coarse ( $20 \mu\text{m}$ ) fibers. The YLCA of the fibers is assumed to be  $120^\circ$  and the intrusion pressure is set at 5 kPa. Volume fraction of fine fibers is 50% and 25% in (a) and (b), respectively. The intrusion pressure vs. penetration depth simulation results are plotted in (c).

Consider a Bimodal-CA fibrous structure with an SVF of 0.23 and a fixed fiber diameter of 10  $\mu\text{m}$ . The structure is comprised of fibers with YLCAs of  $\theta_1 = 150^\circ$  (66% volume fraction) and  $\theta_2 = 120^\circ$  (34% volume fraction) shown with red and blue colors, respectively, in Figure 3.10a. This figure also shows the AWI at an intrusion pressure of 9.5 kPa. Figure 3.10b shows the AWI at the same intrusion pressure for the same structure but with fibers' YLCAs swapped. It can clearly be seen that the AWI penetrates deeper in the structure with less hydrophobic fibers (Figure 3.10b). Note also in Figure 3.10a that AWI penetration is less in regions where the fibers are closer to one another. Defining the volume fraction of the more hydrophobic fibers in a Bimodal-CA medium as  $v_1^\theta$ , effects of  $v_1^\theta$  on intrusion pressure–depth relationship is shown in Figure 3.10c. Comparing the results shown in Figures 3.9c, and 3.10c, indicates that intrusion pressure of a fibrous medium depends on fiber diameter more strongly than it depends on YLCA.

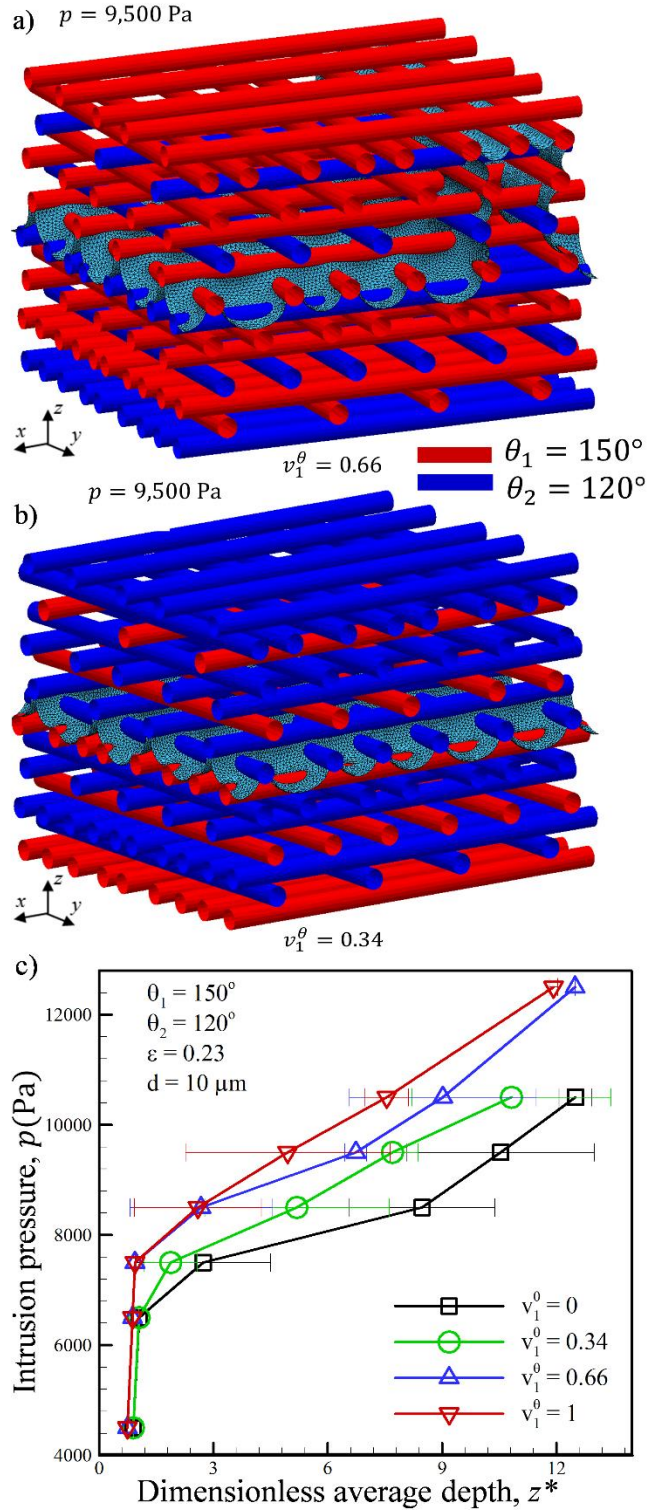


**Fig. 3.10:** Simulation of AWI inside Bimodal-CA structures with an SVF of 0.23 and a fiber diameter of  $10 \mu\text{m}$  but different fiber YLCAs of 150 and 120 degrees. The intrusion pressure is set at 9.5 kPa. Volume fraction of more hydrophobic fibers is 66% and 34% in (a) and (b), respectively. The intrusion pressure vs. penetration depth simulation results are given in (c).

A more realistic scenario is when both the YLCA and fiber diameter vary in a bimodal fibrous structure (referred to as Bimodal-D-CA). The inset in Figure 3.11 shows an example of our AWI tracking (for an intrusion pressure of 7.5 kPa) in a Bimodal-D-CA membrane with an SVF of 0.23, made of two types of fibers, one with a YLCA of  $150^\circ$  and a diameter of  $10\ \mu\text{m}$  (shown in red) and the other with a YLCA of  $120^\circ$  and a diameter of  $20\ \mu\text{m}$  (shown in blue). The intrusion pressure–depth relationship for this membrane is plotted in Figure 3.11. The volume fraction of each species is arbitrarily chosen to be 0.5.

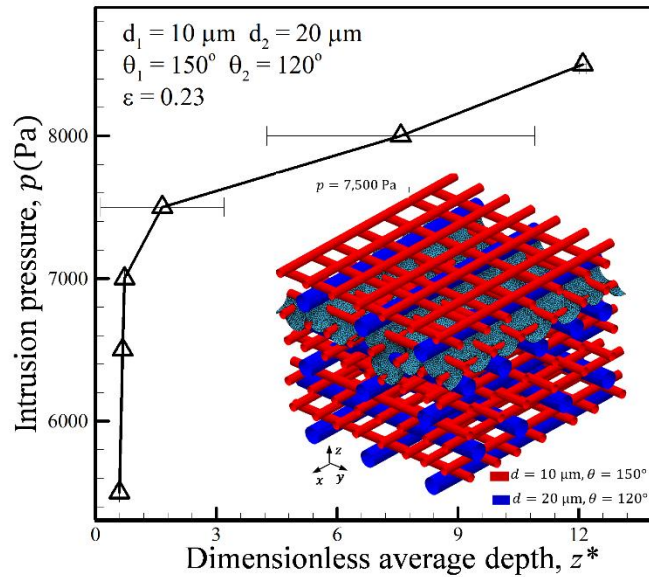


**Fig. 3.11:** The intrusion pressure vs. penetration depth results for Bimodal-D-CA membranes with an SVF of 0.23. Simulation of AWI inside Bimodal-D-CA membranes with an SVF of 0.23 at an intrusion pressure of 7.5 kPa is shown in the inset. The structures are composed of fibers with a diameter  $10\ \mu\text{m}$  and a YLCA of  $150^\circ$  (shown in red) and fibers with a diameter  $20\ \mu\text{m}$  and a YLCA of  $120^\circ$  (shown in blue).

### 3.6 Conclusions

Intrusion pressure for fibrous membranes comprised of orthogonally-oriented layers of semi-ordered parallel fibers was simulated in this work using an interface tracking approach implemented in the Surface Evolver finite element code. For model validation, we compared the predictions of our interface tracking method with those obtained from analytical force balance method (e.g., [124]) or experiment but for simpler fibrous geometries. The main advantage of the simulation method developed in this work is the ability to resolve the shape and position of the air–water interface as the interface penetrates into the membrane, which includes the breakup of an interface into smaller interfaces. Moreover, the proposed method can predict the effects of fiber diameter or contact angle dissimilarity on intrusion pressure with a reasonable CPU time. The main disadvantage of the method on the other hand, is that it is very sensitive to the internal geometry of the membranes, making it hard to apply the method to membrane comprised of purely random fibrous structures. The advantages and shortcomings of the energy method are also discussed relative to those of some other methods like VOF, LB, or FM. For demonstration purposes, we simulated the effects of fiber diameter or fiber contact angles on membrane intrusion pressure. It was shown that increasing the volume fraction of the fine fibers, or fibers with a higher YLCA, leads to an increase in the intrusion pressure of the resulting media [4,125].

## Chapter 4. On liquid bridge adhesion to fibrous surfaces under normal and shear forces

### 4.1 Introduction

Formation of a liquid column between two surfaces is often referred to as a liquid bridge. Liquid bridges are seen in nature, e.g., in frogs, insects, or geckoes climbing a wall [11–13] or in wet beach sands adhering to one another [54], and in industrial applications like printing [14-15], microstereolithography [143-144], papermaking [16], filtration [145], or atomic force microscopy [17–18]. Pioneering research on liquid bridges dates back to 1805, when Young created a liquid bridge between two flat plates to study surface tension [20]. Later, Laplace formulated the pressure difference across an interface between two immiscible fluids in terms of the curvature of the interface, i.e., the Laplace pressure [19], and it was then presented by Gauss in the form of the Young–Laplace equation [146]. The Young–Laplace equation has been solved analytically for the simple case of a liquid bridge between two similar [55–56] (or dissimilar [57]) flat plates in the absence of gravity, or numerically for a liquid bridge between a sphere and a flat plate [58], between two spherical particles [59-61], or between two cylindrical fibers [62-63]. These studies were mainly aimed at predicting the forces acting on a liquid bridge as a function of the spacing between the surfaces or their wetting properties. Despite the differences in the methods used to solve the Young–Laplace equation (or the geometries considered), the above investigations shared one important attribute: they all assigned a single equilibrium contact angle (CA) to the liquid–air interface at the liquid–solid–air triple contact-line (TCL). This is obviously an idealization as in practice, owing to surface roughness [64] or heterogeneity [65], a surface often shows a lower CA, when the TCL is receding, and a higher CA, when it is advancing (with the difference between them being referred to as the contact angle hysteresis, CAH).

Liquid bridges formed between two identical parallel plates were classified as the  $R$ -bridges (where the interface is pinned to the circumference of a circular plate) or the  $\theta$ -bridges (where a CA is assigned to a moving TCL) by Fortes [147] who reported the possibility of observing more than one equilibrium profile for a liquid volume between two parallel plates. Most published studies in the literature have considered a moving TCL (with a single-valued CA) as the boundary condition, when studying the compression or stretching of a liquid bridge between two parallel plates. De Souza et al. [148–150] were the first to consider two  $\theta$ -constant lines, corresponding to the advancing and receding CAs of the surface, in simulating a liquid bridge compression or stretching, and Chen et al. [66–68] were the first to systematically incorporate a CAH in liquid bridge modeling. These authors used a pinned TCL boundary condition, when the CA was between the receding and advancing values, and a moving (unpinned) TCL boundary condition, when the CA had reached the advancing or receding CAs. In the present study, we describe how TCL pinning/unpinning affects the behavior of a liquid bridge between two parallel plates during compression or stretching using  $R$ -constant (pinned TCLs) and  $\theta$ -constant (moving TCLs) lines on force–spacing plot. We use this new approach to describe the moment of transition from one mode of liquid–surface interaction to the other via insightful energy plots. We also use the  $R$ -constant and  $\theta$ -constant lines to map the compression–stretching process and to predict the fate of the liquid bridge under a compression–stretching cycle.

The remainder of this chapter is organized as follows. Section 4.2 presents our experiments including our test setup and surface coating methods. The underlying physics of the problem at hand as well as our simulation approaches are discussed in Section 4.3, and are followed by a validation study in Section 4.4. Section 4.4 also presents our computational and experimental

results for liquid bridge under varying degrees of compression, stretching, and shear. The conclusions drawn from our study are given in Section 4.5.

## 4.2 Experimental Setup and Materials

### 4.2.1 Test Setup

As shown in Figure 4.1, our experimental setup is comprised of two flat plates on which the test surfaces (or coatings) were mounted. The lower plate was placed on a sensitive scale (Mettler Toledo XSE105DU) with an accuracy of 0.01 mg while the upper plate was mounted on a height gauge. A glycerol-in-water solution with a glycerol concentration of 15% by weight was considered as our test fluid (glycerol was added to DI water to help lowering the rate of evaporation without affecting the surface tension  $\sigma = 0.072$  N/m and density  $\rho = 1,039$  kg/m<sup>3</sup> of the DI water). Droplets with a volume of 7  $\mu$ L were deposited on the lower plate using a New Era NE-300 syringe pump, and the scale was zeroed after each droplet placement. The upper plate was lowered incrementally until it touched the droplet and formed a liquid bridge between the plates (the scale was observed to show a negative weight, corresponding to the attraction forces exerted on the droplet by the upper plate, at the moment of contact). The upper plate was then moved to first compress and then stretch the liquid bridge while the forces on the lower plate was being recorded by the scale. The entire process of liquid bridge formation and compression/stretching up to the moment of breakup was captured by a high-speed camera (Phantom Miro Lab 340) equipped with a Tokina 100mm F 2.8 D lens. Special care was taken to ensure that the experiment was conducted slowly so that the compression–stretching process could be treated as a quasi-static process. The quasi-static assumption was also justified on the basis on small Capillary and Weber numbers ( $Ca = \frac{\mu U}{\sigma} = 2.13 \times 10^{-7} \ll 0.1$  ,  $We = \frac{\rho U^2 r}{\sigma} = 1.7 \times 10^{-9} \ll 1$ , with  $U$  as the velocity

of the upper plate,  $r$  as the characteristic length of the liquid bridge, taken as the radius of a sphere with the same volume of liquid, and  $\mu$ ,  $\sigma$ , and  $\rho$  as the viscosity, surface tension, and density of our glycerol-in-water solution, respectively) that were obtained for the experiment.

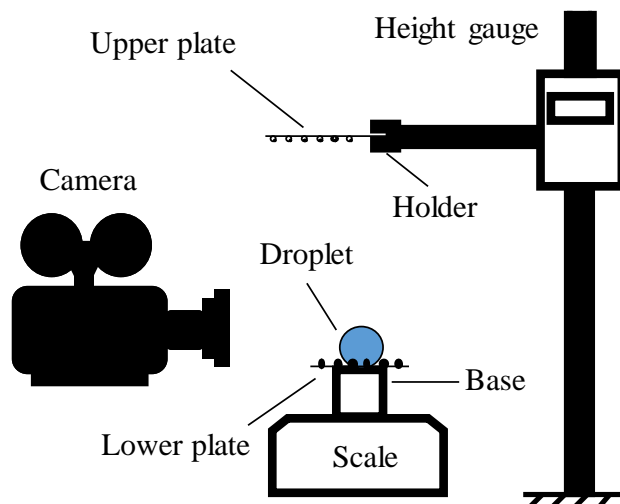


**Fig. 4.1:** Schematic drawings for the setup used for liquid bridge experiments.

#### 4.2.2 Electrospinning Fibrous Coatings

Electrospinning is a simple method of producing nanofiber coatings from a charged solution [151-153]. We employed this process to produce fibrous coatings with different wettabilities. To create a hydrophobic fibrous coating, a Polystyrene (PS) solution was produced by dissolving PS pellets in a 70–30 wt% mixture of Toluene and Tetrahydrofuran (THF) to obtain a 25 wt% PS solution (to ensure homogeneity, the solution was stored in a refrigerator for a day before being used for electrospinning) [154]. A positive voltage of 5.5 kV, with respect to a grounded target, was applied to the tip of a syringe mounted on a syringe pump with an infusion rate of 2.5  $\mu\text{L}/\text{min}$ . Under the influence of the electrostatic force, microscale fibers were ejected toward a substrate (a microscope cover glass purchased from McMaster Carr) mounted on a drum (grounded target) located 85 mm

away from the syringe tip. Drum was given axial and rotational motions with velocities of 15 mm/s and 1,200 rpm, respectively. This allowed us to produce electrospun coatings comprised of aligned fibers. In this study, three-layer orthogonal PS electrospun coatings with spinning time of 5 min for each layer were produced (see Figure 4.2).

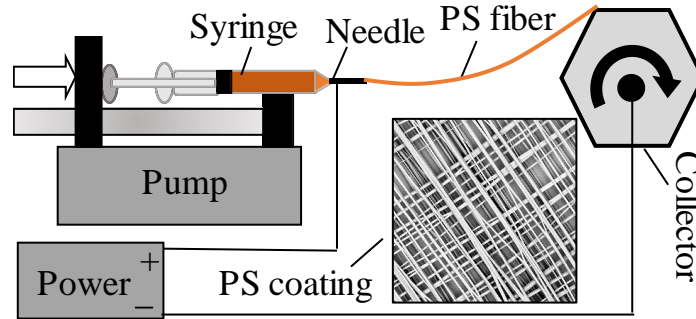


**Fig. 4.2:** Schematic drawings for the setup used for polystyrene electrospinning. The inset SEM image is an example of our PS coatings comprised of orthogonally-layered fibers.

## 4.3 Theoretical Analysis

### 4.3.1 Balance of Forces on A Liquid bridge

Consider the liquid bridge between the plates shown in Figure 4.3. Forces acting on the bridge are the TCL forces (acting along the TCL on the upper and lower plates), the force from the Laplace pressure on both plates, and the gravitational force. The significance of the gravitation force is often judged using the Bond number  $Bo = \frac{\Delta\rho g r^2}{\sigma}$  (with  $\Delta\rho$  density difference between the two phases i.e., air and water,  $g$  the gravitational acceleration, and  $r$  the characteristic length, taken as the radius of a sphere with the same volume of liquid). For small droplets, where  $Bo < 1$ , the effects of gravity are negligible, and the vertical adhesion force on the upper plate is the same as that on the lower plate. When gravity is important, the Laplace pressure  $\Delta P$  (and hence the mean curvature

of the liquid bridge  $H$ ) varies in the  $z$ -direction (i.e.,  $\Delta P(z) = \Delta P_L - \rho g z$ , and  $H(z) = H_L - \rho g z / 2\sigma$ ).

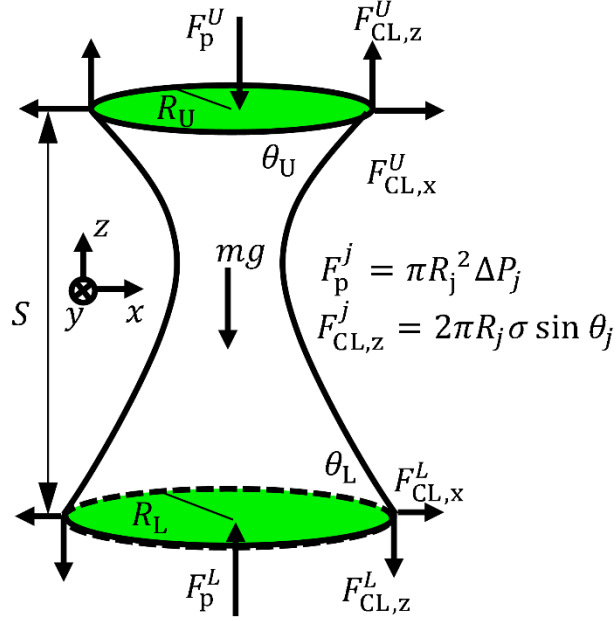


**Fig. 4.3:** Free body diagram for a liquid bridge between two horizontal plates.

In other words, the lower plate experiences a higher pressure than the upper plate (the difference being the hydrostatic pressure), when the gravity is not negligible. Considering the balance of vertical forces on a liquid bridge, we can write (see Figure 4.3),

$$\sum F_z = F_{CL,z}^U - F_p^U - F_{CL,z}^L + F_p^L - mg = 0 \quad (4.1)$$

where  $F_{CL,z}$  and  $F_p$  are the TCL and pressure (from the Laplace pressure) forces, respectively, and they can be calculated as,

$$F_{CL,z}^j = 2\pi R_j \sigma \sin \theta_j \quad (4.2)$$

$$F_p^j = \pi R_j^2 \Delta P_j \quad (4.3)$$

In these equations,  $R$  refers to TCL radius,  $\theta$  is the CA, and subscripts  $U$  and  $L$  denote the upper and lower plates, respectively. It can be seen from Equation 4.1 that the vertical adhesion force on the upper plate (i.e.  $F_U = F_{CL,z}^U - F_p^U$ ) is larger than its counterpart on the lower plate. Calculating the adhesion forces between a liquid bridge and its hosting plates requires accurate information about the equilibrium shape of the liquid bridge, which is obtained here by solving the Young–Laplace equation with proper boundary conditions. Two different boundary conditions may become necessary in describing the liquid bridge compression–stretching process mathematically. The first scenario is when the TCL is fixed and the CA is free to vary between the advancing  $\theta_a$  and receding  $\theta_r$  CAs (referred to as the pinned TCL). The second scenario is when at a constant CA (receding or advancing), the TCL is allowed to freely move on the surface (referred to as the unpinned or moving TCL). Obviously depending on the choice of boundary conditions, the equilibrium shape of a liquid bridge and the adhesion forces on the plates, vary with varying the spacing between the plates.

### 4.3.2 Numerical Simulation

As discussed earlier, studying the forces acting on the plates during the compression and stretching of a liquid bridge requires detailed information about the instantaneous AWI shape of the liquid bridge. Quasi-static process is considered in this work (i.e. the compression and stretching of the liquid bridge is performed slowly), which is different from the dynamics of the liquid shape and its interfacial deformation that are often investigated via molecular dynamics approaches [155–157]. Simulation of the quasi-static process is achieved here through solving the Young–Laplace equation via the Surface Evolver (SE) finite element code [141]. SE predicts the equilibrium shape of a fluid–fluid interface, e.g., air–water interface (AWI), by dividing the AWI into small triangular facets, and moving the vertices of these facets to minimize the total energy of the system

iteratively, while also satisfying a set of constraints (e.g., a pinned or moving TCL) [123,158-159].

The total energy of the solid–liquid–gas system for a liquid bridge can be defined as,

$$E = \iiint_V (p_L - \rho g z) dV + \sigma \iint_{A_{LG}} dA_{LG} - \sigma \cos \theta_L \iint_{A_{SL}^L} dA_{SL} - \sigma \cos \theta_U \iint_{A_{SL}^U} dA_{SL} \quad (4.4)$$

The first term in Equation 4.4 is the work done on the liquid–gas interface by the liquid bridge internal pressure (the sum of the Laplace and hydrostatic pressures), and the second term is the surface energy of the liquid–gas interface. The last two terms on the RHS incorporate the Young equation (i.e.  $\gamma_{SG} - \gamma_{SL} = \sigma \cos \theta$ ) to calculate the solid surface energy on the lower and upper plates. For the case of moving TCLs (with a known CA), the Young–Laplace equation should be solved for the TCL radius, with the surface receding or advancing CAs assigned to  $\theta_L$  or  $\theta_U$  in Equation 4.4. In addition, the solid–liquid differential area element  $dA_{SL}$  for the upper and/or lower plate(s) should also be defined for SE as,

$$dA_{SL} = x dy \quad (4.5)$$

The liquid bridge equilibrium solid–liquid area  $A_{SL}$  will be then obtained by minimizing the energy of the system (Equation 4.4) iteratively. For the case of pinned TCLs (known TCL radius) on the other hand, the Young–Laplace equation should be solved for the CA. This was done here by considering a circular TCL for the liquid bridge with its parametric representation in the polar coordinates given as,

$$x = R_i \cos \phi \quad (4.6)$$

$$y = R_i \sin \phi \quad (4.7)$$

$$z = z_i \quad (4.8)$$

where, subscript  $i$  can represent the lower or the upper plate. Once the minimum energy of the system is reached through iterations, the equilibrium CA of the liquid bridge on the plates will be predicted by iteratively minimizing the energy of the system. The volume of the liquid bridge is found by adding up the individual volumes of the vertical prism between each facet and the lower plate ( $z = 0$  plane). To account for the upper plate in SE calculations, the differential volume element  $dV$  should be programmed in SE as,

$$dV = z_U x dy \quad (4.9)$$

Figure 4.4 shows a simulated liquid bridge between two horizontal plates. The facets adjacent to the lower plate (the  $xy$ -plane) are shown in red. CA is defined for the simulations as the angle between the normal to the facet and that to the plate. Assuming that the normal vector to a facet on the TCL to be  $\hat{n} = (v_1, v_2, v_3)$ , the CA for the lower plate can be found as,

$$\theta_L = \text{acos}\left(\frac{v_3}{\sqrt{v_1^2 + v_2^2 + v_3^2}}\right) \quad (4.10)$$

Similarly, for the facets adjacent to the upper plate,

$$\theta_U = \text{acos}\left(\frac{-v_3}{\sqrt{v_1^2 + v_2^2 + v_3^2}}\right) \quad (4.11)$$

Although a coarse mesh size was used in Figure 4.4 for illustration, special attention was paid to ensure that the mesh size used for the simulations was fine enough to produce grid-independent results.

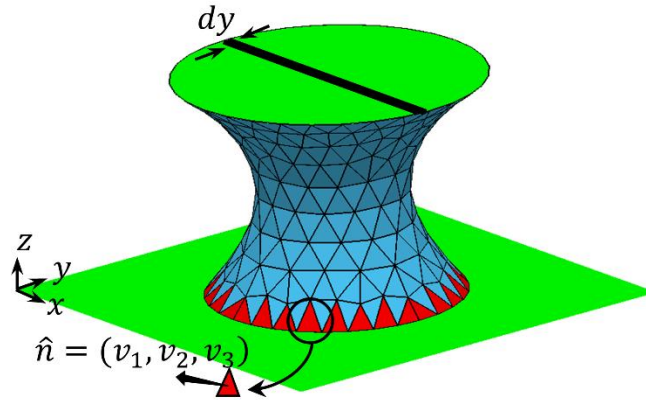


**Fig. 4.4:** A virtual liquid bridge between two horizontal plates with the facets on the lower TCL shown in red.

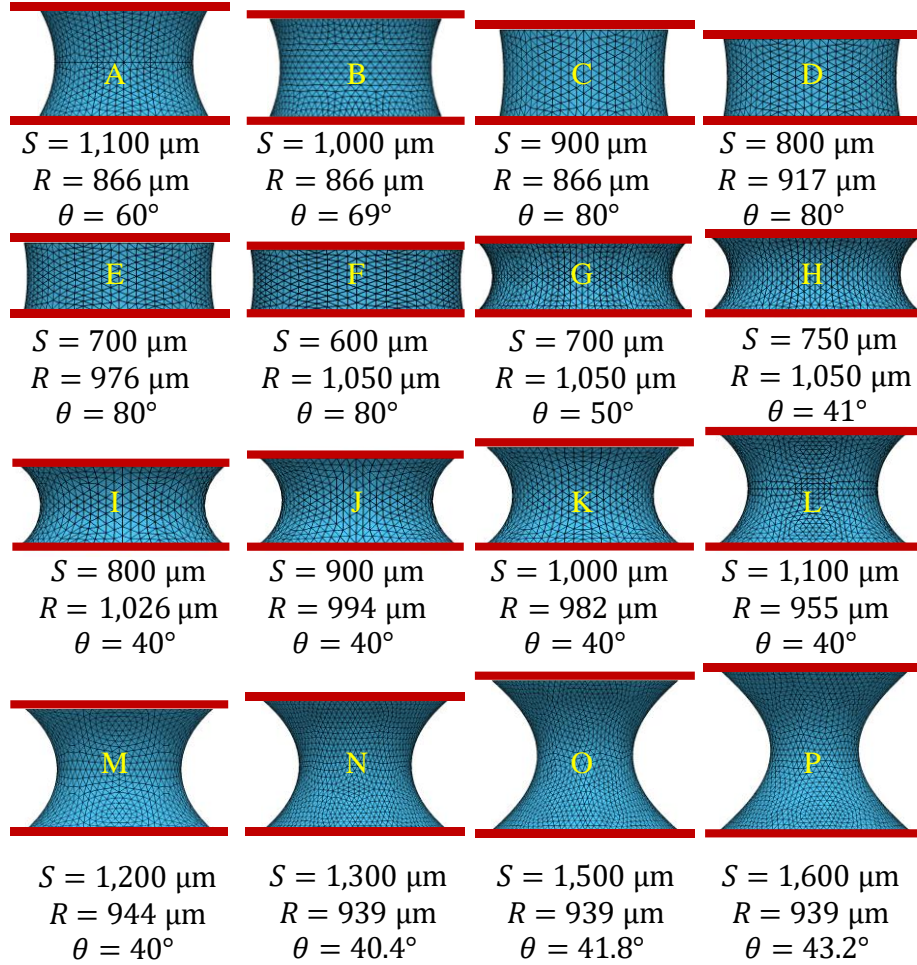
Throughout the simulations, we calculated the CAs of the liquid bridge and compared them to the measured advancing and receding CAs. Contact angles greater (or smaller) than the advancing (or receding) CAs were replaced by their limiting values when the TCL was unpinned. On the other hand, if the CAs happened to be between the advancing and receding CAs, then the TCL was assumed to be pinned. Either way, the interface shape was recalculated after any modifications to the TCL condition. We incrementally decreased the distance between the plates down to a minimum distance of  $S_{\min}$  (compression) and recalculated the CAs on each plate at each increment to check if they were between the limiting values of advancing and receding CAs. Once the minimum distance was reached, we then separated the plates incrementally (stretching) up to a point where no equilibrium shape could be found. This was also seen in the experiment, where at some distance near the end of the stretching process, a spontaneous (irreversible) liquid bridge breakup had occurred. Note that CAs were recalculated every time the spacing between the plates was varied (to decide on whether pinning/unpinning condition for the TCL- line should be used).

## 4.4 Results and Discussion

### 4.4.1 Liquid Bridge between PS-Coated Horizontal Plates under Compression or Stretching

We start this section with an insightful discussion on the variation of the surface energy of a liquid bridge during compression and stretching. This is also accompanied with a validation study through comparing our results with those reported previously by Chen et al. [66].

Our simulations started with an initial spacing of 1,100  $\mu\text{m}$ , a volume of 2  $\mu\text{L}$ , and a YLCA of  $60^\circ$  on both plates, i.e., average of the advancing and receding CAs (we used the advancing and receding CAs of the surface in our simulations to determine which of the pinned or unpinned TCL was to be considered for a given spacing). The outputs of the SE simulations were the equilibrium shape of the liquid bridge and the mean curvature of the liquid bridge interface (hence the Laplace pressure), which were used to find the forces on the lower plate  $2\pi R_L \sigma \sin \theta_L - \pi R_L^2 \Delta P_L$ . Figure 4.5 shows liquid bridge profiles during the compression and stretching steps. The spacing between the plates and the radius of the bridge are given below each subfigure.



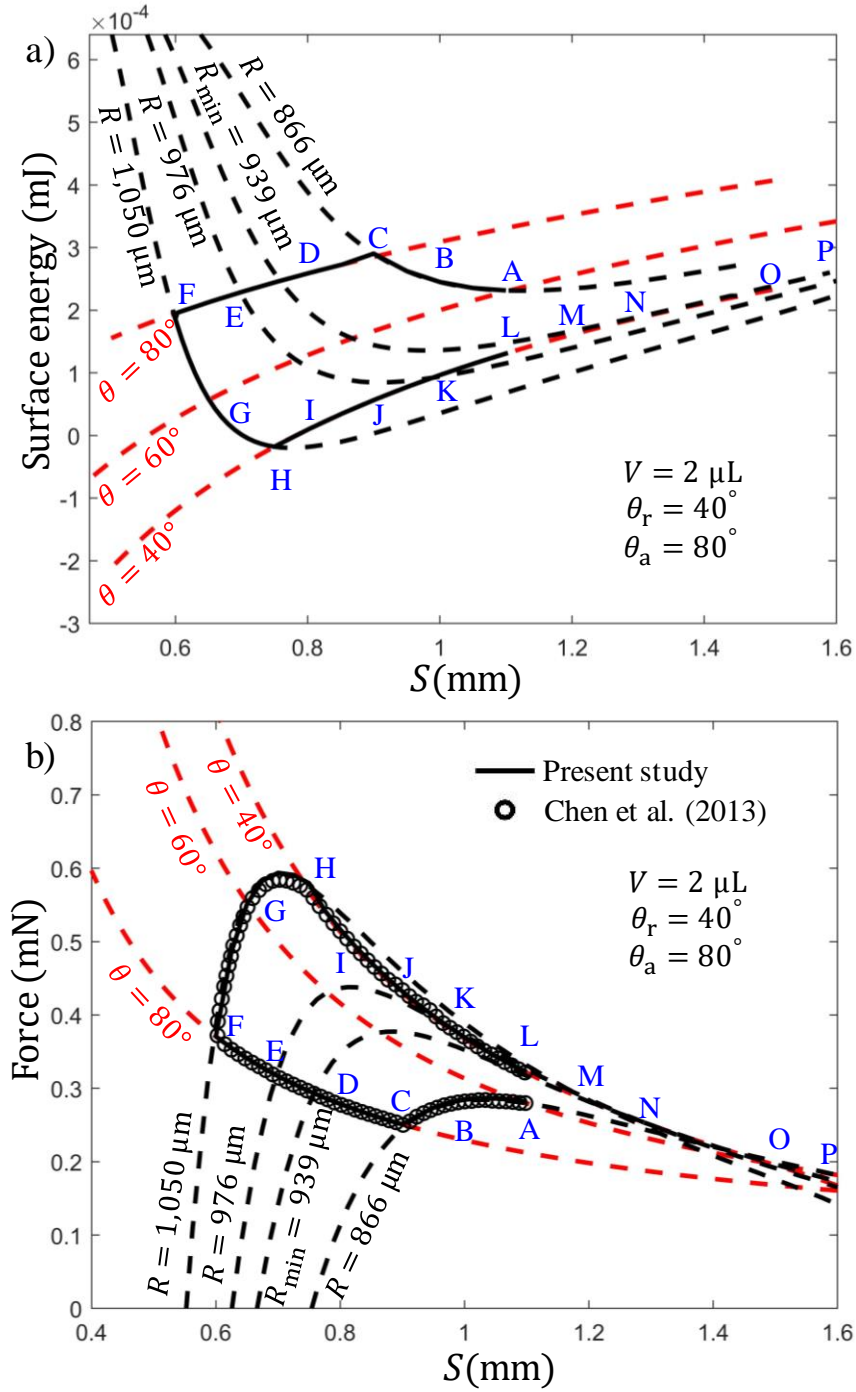
**Fig. 4.5:** Snapshots of a liquid bridge with a volume of  $2 \mu\text{L}$  are shown at different spacing distance between two identical plates with advancing and receding CAs of  $80$  and  $40^\circ$ , respectively. Spacing between the plates, radius of the contact area, and the liquid CA are given underneath each subfigure.

Figure 4.6a shows the surface energy ( $\sigma A_{LG} - \sigma \cos \theta_L A_{SL}^L - \sigma \cos \theta_U A_{SL}^U$ ) of the liquid bridge at different spacings while Figure 4.6b presents the same process on a force–spacing plot. For the latter, we also included the force predictions of Chen et al. [66] for comparison. Also, added to these figures are the  $\theta$ -constant (unpinned TCL) and  $R$ -constant (pinned TCL) lines to map the compression–stretching process and provide insight into the physics of the problem. During the initial stages of the liquid bridge compression from point A (where both surfaces have an average CA of  $60^\circ$  and lay on the  $\theta = 60^\circ$  line), the TCL was pinned (compression takes the liquid bridge

along the  $R = 866 \mu\text{m}$  line) while the CA was allowed to increase and reach the advancing CA at a distance of  $900 \mu\text{m}$  at point C, which is the intersection of the  $R = 866 \mu\text{m}$  line and advancing CA line (i.e.,  $\theta = 80^\circ$  line) (note the increase in the surface energy of the system during the pinned compression process from A to C). The TCL was then unpinned and allowed to move with the advancing CA until a minimum spacing of  $600 \mu\text{m}$  was reached at point F (note the decrease in the system energy; almost all the energy stored by the system during the pinned compression was spent in this process). The stretching process started from point F with an initially pinned TCL. The CA decreased along the F-to-H travel to reach the receding CA at point H. Note the decrease in system's surface energy moving down even to negative values (meaning that the negative surface energy of the solid-liquid dominates the positive surface energy of the liquid-gas interface). Further stretching from this point resulted in TCL shrinking with the receding CA (from point H to point L). Note that the surface energy of the system was increased from H to L meaning that some work was done on the system. It is interesting to note that point L has a lower energy compared to that of point A. This means that after one compression-stretching cycle, the liquid bridge will be at a lower energy state. Also seen is that for any two points with identical spacing (e.g., B-K or C-J), state of energy during stretching is lower than that during compression. It should be noted that the liquid bridge shape variations are reversible from point F to H or on any other  $R$ -constant lines. For instance, liquid bridge reverts to the same point along the same path (point F) if one increases the spacing between the plates from  $600 \mu\text{m}$  to  $700 \mu\text{m}$  (from point F to point G) and then back to  $600 \mu\text{m}$ . On the other hand, the shape variations are irreversible on the  $\theta$ -constant lines when reducing the spacing from  $900 \mu\text{m}$  to  $600 \mu\text{m}$  (point C to point F), and then stretch back to the same height. In this case, the liquid bridge does not retrieve its initial state at point C, but instead takes the F-H-J path to point J. Evidently, the  $\theta$ -constant and  $R$ -constant lines also

predict the pinning span in the compression or stretching processes. For instance, stretching the liquid bridge from point E, the TCL remains pinned up to the height at which the  $R = 976 \mu\text{m}$  line intersects with the  $\theta = 40^\circ$  line (the receding line).

Another important behavior to point out is the TCL pinning at the end of the stretching process, which often happens for hydrophilic surfaces. In such cases, the TCL recedes until its radius decreases to a minimum value  $R_{\min}$  (was also discussed in the model of [66] and the experiments of [160]).  $R_{\min}$  depends on liquid volume as well as the receding CA of the surface. For the liquid bridge considered in Figure 4.6, the minimum contact radius of  $R_{\min} = 939 \mu\text{m}$  was obtained. Hence, the pinning at the end of the stretching process starts at the intersection of the  $\theta_r = 40^\circ$  and  $R_{\min} = 939 \mu\text{m}$  lines, and the CA increases with further stretching (from point N to point P). Note that since the  $\theta$ -constant and  $R$ -constant lines approach one another at higher spacing values, the choice of pinned vs. unpinned TCL becomes less significant for force prediction (but it is important in predicting the liquid bridge profile). The  $R$ -constant (or  $\theta$ -constant) lines are obtained from separate simulations with the assumption of a constant contact-line radius (or CA) for all spacing. Such simulations can be repeated for different CAs and contact-line radius to fabricate a mapped force-spacing plot. Such a plot allows the user that needless of running simulation (or solving the Young-Laplace equation), just using the surface advancing and receding CA and the  $R_{\min}$  lines with the abovementioned discussion, predict the adhesion force (as well as the liquid bridge profile) at any spacing.



**Fig. 4.6:** Surface energy of the system is given in (a). Also, shown in (a) is the  $R$ -constant and  $\theta$ -constant lines. Comparison between the current numerical simulations and those from [66] are given in (b) in a force–spacing diagram.

As mentioned earlier, our experimental setup was comprised of two flat plates. The lower plate was placed on a sensitive scale while the other one was mounted on a height gauge. For the

experiment, a droplet was deposited on the lower plate and the scale was immediately zeroed. When compressing or stretching the liquid bridge, the force exerted to the lower plate by the liquid bridge was recorded by the scale. For the experiments reported in this section, we used plates coated with PS fibers. PS electrospun coatings are known for their superhydrophobicity, and depending on the spacing between the fibers, fiber diameter, and the chemistry of the PS fibers (e.g., choice of solvent or solution concentration) a water droplet may exhibit a behavior associated with the Cassie (almost dry) or the Wenzel (wetted) state. A droplet at the Cassie state is mainly in contact with air and requires less force to move on the surface compare to a droplet at the Wenzel. In our liquid bridge experiment, we believe that droplets cannot remain in the Cassie state during the compression process even though they may also not reach a fully-wetted (fully Wenzel) state [4,154,161-165]. To assign advancing and receding CAs to these surfaces, we used the inflation–deflation method, i.e., we incrementally increased the volume of a droplet on the surface (upon injecting more liquid into the droplet by a syringe) and monitored its profile using a camera. The CA at which droplet’s TCL moved on the surface was then taken as the advancing CA for that droplet–surface combination. Similarly, we decreased the volume of the droplet (upon taking in some portion of the droplet back to the syringe), and monitored the TCL motion. The angle at which droplet’s TCL started shrinking was taken as the receding CA. Figures 4.7a and 4.7b present experimental and computational results for when the upper and lower plates were coated with electrospun PS (hydrophobic) fibers. For these simulations, we considered an advancing CA of  $131^\circ$  for both the upper and lower surfaces at a spacing of  $1,240\ \mu\text{m}$  in the presence of gravity. The droplet was compressed to a spacing of  $940\ \mu\text{m}$  and then stretched till the breakup point.

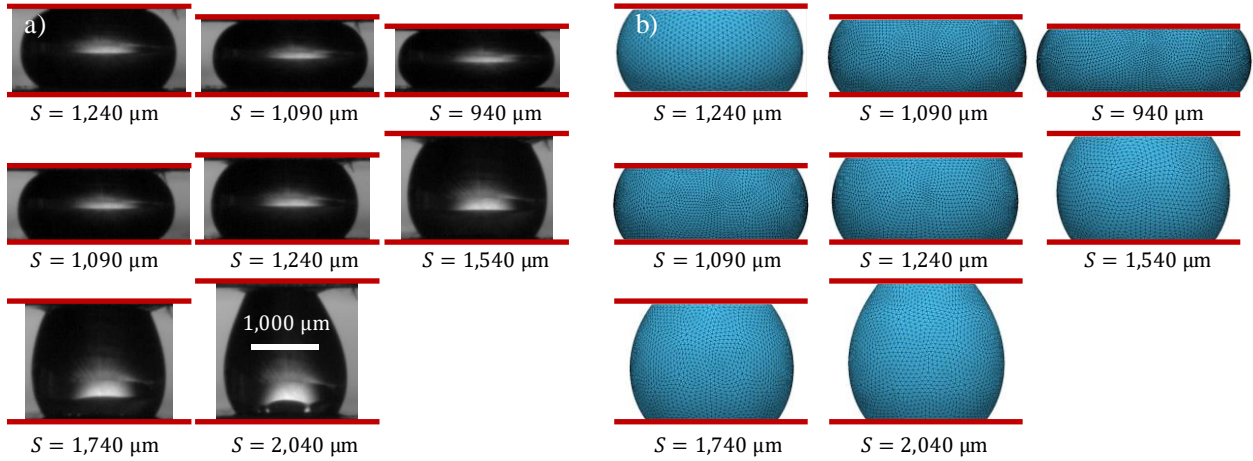


**Fig. 4.7:** Snapshots of a liquid bridge between two horizontal plates coated with electrospun PS fibers (with advancing and receding CAs of  $131^\circ$  and  $125^\circ$ , respectively) are given in (a) along with their computational counterparts in (b) at different spacing.

Figure 4.8a compares the force exerted on the lower plate from simulation with that from experiment. The discrepancy between the predicted and measured forces can be attributed to the non-uniformity of the PS coating (see the inset of this figure), which can introduce inconsistency in our advancing/receding CA measurements (inputs to the model). Different  $\theta$ -constant lines are also added to the figure for the sake of illustration.  $R$ -constant lines are not plotted, since in the presence of gravity the radius of the TCL on the upper plate is different from that on the lower one and assigning a single  $R$ -constant is not relevant. It can be seen in Figure 4.8b that,  $F_p$  becomes larger than  $F_{CL}$  at low spacing values, which provides a negative net force on the lower plate (i.e., liquid bridge exerts a compressive force on the lower plates at small spacing). Stretching the liquid bridge causes the force to change sign at some point.

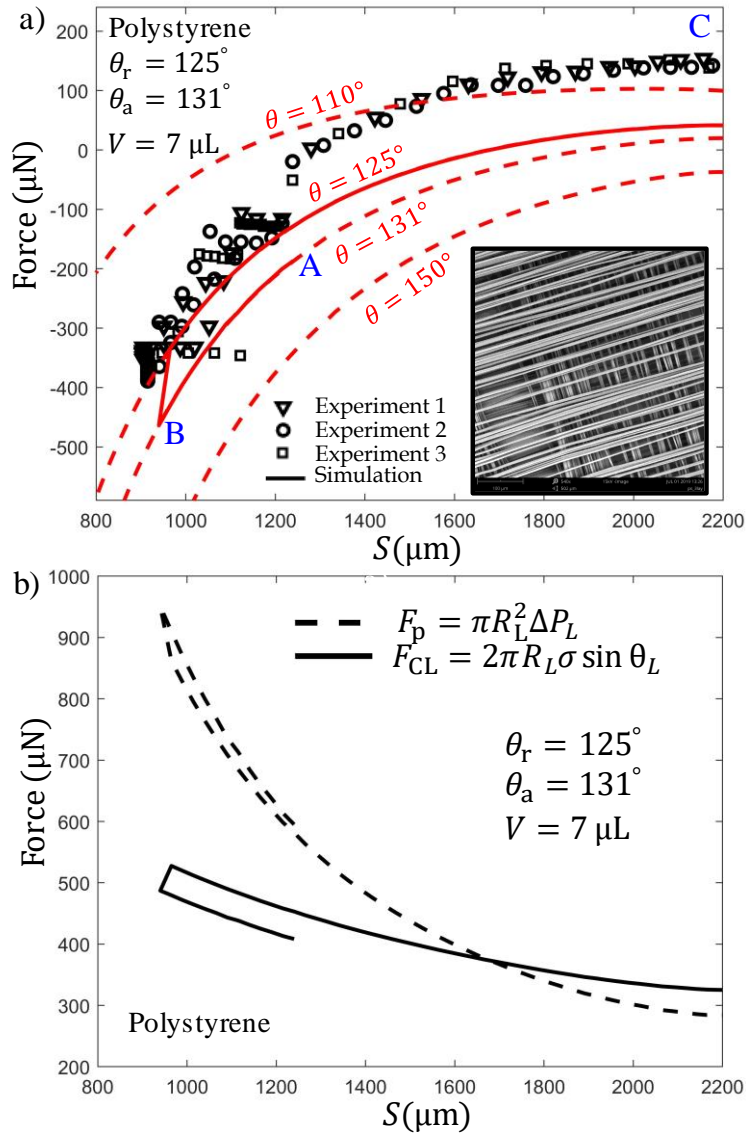


**Fig. 4.8:** The measured and predicted adhesion forces on the lower plate are shown in (a). Predicted capillary and pressure forces on the lower plate are compared with one another in (b).

Figure 4.9a presents simulation results for the effects of minimum spacing between the plates on the force exerted by the liquid bridge. It is interesting to note that the equilibrium shape of the liquid bridge during stretching can be different from that during compression for a given spacing (e.g., see the two different liquid bridge profiles at  $S = 1,090 \mu\text{m}$  in Figure 4.7b) due to CAH. This results in a force–spacing path during stretching different from that during compression (Figure

4.9a). Effects of varying liquid volume on force–spacing behavior were also simulated and are shown in Figure 4.9b. It can be seen that increasing liquid volume results in an increase in the force magnitude. This is because a larger droplet has a longer TCL (for a given spacing between the plates), which results in a larger capillary force.

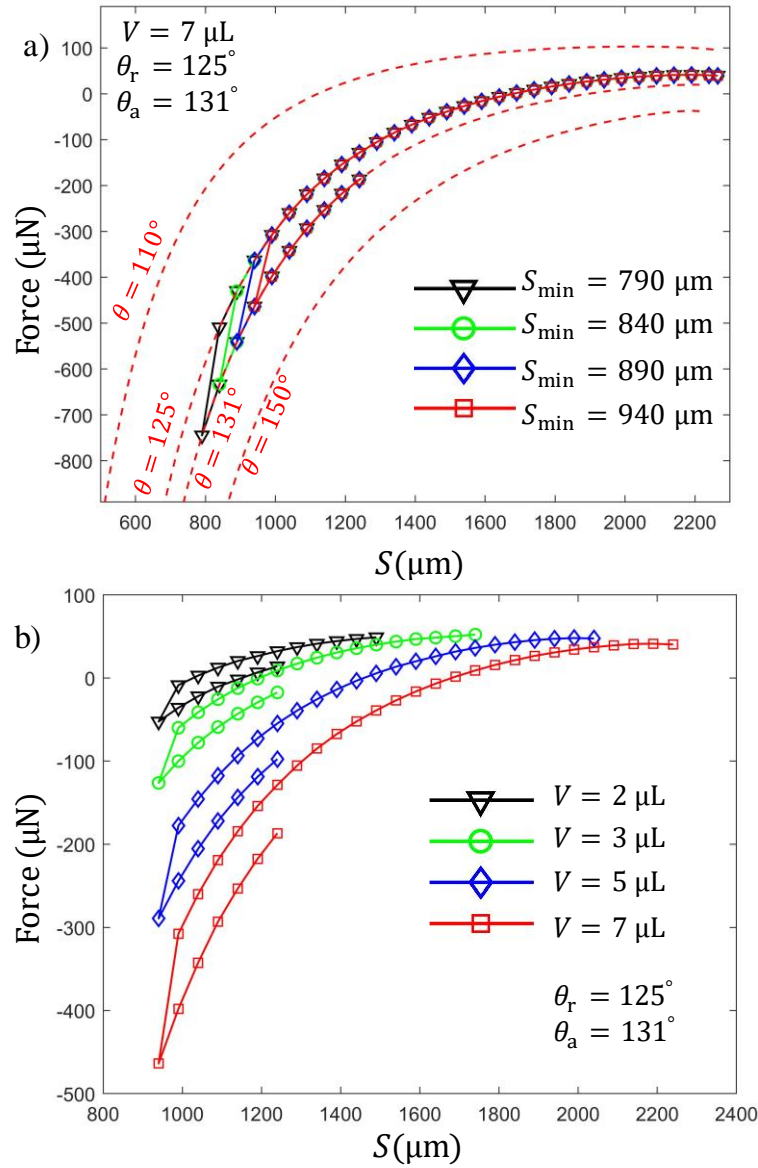


**Fig. 4.9:** Panel (a) shows the predicted adhesion force on the lower plate for when a liquid bridge with a volume of  $7 \mu\text{L}$  is compressed to different minimum spacing values before stretching. Panel (b) shows similar results for liquid bridge with different volumes but an identical minimum spacing of  $940 \mu\text{m}$ .

The results presented in Figures 4.5 through 4.9 quantitatively describe the relative importance of parameters like advancing and receding CAs in describing the interaction of a droplet with plates. Note that liquid interaction with a plate is different from that with fibers where because of fibers' round geometry, pinning is not crucial and that interaction is often described with a single YLCA value [166-167].

It is also interesting to compare the force exerted on the plates near the moment of liquid bridge breakup with that required to detach a sessile droplet from the same (or similar) surface. Following the work of [168], we deposited a water-based ferrofluid droplet with a volume of 7  $\mu\text{L}$  on one of our PS-coated plates and placed the assembly on the scale. We zeroed the scale and detached the droplet vertically by bringing a permanent magnet close to the droplet from above. The force recorded by the scale (minus droplet weight) was then taken as the force of detachment for the droplet. To account for the differences between the physical properties of the water-based ferrofluid and the liquid used in our liquid bridge experiments (15% glycerol in DI water), we scaled the measured force using droplets bond number ratios [169-170],

$$F_{wg} = F_f \left( \frac{\sigma_{wg}}{\sigma_f} \right)^{\frac{1}{2}} \frac{\rho_f}{\rho_{wg}} \left( \frac{V_f}{V_{wg}} \right)^{\frac{2}{3}} \quad (4.12)$$

where subscripts  $f$  and  $wg$  denote ferrofluid and water–glycerol solution, respectively.  $F_f$  is the detachment force from the experiment with the ferrofluid droplets, and  $F_{wg}$  is the scaled value. The force applied by the magnet was measured to be  $F_f = 200 \pm 30 \mu\text{N}$ , which scales to  $F_{wg} = 214 \pm 32 \mu\text{N}$  for a water–glycerol droplet. The force applied to the lower plate at the moment of the liquid bridge breakup was found to be 170  $\mu\text{N}$  on average for the PS-coated plates, which is within 20% of the force of sessile droplet detachment. The difference between these two values can be

attributed to the differences between the profile of a detaching sessile droplet and that of a liquid bridge near the breakup moment. A similar difference was also reported in [158] for droplet detachment from a single fiber using a magnet as opposed to using another fiber (i.e., a liquid bridge between two fibers).

#### 4.4.2 Liquid Bridge between PU-Coated Vertical Plates under Shear

In this section, we study how a liquid bridge behaves in response to a tangential (shear) force. For this study, we slightly modified our test setup to move the plates in a direction parallel to one another. We also mounted the plates vertically so that the shear force could be measured by the scale (see Figure 4.10).

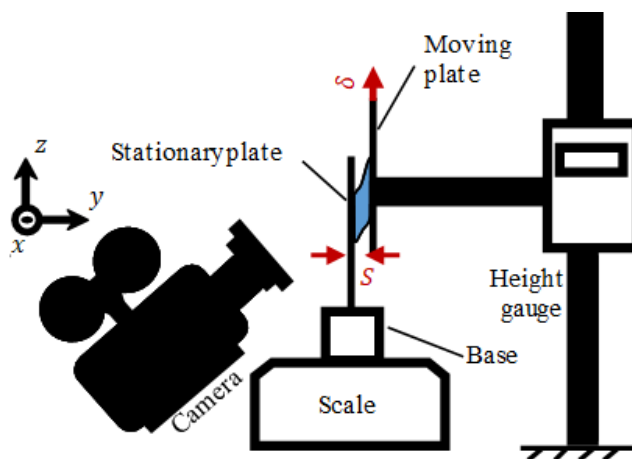


**Fig. 4.10:** Schematic drawings for the setup used for liquid bridge shear experiment.

In this section, we consider Polyurethane (PU) electrospun coatings as the PS coatings seemed to remain at a near-Cassie state with the extent of wetting dependent strongly on the spacing between the plates, non-uniformity of the coatings, size of the droplet, and other practical factors (leading to drastic variation in the results from one experiment to the other). PU coatings were produced by electrospinning from a PU-in-THF solution with a concentration of 5% at an infusion rate of 8.33

$\mu\text{L}/\text{min}$  using a positive voltage of 12 kV on Aluminum substrates. The experiment started by depositing a droplet with a given volume on one of the plates (for a droplet with a volume less than  $9 \mu\text{L}$ , pinning of the fibrous surfaces was large enough to keep the droplet from sliding down or falling in our experiments). The other plate was then brought into contact with the droplet and compressed it to a spacing of  $S$ . The scale was then zeroed and the shearing process was started by moving the plate mounted on the height gauge relative to the one placed on the scale. The changes in the scale readings were recorded at each displacement  $\delta$  and attributed to the shear force. We also simulated the process of shearing a liquid bridge to better understand and analyze the forces involved in this process. Unlike the case of a liquid bridge subjected to vertical forces, the liquid bridge literature is very scarce when it comes to modeling shearing forces. This is in part because solving the Young–Laplace equation becomes challenging when the CA varies around the TCL due to liquid bridge profile becoming asymmetric when the shear forces are vertical. We have therefore considered some simplifying assumptions to ease the simulation problems. Based on our experimental observations, we have assumed that the TCL on the stationary plate (left plate) remains pinned, and the wetted area on this plate has a circular shape mathematically described by  $x = R_S \cos \phi$ ,  $y = 0$ , and  $z = R_S \sin \phi$ . Moreover, we have assumed that the wetted area on the moving plate is also circular with a radius of  $R_M$  when  $\delta = 0$ . The center of this circular area is assumed to be below the origin by a distance of  $\Delta z_i$ . Upon moving the right plate, the length of wetted area is assumed to become elongated in the direction of motion (the  $z$ -direction), but to remain almost unchanged in the lateral direction (the  $x$ -direction). We therefore, considered an elliptical contact area for the bridge on the moving plate with a minor axis of  $b(\delta) = 2R_M$  and a major axis of  $a(\delta) = 2R_M + \delta$ . In the parametric form therefore, one can write,

$$x = R_M \cos \phi \tag{4.13}$$

$$y = S \quad (4.14)$$

$$z = (R_M + \delta/2) \sin \phi + (\delta - \Delta z_i) \quad (4.15)$$

Therefore,  $R_S$ ,  $R_M$ , and  $\Delta z_i$  should be estimated before the liquid bridge profile between the plates can be predicted at each  $\delta$ . To this aim, we start with a given liquid volume having a spherical cap profile with an YLCA of  $97^\circ$  (average CA for a droplet on the PU coatings) to estimate the radius of the TCL,

$$a = \left( \frac{3V}{\pi(2+\cos\theta)(1-\cos\theta)^2} \right)^{1/3} \sin \theta \quad (4.16)$$

where  $a$  is the radius of TCL as shown in Figure 4.11.

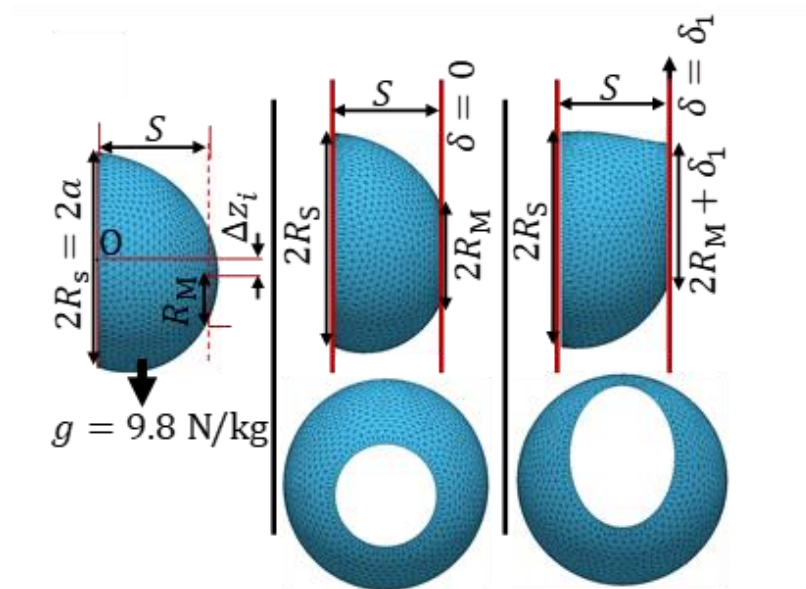


**Fig. 4.11:** Geometrical assumptions considered in setting up a numerical simulation to predict the behavior of a liquid bridge under shear and in the presence of gravity.

We then use this radius to simulate the equilibrium shape of a droplet on a vertical wall under the influence of gravity. With the droplet shape obtained, we slice the droplet profile with a vertical

plate located at a distance of  $S$  from the left plate (based on the setting from experiment) to obtain the abovementioned wetted area on the moving plate at  $\delta = 0$ . The elliptical wetted area on the moving plate can then be calculated for any displacement  $\delta$  using Equations 4.13–4.15. Figure 4.12 compares simulation results for a liquid bridge with a volume of  $7 \mu\text{L}$  between PU coatings with a spacing of  $S = 1,400 \mu\text{m}$  at different displacements  $\delta$  to those from experiment. It should be mentioned that the best matching liquid bridge profiles from experiment (Figure 4.12a) and simulation (Figure 4.12b) were not observed at the same exact  $\delta$  values. We believe this is because of our simplifying assumptions considered for the simulations (e.g., elliptical contact area) as well as the errors associated with liquid wicking into the pores of the PU coatings during the experiments. Despite the less-than-perfect agreement between the simulated and imaged bridge profiles, our simulations can be used to estimate the force of adhesion between the plates during the experiment.

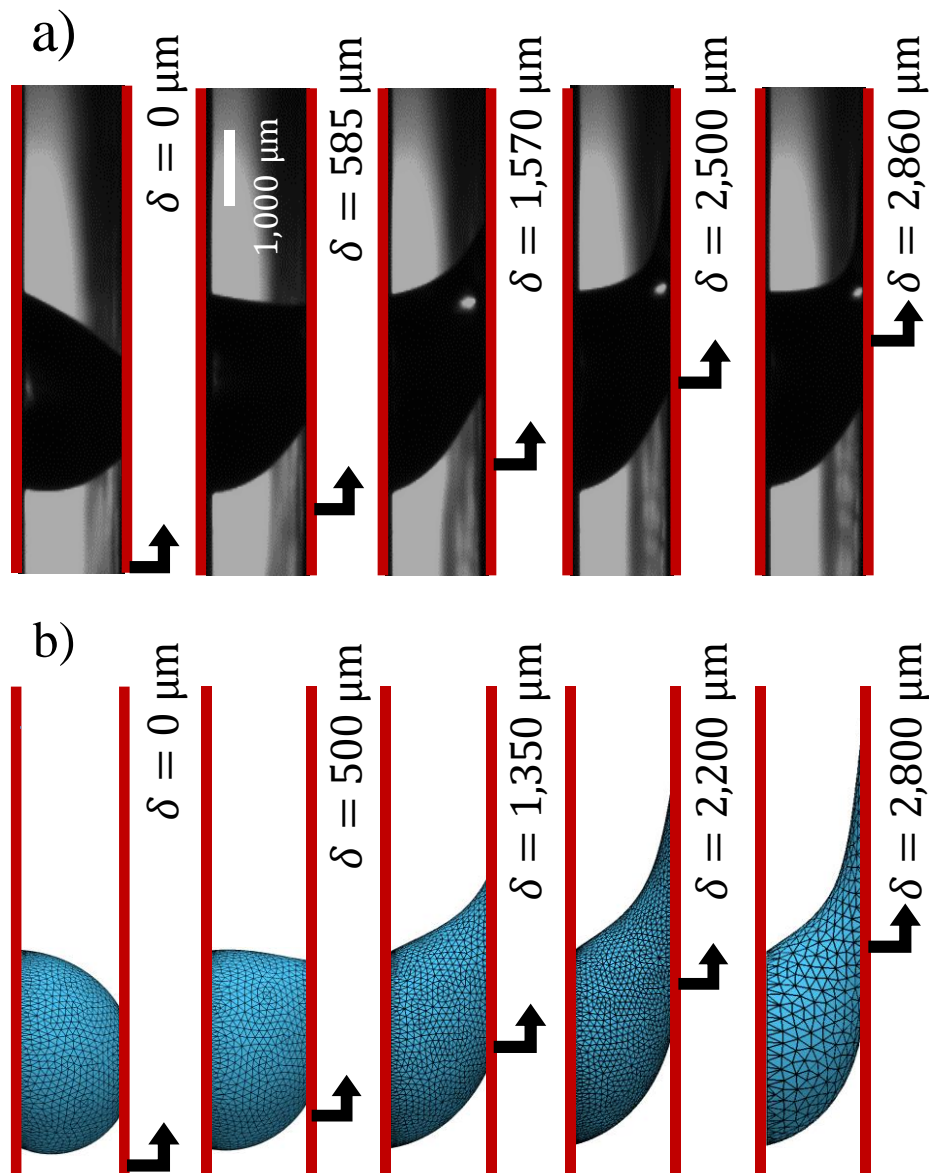


**Fig. 4.12:** Snapshots of the experiment with a liquid bridge with a volume of  $7 \mu\text{L}$  between two vertical plates having a spacing of  $1,400 \mu\text{m}$  and coated with electrospun PU fibers are shown in (a). Predictions of the liquid bridge profile from our numerical simulations are given in (b) for different plate displacements.

Note however that, the force calculation formula discussed earlier (Equations 4.2–4.3) cannot be used here for shear force calculation. Also, note that the pressure force (Laplace pressure) has no component in the tangential (vertical) direction, and so the shear force is merely the summation of

capillary forces around the TCL. Therefore, to calculate these forces we have developed a new set of equations. Let  $\hat{n} = (v_1, v_2, v_3)$  be the normal vector of the facet along the TCL (shown in red or blue in Figure 4.13a) and  $\vec{m} = (e_x, e_y, e_z)$  be the vector of the line segment connecting two consecutive grid points on the TCL. Then, the direction in which the surface tension force applies is the vector normal to  $\hat{n}$  and  $\vec{m}$ , which can be found as  $\vec{l} = \hat{n} \times \vec{m}$ . The angles this direction make with the  $x$ -,  $y$ -,  $z$ -axes are  $\alpha = \text{acos}(\vec{l} \cdot \hat{i})$ ,  $\beta = \text{acos}(\vec{l} \cdot \hat{j})$  and  $\gamma = \text{acos}(\vec{l} \cdot \hat{k})$ , respectively. Therefore, balance of the forces on the plate (left or right) can be written as (see Figure 4.13a),

$$\sum F_x = \sum_i \sigma \cos \alpha_i \sqrt{e_{x,i}^2 + e_{z,i}^2} = 0 \quad (4.17)$$

$$\sum F_y = \int_{\text{CL}} x(p_o - \rho g z) dz - \sum_i \sigma \cos \beta_i \sqrt{e_{x,i}^2 + e_{z,i}^2} = 0 \quad (4.18)$$

$$\sum F_z = F_\delta - \sum_i \sigma \cos \gamma_i \sqrt{e_{x,i}^2 + e_{z,i}^2} = 0 \quad (4.19)$$

Therefore, the component of the force in the shear direction ( $F_\delta$ ) can be found as,

$$F_\delta = \sum_i \sigma \cos \gamma_i \sqrt{e_{x,i}^2 + e_{z,i}^2} \quad (4.20)$$

The subscript  $i$  denotes the distance between two consecutive grid points on the TCL with  $e_x$  and  $e_z$  being its components in the  $x$  and  $z$  directions, respectively (note that  $e_y = 0$ ). The total shear force can then be obtained by summing all the individual forces along the TCL for each plate. The shear force calculated for the left and right plates are shown in Figure 4.13b. As expected from the free body diagram shown in the inset, the difference between these forces at any displacement is equal to the weight of the droplet. Figure 4.13c shows the effects of spacing on the measured shear force for plates coated with electrospun PU coatings. It can be seen that, for a given volume of  $V =$

7  $\mu\text{L}$ , decreasing the spacing between the plates results in an increase in the shear force. This is because decreasing the spacing increases the wetted area (and the length of TCL) on the plates, which results in larger force transfer between the plates. Note that, we zeroed the scale prior to displacing the second plate (and so the recorded forces start from zero). To mimic the effect of zeroing the scale when reporting the simulation results, the computed tangential force at  $\delta = 0$  is subtracted from the simulation data shown in Figure 4.13c. Note from the balance of forces that,  $F_{\delta}^R = F_{\delta}^L + mg$  (and  $F_{\delta=0}^R = F_{\delta=0}^L + mg$ ), and therefore, the changes in the shear force on the left plate (shown on the vertical axis in Figures 4.13c and 4.13d) are the same as those on the right plate, i.e.,  $F_{\delta}^R - F_{\delta=0}^R = F_{\delta}^L - F_{\delta=0}^L$ . Effects of liquid volume on the shear force are shown in Figure 4.13d, and they clearly show that shear forces are larger for larger liquid volumes. This is because for a given spacing, larger droplets will form larger TCLs and so larger adhesion forces. Simulation results for each droplet volume is also shown with solid lines.

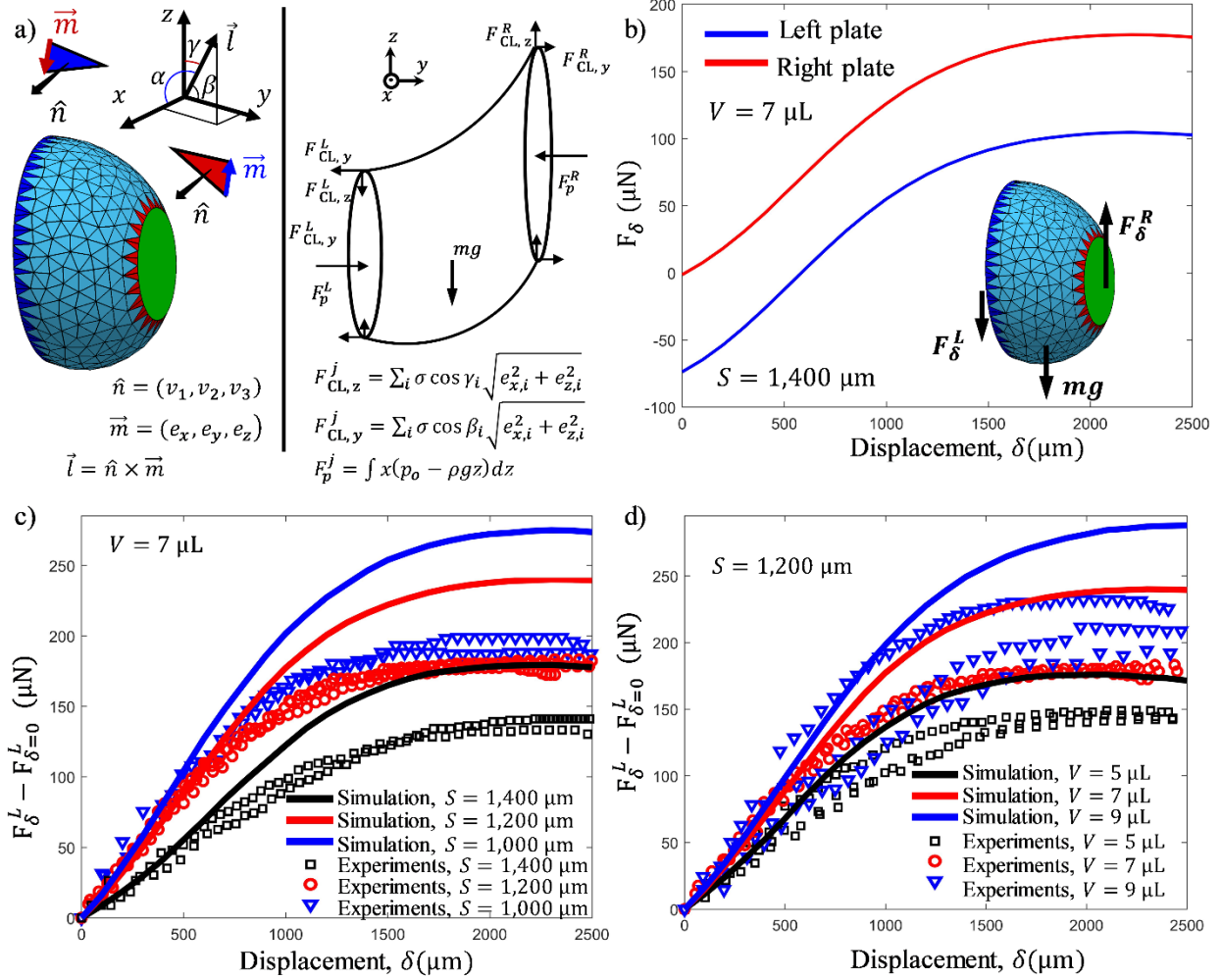


**Fig. 4.13:** Illustration of the facets on the TCL (red) considered to find the local direction of the surface tension forces around the TCL is given in (a) along with a free body diagram for the forces acting on a liquid bridge under vertical shear. Tangential forces exerted from left and right to a liquid bridge with a volume of  $7 \mu\text{L}$  placed between two vertical plates coated with electrospun PU fibers with a spacing of  $1,400 \mu\text{m}$  are shown in (b). Shear force exerted on the left plate by a liquid bridge with a volume of  $7 \mu\text{L}$  at different spacings are shown in (c). Shear force exerted on the left plate by liquid bridges with different volumes but for a fixed spacing of  $1,200 \mu\text{m}$  between the plates are given in (d). The solid lines are the force predictions from simulations (obtained with the assumption of pinned TCL throughout the process) and the symbols are from experiment.

## 4.5 Conclusions

Liquid bridge and the adhesion force between fibrous surfaces made of PS or PU fibers were investigated in this work both experimentally and numerically. This was achieved by placing a water droplet (containing 15% glycerol) on a plate coated with PS or PU fibers and compressing, stretching, or shearing it using another coated plate. The axial or tangential forces exerted on the plates were measured using a sensitive scale and they were compared to their numerical counterparts obtained from the Surface Evolver code modified to include the CAH effect in the simulations. Reasonable agreement was achieved between the measured and simulated forces, despite the inherent non-uniformity of the fibrous coatings and the simplifying assumptions considered to make numerical simulations affordable. While it is not very noticeable from the experiments with fibrous coatings (due to experimental noise), our simulations clearly show that the force-spacing trajectory of a liquid bridge during a compression–stretching process on a surface with CAH follows  $\theta$ -constant (unpinned CL) and  $R$ -constant (pinned CL) lines. It was also shown that the force–spacing trajectories during compression and receding processes are closer to one another when the surface CAH is smaller. Positive forces (attraction) were obtained for the hydrophilic surface for any spacing values, while for the hydrophobic surface both negative (repulsion) and positive (attraction) were measured (and predicted) depending on the spacing between the plates. Our simulations also show that surface energy of the system varies inversely with the magnitude of the attraction force between the liquid bridge and the surface. When shearing the liquid bridge, it was observed that the shear force increases with relative displacement between the plate until it reaches a plateau. Our results also revealed that increasing the liquid volume, or decreasing the spacing between the plates, leads to an increase in the shear force on the plates.

## Chapter 5. Overall Conclusion

The main goal of this thesis was to develop simulation method to predict capillary pressure/capillary forces in fibrous surfaces. Two different modeling approach was used in this work to predict capillary pressure in fibrous structures. we first presented a physics-based model to simulate the 3-D structure of fibrous mats on the basis of treating each fiber as an array of point masses connected to one another via springs and dampers. This allowed us to generate the most realistic virtual fibrous structures and solved the problem with most literature structure generation approaches by avoiding the unrealistic fiber-fiber overlaps. We then developed a model to estimate a LEP for hydrophobic fibrous membrane based on a simplifying assumption that the AWI remains both planar and intact as it penetrates inside the media, which makes it possible to estimate an LEP for media with complex morphological or wetting properties (an otherwise challenging problem). Our results revealed that the LEP of a fibrous membrane increases upon decreasing the diameter or increasing the contact angle of its constituting fibers. For the purpose of accurate prediction of the LEP of fibrous membranes, in this work, we also developed an interface tracking approach implemented in the Surface Evolver finite element code. We applied this method to fibrous structures comprised of orthogonally-oriented layers of parallel fibers. Our interface tracking method approach was able to resolve the shape and position of the AWI inside a fibrous membrane, as the approach was benchmarked with experimental results and 2-D simulations in the literature. Our simulation results showed that increasing the volume fraction of the fine fibers, or fibers with a higher YLCA, results in an increase in the intrusion pressure of the media. The simulation method also provided information about the relationship between intrusion pressure and depth of water penetration into the membrane which is of great significance in designing and optimizing the microstructure of a fibrous membrane to maximize LEP while being highly porous. The interface

tracking approach presented in this work could be a framework for future studies as one needs to apply the method to more complex structures like those generated by our mass-spring-damper approach.

Regarding the capillary forces on fibrous surfaces, we used the liquid bridge between fibrous surfaces (surfaces coated with PS or PU electrospun fibers) to measure or predict the adhesion force during compressing, stretching, or shearing of a 15% water-glycerol droplet laying on a plate using another plate. A sensitive scale was used in our force measurements and the results were compared to simulations obtained from a Surface Evolver code, which was modified to include the CAH and hence the contact line pinning or unpinning. Our simulation results showed that the force-spacing trajectory of a liquid bridge during a compression–stretching process on a surface with CAH follows  $\theta$ -constant (unpinned CL) and  $R$ -constant (pinned CL) lines. Regarding the effects of surface wettability it was shown that hydrophilic surfaces reveal positive forces (attraction) at any spacing values during the compression-stretching of the liquid bridge, while for hydrophobic surfaces could reveal both negative (repulsion) and positive (attraction) forces depending on the spacing between the plates. The surface energy of the solid-liquid-gas system was also studied in this work and was shown that the surface energy varies inversely with the magnitude of the attraction force between the liquid bridge and the surface. To shed some light on the tangential adhesion forces, the process of shearing the liquid bridge was also studied experimentally and numerically. Both measured and predicted results revealed that the shear force increases with relative displacement between the plate until it reaches a plateau. It was also seen that the shear force on the plates increases by increasing the liquid volume, or decreasing the spacing between the plates.

## Chapter 6. References

- 1-C.W. Extrand, Criteria for ultralyophobic surfaces, *Langmuir* 20, 5013–5018 (2004)
- 2-E. Bormashenko, Y. Bormashenko, T. Stein, G. Whyman, E. Bormashenko, Why do pigeon feathers repel water? Hydrophobicity of penna, Cassie-Baxter wetting hypothesis and Cassie-Wenzel capillarity-induced wetting transition, *J. Colloid Interface Sci.* 311, 212–216 (2007)
- 3-N.J. Shirtcliffe, G. McHale, S. Atherton, M.I. Newton, An introduction to superhydrophobicity, *Adv. Colloid Interf. Sci.* 161, 124–138 (2010)
- 4-B. Emami, H.V. Tafreshi, M. Gad-el-Hak, and G.C. Tepper, Effect of Fiber Orientation on Shape and Stability of Air–Water Interface on Submerged Superhydrophobic Electrospun Thin Coatings, *Journal of Applied Physics* 111, 064325 (2012)
- 5-Y Li, QY Zhu, Simultaneous heat and moisture transfer with moisture sorption, condensation, and capillary liquid diffusion in porous textiles, *Textile Research Journal*, 73, 6, 515-524 (2003)
- 6-I Eames, I Small, A Frampton, AM Cottenden, Experimental and theoretical study of the spread of fluid from a point source on an inclined incontinence bed-pad, *Proceedings of The Institution of Mechanical Engineers Part H-Journal of Engineering in Medicine*, 217, H4, 263-271 (2003)
- 7-M. Landeryou, I Eames, A Cottenden, Infiltration into inclined fibrous sheets, *J Fluid Mechanics* 529, 173-193 (2005)
- 8-S. Jaganathan, H.V. Tafreshi, and B. Pourdeyhimi, A Realistic Micro- and Macroscale Modeling of Fluid Infiltration in Thin Fibrous Sheets, *Journal of Applied Physics* 105, 113522 (2009)
- 9-A. Ashari, T.M. Bucher, H.V. Tafreshi, M. A. Tahir, and M.S.A. Rahman, Modeling Fluid Absorption in Thin Fibrous Sheets: Effects of Fiber Orientation, *International Journal of Heat & Mass Transfer* 53, 1750 (2010)
- 10- SJ Kim, JW Choi, M-W Moon, K-R Lee, YS Chang, D-Y Lee, and H-Y Kim, Wicking and flooding of liquids on vertical porous sheets, *PHYSICS OF FLUIDS* 27, 032105 (2015)
- 11- G. Hanna, W.J.P. Barnes, Adhesion and detachment of the toe pads of tree frogs, *J. Exp. Biol.* 155 (1991) 103–125.
- 12- B.N.J. Persson, Wet adhesion with application to tree frog adhesive toe pads and tires, *J. Phys.: Condens. Matter*, Matter 19 (2007) 376110.
- 13- G. Huber, H. Mantz, R. Spolenak, K. Mecke, K. Jacobs, S. N. Gorb, Evidence for capillarity contributions to gecko adhesion from single spatula nanomechanical measurements, *Proc. Natl. Acad. Sci. U.S.A.* 102 (2005) 16293–16296.
- 14- J.K. Hwang, S. Cho, J.M. Dang, E.B. Kwak, K. Song, J. Moon, M.M. Sung, Direct nanoprinting by liquid-bridge-mediated nanotransfer moulding, *Nat. Nanotech.* 5 (2010) 742–748.

- 15- H.W. Kang, H.J. Sung, T-M. Lee, D-S. Kim, C-J. Kim, Liquid transfer between two separating plates for micro-gravure-offset printing, *J. Micromech. Microeng.* 19 (2009) 015025.
- 16- Theo G. M. van de Ven, Capillary forces in wet paper, *Ind. Eng. Chem. Res.* 2008, 47, 7250–7256.
- 17- Y. Men, X. Zhang, W. Wang, Capillary liquid bridges in atomic force microscopy: Formation, rupture, and hysteresis, *J. Chem. Phys.* 131 (2009) 184702.
- 18- L. Wang, T.J. McCarthy, Shear distortion and failure of capillary bridges. Wetting information beyond contact angle analysis, *Langmuir* 2013, 29, 7776–7781.
- 19- P.G. de Gennes, F. Brochard-Wyart, D. Quéré, *Capillarity and Wetting Phenomena: Drops, Bubbles, Pearls, Waves*, Springer-Verlag, New York, (2004).
- 20- T. Young, An Essay on the Cohesion of Fluids, *Philos Trans R Soc Lond.* 1805;95:65–87.
- 21- Brown RA, Scriven LE. On the multiple equilibrium shapes and stability of an interface pinned on a slot. *J. Colloid Interface Sci.* 1980;78(2):528 – 542.
- 22- Lobaton EJ, Salamon TR. Computation of constant mean curvature surfaces: Application to the gas-liquid interface of a pressurized fluid on a superhydrophobic surface. *J. Colloid Interface Sci.* 2007;314(1):184 – 198.
- 23- Emami B, Tafreshi HV, Gad-el-Hak M, Tepper GC. Predicting shape and stability of airwater interfaces on superhydrophobic surfaces with randomly distributed dissimilar posts. *Appl. Phys. Lett.* 2011;98:203106.
- 24- Ershov D, Sprakel J, Appel J, Stuart MAC, van der Gucht J. Capillarity induced ordering of spherical colloids on an interface with anisotropic curvature. *PNAS.* 2013;110(23):9220 – 9224.
- 25- Lee C, Choi C-H, Kim C-J, Structured surfaces for giant liquid slip. *Phys. Rev. Lett.* 2008;101:064501.
- 26- Shirtcliffe NJ, McHale G, Newton MI, Chabrol G, Perry CC. Dual-scaleroughness produces unusually water-repellent surfaces. *Adv. Mater.* 2004;16:1929–1932.
- 27- Tuteja A, Choi W, Mabry JM, McKinley GH, Cohen RE. Robust omniphobic surfaces. *Proc. Natl. Acad. Sci. U.S.A.* 2008;105:18200.
- 28- Ma ML, Hill RM, Rutledge GC. A review of recent results on superhydrophobic materials based on micro- and nanofibers. *J. Adhes. Sci. Technol.* 2008;22:1799.
- 29- Emami B, Tafreshi HV, Gad-el-Hak M, Tepper GC. Simulation of meniscus stability in superhydrophobic granular surfaces under hydrostatic pressures. *Colloid Surf. A.* 2011;385:95–103.

- 30- Samaha MA, Ochanda F, Tafreshi HV, Tepper GC, Gad-el-Hak M. In-situ non-invasive characterization of superhydrophobic coatings. *Rev. Sci. Instrum.* 2011;82:045109.
- 31- Samaha MA, Tafreshi HV, Gad-el-Hak M. Effects of hydrostatic pressures on drag reduction performance of submerged aerogel particle coatings. *Colloid Surf. A.* 2012;399:62–70.
- 32- Bormashenko E. Progress in understanding wetting transitions on rough surfaces. *Advances in colloid and interface science.* 2015;222:92–103.
- 33- Eick JD, Good RJ, Neumann AW. Thermodynamics of contact angles. 2. Rough solidsurfaces. *J. Colloid Interface Sci.* 1975;53:235–248.
- 34- He B, Patankar NA, Lee J. Multiple equilibrium droplet shapes and design criterion for rough hydrophobic surfaces. *Langmuir.* 2003;19:4999–5003.
- 35- Long J, Hyder MN, Huang RYM, Chen P. Thermodynamic modeling of contact angles on rough, heterogeneous surfaces. *Adv. Colloid Interface Sci.* 2005;118:173–190.
- 36- Wenzel RN. Resistance of solid surfaces to wetting by water. *Ind. Eng. Chem.* 1936;28:988–994.
- 37- Cassie ABD, Baxter S. Wettability of porous surfaces. *Trans. Faraday Soc.* 1944;40:0546–0550.
- 38- Marmur A. Wetting on the hydrophobic rough surfaces: To be heterogeneous or not to be?. *Langmuir.* 2003;19:8343 – 8348.
- 39- C.W. Extrand, Repellency of the lotus leaf: resistance to water intrusion under hydrostatic pressure, *Langmuir* 27 (2011) 6920–6925.
- 40- Jian-Gang Lu, You-Fei Zheng, Min-Dong Cheng, Wetting mechanism in mass transfer process of hydrophobic membrane gas absorption, *J. Memb. Sci.* 308 (2008) 180–190.
- 41- Zhe-Qin Dong, Xiao-hua Ma, Zhen-Liang Xu, Wen-Ting You, Fang-bing Li, Superhydrophobic PVDF–PTFE electrospun nanofibrous membranes for desalination by vacuum membrane distillation, *Desalination* 347 (2014) 175–183.
- 42- Y. Liao, Chun-Heng Loh, R. Wang, A.G. Fane, Electrospun superhydrophobic membranes with unique structures for membrane distillation, *ACS Appl. Mater. Interfaces* 6 (2014) 16035–16048.
- 43- Y. Liao, R. Wang, A.G. Fane, Fabrication of bioinspired composite nanofiber membranes with robust superhydrophobicity for direct contact membrane distillation, *Environ. Sci. Technol.* 48 (2014) 6335–6341.

- 44- F. Guo, A. Servi, A. Liu, K.K. Gleason, G.C. Rutledge, Desalination by membrane distillation using electrospun polyamide fiber membranes with surface fluorination by chemical vapor deposition, *ACS Appl. Mater. Interfaces* 7 (2015) 8225–8232.
- 45- Y. Li, F. Yang, J. Yu, B. Ding, Hydrophobic fibrous membranes with tunable porous structure for equilibrium of breathable and waterproof performance, *Adv. Mater. Interfaces* 3 (2016) 1600516.
- 46- A.T. Servi, J. Kharraz, D. Klee, K. Notarangelo, B. Eyob, E. Guillen-Burrieza, A. Liu, H.A. Arafat, K.K. Gleason, A systematic study of the impact of hydrophobicity on the wetting of MD membranes, *J. Memb. Sci.* 520 (2016) 850–859.
- 47- A. Katsandri, A theoretical analysis of a spacer filled flat plate membrane distillation modules using CFD: part I: velocity and shear stress analysis, *Desalination* 408 (2017) 145–165.
- 48- X. Li, M.C. García-Payo, M. Khayet, M. Wang, X. Wang, Superhydrophobic polysulfone/polydimethylsiloxane electrospun nanofibrous membranes for water desalination by direct contact membrane distillation, *J. Memb. Sci.* 542 (2017) 308–319.
- 49- J. Cai, X. Liu, Y. Zhao, F. Guo, Membrane desalination using surface fluorination treated electrospun polyacrylonitrile membranes with nonwoven structure and quasi-parallel fibrous structure, *Desalination* 429 (2018) 70–75.
- 50- R. Ullah, M. Khraisheh, R.J. Esteves, J.T. McLeskey, M. AlGhouti, M. Gad-el-Hak, H.V. Tafreshi, Energy efficiency of direct contact membrane distillation, *Desalination* 433 (2018) 56–67.
- 51- A. Moghadam, S.H. Yousefi, H. V. Tafreshi, and B. Pourdeyhimi, Characterizing Nonwoven Materials via Realistic Microstructural Modeling, *Separation and Purification Technology*, 211 (2019) 602-609.
- 52- M.A. Samaha, H.V. Tafreshi, M. Gad-el-Hak, Sustainability of superhydrophobicity under pressure, *Phys. Fluids* 24 (2012) 112103.
- 53- Brakke KA, *Experimental Mathematics* 1992, 1, 141– 165.
- 54- D.J. Hornbaker, R. Albert, I. Albert, A.L. Barabási, P. Schiffer, What keeps sandcastles standing? *Nature* 387, 6635 (1997) 765.
- 55- C. Delaunay, Sur la Surface de Révolution dont la Courbure Moyenne est Constante, *J. Math. Pures Appl.* 6 (1841) 309–314.
- 56- W.C. Carter, The forces and behavior of fluids constrained by solids, *Acta Metall.* 36 (1988) 2283-2292.

- 57- Y. Wang, S. Michielsen, H.J. Lee, Symmetric and asymmetric capillary bridges between a rough surface and a parallel surface, *Langmuir* 29 (2013) 11028-11037.
- 58- F.M. Orr, L.E. Scriven, A.P. Rivas, Pendular rings between solids: meniscus properties and capillary force, *J. Fluid Mech.* 67 (1975) 723-742.
- 59- D.N. Mazzone, G.I. Tardos, R. Pfeffer, The effect of gravity on shape and strength of a liquid bridge between two spheres, *J. Colloid Interface Sci.* 113 (1986) 544-556.
- 60- C.D. Willet, M.J. Adams, S.A. Johnson, J.P.K. Seville, Capillary Bridges between Two Spherical Bodies, *Langmuir* 2000, 16, 9396-9405.
- 61- M.J. Adams, S.A. Johnson, J.P.K. Seville, C.D. Willett, Mapping the influence of gravity on pendular liquid bridges between rigid spheres, *Langmuir* 18 (2002) 6180-6184.
- 62- A. Virozub, N. Haimovich, S. Brandon, Three-dimensional simulations of liquid bridges between two cylinders: Forces, energies, and torques, *Langmuir*, 25 (2009) 12837–12842.
- 63- X.F. Wu, A. Bedarkar, K.A. Vaynberg, Droplets wetting on filament rails: surface energy and morphology transition, *J. Colloid Interface Sci.* 341 (2010) 326–332.
- 64- J.P. Oliver, C. Huh, S.G. Mason, An experimental study of some effects of solid surface roughness on wetting, *Colloids and Surfaces* 1 (1980) 79-104.
- 65- E.L. Decker, B. Frank, Y. Suo, S. Garoff, Physics of contact angle measurement, *Colloids Surf. A* 156 (1999) 177–189.
- 66- H. Chen, A. Amirfazli, T. Tang, Modeling Liquid Bridge between Surfaces with Contact Angle Hysteresis, *Langmuir* 29 (2013) 3310-3319.
- 67- H. Chen, T. Tang, A. Amirfazli, Liquid transfer mechanism between two surfaces and the role of contact angles, *Soft matter* 10 (2014) 2503-2507.
- 68- H. Chen, T. Tang, H. Zhao, K.Y. Law, A. Amirfazli, How pinning and contact angle hysteresis govern quasi-static liquid drop transfer, *Soft Matter* 12 (2016) 1998-2008.
- 69- A. Fall, B. Weber, M. Pakpour, N. Lenoir, N. Shahidzadeh, J. Fiscina, C. Wagner, and D. Bonn, Sliding Friction on Wet and Dry Sand *Phys. Rev. Lett.* 112, 175502.
- 70- B.J. Mullins, R.D. Braddock, G. Kasper, Capillarity in fibrous filter media: relationship to filter properties, *Chem. Eng. Sci.* 62 (2007) 6191–6198.
- 71- D. Kampa, S. Wurster, J. Buzengeiger, J. Meyer, G. Kasper, Pressure drop and liquid transport through coalescence filter media used for oil mist filtration, *Int. J. Multiph. Flow* 58 (2014) 313–324.

- 72- S.U. Patel, G.G. Chase, Separation of water droplets from water in-diesel dispersion using superhydrophobic polypropylene fibrous membranes, *Sep. Purif. Technol.* 126 (2014) 62–68.
- 73- P.S. Kulkarni, S.U. Patel, S.U. Patel, G.G. Chase, Coalescence filtration performance of blended microglass and electrospun polypropylene fiber filter media, *Sep. Purif. Technol.* 124 (2014) 1.
- 74- Y. Wu, G.M. Manzo, G.G. Chase, Thickness shrinkage of microfiber media in gas liquid coalescence filtration, *Sep. Purif. Technol.* 141 (2015) 188–196.
- 75- D.A. Lockington, J.Y. Parlange, M. Lenkopane, Capillary absorption in porous sheets and surfaces subject to evaporation, *Transp. Porous Media* 68 (2007) 29–36.
- 76- V.F. Cotorobai, I. Zgura, M. Birzu, S. Frunza, L. Frunza, Wicking behavior of fabrics described by simultaneous acquiring the images of the wet region and monitoring the liquid weight, *Colloids Surf. A* 497 (2016) 146–153.
- 77- Q. Wang, B. Maze, H.V. Tafreshi, B. Pourdeyhimi, A case study of simulating submicron aerosol filtration via spun-bonded filter media, *Chem. Eng. Sci.* 61 (2006) 4871–4883.
- 78- Q. Wang, B. Maze, H.V. Tafreshi, B. Pourdeyhimi, Simulating through-plane permeability of fibrous materials having different fiber lengths, *Modeling Simul. Mater. Sci. Eng.* 15 (2007) 855–868.
- 79- M.A. Tahir, H.V. Tafreshi, Influence of fiber orientation on the transverse permeability of fibrous media, *Phys. Fluids* 21 (2009) 083604.
- 80- S. Fotovati, H.V. Tafreshi, B. Pourdeyhimi, Influence of fiber orientation distribution on performance of aerosol filtration media, *Chem. Eng. Sci.* 65 (2010) 5285–5293.
- 81- S.A. Hosseini, H.V. Tafreshi, 3-D simulation of particle filtration in electrospun nanofibrous filters, *Powder Technol.* 201 (2010) 153–160.
- 82- A.M. Saleh, S.A. Hosseini, H.V. Tafreshi, B. Pourdeyhimi, 3-D microscale simulation of dust-loading in thin flat-sheet filters: a comparison with 1-d macroscale simulations, *Chem. Eng. Sci.* 99 (2013) 284–291.
- 83- C. Yue, Q. Zhang, Z. Zhai, Numerical simulation of the filtration process in fibrous filters using CFD-DEM method, *J. Aerosol Sci.* 101 (2016) 174–187.
- 84- K. Rezk, J. Forsberg, L. Nilsson, J. Berghel, Characterizing flow resistance in 3- dimensional disordered fibrous structures based on Forchheimer coefficients for a wide range of Reynolds numbers, *Appl. Math. Model.* 40 (2016) 8898–8911.
- 85- K. Nakamura, T. Suda, K. Matsumoto, Characterization of pore size distribution of non-woven fibrous filter by inscribed sphere within 3D filter model, *Sep. Purif. Technol.* 197 (2018) 289–294.

- 86- A. Ashari, H.V. Tafreshi, General capillary pressure and relative permeability expressions for through-plane fluid transport in thin fibrous sheets, *Colloids Surf. A* 346 (2009) 114–122.
- 87- A. Ashari, T.M. Bucher, H.V. Tafreshi, M.A. Tahir, M.S.A. Rahman, Modeling fluid absorption in thin fibrous sheets: effects of fiber orientation, *Int. J. Heat Mass Transfer* 53 (2010) 1750–1758.
- 88- M.A. Tahir, H.V. Tafreshi, S.A. Hosseini, B. Pourdeyhimi, Modeling the role of microstructural parameters in radiative heat transfer through disordered fibrous media, *Int. J. Heat Mass Transfer* 53 (2010) 4629–4637.
- 89- R. Arambakam, H.V. Tafreshi, B. Pourdeyhimi, Modeling performance of multicomponent fibrous insulations against conductive and radiative heat transfer, *Int. J. Heat Mass Transfer* 71 (2014) 341–348.
- 90- R. Arambakam, H.V. Tafreshi, B. Pourdeyhimi, A simple simulation method for designing fibrous insulation materials, *Mater. Des.* 44 (2013) 99–106.
- 91- X. Hou, M. Acar, V.V. Silberschmidt, Finite element simulation of low-density thermally bonded nonwoven materials: effects of orientation distribution function and arrangement of bond points, *Comput. Mater. Sci.* 50 (2011) 1292–1298.
- 92- G. Gaiselmann, R. Thiedmann, I. Manke, W. Lehnert, V. Schmidt, Stochastic 3D modeling of fiber-based materials, *Comput. Mater. Sci.* 59 (2012) 75–86.
- 93- B. Sabuncuoglu, M. Acar, V.V. Silberschmidt, Finite element modelling of fibrous networks: analysis of strain distribution in fibers under tensile load, *Comput. Mater. Sci.* 79 (2013) 143–158.
- 94- S. Abishek, A.J.C. King, R. Mead-Hunter, V. Golkarfard, W. Heikamp, B.J. Mullins, Generation and validation of virtual nonwoven, foam and knitted filter (separator/ coalescer) geometries for CFD simulations, *Sep. Purif. Technol.* 188 (2017) 493–507.
- 95- H. Altendorf, D. Jeulin, Random-walk-based stochastic modeling of three-dimensional fiber systems, *Phys. Rev. E* 83 (2011) 041804.
- 96- G. Gaiselmann, C. Tötze, I. Manke, W. Lehnert, V. Schmidt, 3D microstructure modeling of compressed fiber-based materials, *J. Power Sources* 257 (2014) 52–64.
- 97- L. Chapelle, M. Lévesque, P. Brøndsted, M.R. Foldschack, Y. Kusano, Generation of non-overlapping fiber architecture, *Proceedings of the 20th International Conference on Composite Materials*, (2015).
- 98- X. Huang, Q. Zhou, J. Liu, Y. Zhao, W. Zhou, D. Deng, 3D stochastic modeling, simulation and analysis of effective thermal conductivity in fibrous media, *Powder Technol.* 320 (2017) 397–404.

- 99- S. Jaganathan, H.V. Tafreshi, B. Pourdeyhimi, A realistic approach for modelling permeability of fibrous media: 3-D imaging coupled with CFD simulation, *Chem. Eng. Sci.* 63 (2008) 244–252.
- 100- S. Jaganathan, H.V. Tafreshi, B. Pourdeyhimi, Modeling liquid porosimetry in modelled and imaged 3-D fibrous microstructures, *J. Colloid Interface Sci.* 326 (2008) 166–175.
- 101- W. Sambaer, M. Zatloukal, D. Kimmer, 3D modeling of filtration process via polyurethane nanofiber based nonwoven filters prepared by electrospinning process, *Chem. Eng. Sci.* 66 (4) (2011) 613–623.
- 102- K. Schladitz, S. Peters, D. Reinel-Bitzer, A. Wiegmann, J. Ohser, Design of acoustic trim based on geometric modeling and flow simulation for nonwoven, *Comput. Mater. Sci.* 38 (2006) 56–66.
- 103- M.J. Lehmann, J. Weber, A. Kilian, M. Heim, Microstructure simulation as part of fibrous filter media development processes – from real to virtual media, *Chem. Eng. Technol.* 39 (2016) 403–408.
- 104- C. Delisee, J. Lux, J. Malvestio, 3D morphology and permeability of highly porous cellulosic fibrous material, *Transp. Porous Med.* 83 (2010) 623–636.
- 105- X. Huang, Y. Zhao, H. Wang, H. Qin, D. Wen, W. Zhou, Investigation of transport property of fibrous media: 3D virtual modeling and permeability calculation, *Eng. Comput.* 33 (2017) 997–1005.
- 106- D.G. Venkateshan, M.A. Tahir, H.V. Tafreshi, B. Pourdeyhimi, Modeling effects of fiber rigidity on thickness and porosity of virtual electrospun mats, *Mater. Des.* 96 (2016) 27–35.
- 107- R. Lucas, Rate of capillary ascension of liquids, *Kolloid Z.* 23 (1918) 15–22.
- 108- E. Washburn, The dynamics of capillary flow, *Phys. Rev.* 17 (1921) 273–283.
- 109- A. Marmur, R.D. Cohen, Characterization of porous media by the kinetics of liquid penetration: the vertical capillaries model, *J. Colloid Interface Sci.* 189 (2) (1997) 299–304.
- 110- A. Hamraoui, T. Nylander, Analytical approach for the Lucas-Washburn equation, *J. Colloid Interface Sci.* 250 (2) (2002) 415–421.
- 111- M. Gombia, V. Bortolotti, R.J.S. Brown, M. Camaiti, P. Fantazzini, Models of water imbibition in untreated and treated porous media validated by quantitative magnetic resonance imaging, *J. Appl. Phys.* 103 (2008) 094913.
- 112- J.R. Philip, Flow in porous media, *Annu. Rev. Fluid Mech.* 2 (1970) 177–204.
- 113- N. Mao, S.J. Russell, Anisotropic liquid absorption in homogeneous two-dimensional nonwoven structures, *J. Appl. Phys.* 94 (6) (2003) 4135–4138.

- 114- J. Hyvaluoma, P. Raiskinmaki, A. Jasberg, A. Koponen, M. Kataja, J. Timonen, Simulation of liquid penetration in paper, *Phys. Rev. E* 73 (2006) 036705.
- 115- M. Hadavand, A. Nabovati, A.C.M. Sousa, Ferrofluid permeation into three-dimensional random porous media: a numerical study using the lattice Boltzmann method, *Transp. Porous Med.* 99 (2013) 191–206.
- 116- A. Ferrari, I. Lunati, Direct numerical simulations of interface dynamics to link capillary pressure and total surface energy, *Adv. Water Resour.* 57 (2013) 19–31.
- 117- N.K. Palakurthi, S. Konangi, U. Ghia, K. Comer, Micro-scale simulation of unidirectional capillary transport of wetting liquid through 3D fibrous porous media: estimation of effective pore radii, *Int. J. Multiph. Flow* 77 (2015) 48–57.
- 118- H. Fathi, A. Raouf, S.H. Mansouri, M.Th. van Genuchten, Effects of porosity and water saturation on the effective diffusivity of a cathode catalyst layer, *J. Electrochem. Soc.* 164 (4) (2017) F298–F305.
- 119- R.D. Hazlett, Simulation of capillary-dominated displacements in microtomographic images of reservoir rocks, *Transport Porous Med.* 20 (1995) 21–35.
- 120- M. Hilpert, C.T. Miller, Pore-morphology-based simulation of drainage in totally wetting porous media, *Adv. Water Resour.* 24 (2001) 243–255.
- 121- V.P. Schulz, J. Becker, A. Wiegmann, P.P. Mukherjee, C.-Y. Wang, Modeling of twophase behavior in the gas diffusion medium of PEFCs via full morphology approach, *J. Electrochem. Soc.* 154 (4) (2007) B419–B426.
- 122- T.M. Bucher, B. Emami, H.V. Tafreshi, M. Gad-el-Hak, G.C. Tepper, Resistance of nanoFibrous superhydrophobic coatings to hydrostatic pressure: the role of microstructure, *Phys. Fluids* 24 (2012) 022109.
- 123- A. Moghadam, M. Jamali, D.G. Venkateshan, H. Vahedi Tafreshi, B. Pourdeyhimi, A new approach to modeling liquid intrusion in hydrophobic fibrous membranes with heterogeneous wettabilities, *Colloids Surf. A* 558 (2018) 154–163.
- 124- T.M. Bucher, H.V. Tafreshi, Modeling air-water interface in disordered fibrous media with heterogeneous wettability, *Colloids Surf. A* 461 (2014) 323–335.
- 125- T.M. Bucher, M.M. Amrei, H.V. Tafreshi, Wetting resistance of heterogeneous superhydrophobic coatings with orthogonally layered fibers, *Surf. Coat. Technol.* 277 (2015) 117–127.
- 126- C. Raufaste, S. Cox, Deformation of a free interface pierced by a tilted cylinder: variation of the contact angle, *Colloids Surf. A* 438 (2013) 126–131.

- 127- S. Litster, D. Sinton, N. Djilali, Ex situ visualization of liquid water transport in PEM fuel cell gas diffusion layers, *J. Power Sources* 154 (2006) 95–105.
- 128- P.P. Mukherjee, C.-Y. Wang, Q. Kang, Mesoscopic modeling of two-phase behavior and flooding phenomena in polymer electrolyte fuel cells, *Electrochim. Acta* 54 (2009) 6861–6875.
- 129- L. Hao, P. Cheng, Lattice Boltzmann simulations of water transport in gas diffusion layer of a polymer electrolyte membrane fuel cell, *J. Power Sources* 195 (2010) 3870–3881.
- 130- F. Arbabi, H. Montazeri, R. Abouatallah, R. Wang, A. Bazylak, Three-dimensional computational fluid dynamics modelling of oxygen bubble transport in polymer electrolyte membrane electrolyzer porous transport layers, *J. Electrochem. Soc.* 163 (11) (2016) F3062–F3069.
- 131- Y. Gao, A. Montana, F. Chen, Evaluation of porosity and thickness on effective diffusivity in gas diffusion layer, *J. Power Sources* 342 (2017) 252–265.
- 132- S.S. Rajgarhia, S.C. Jana, G.G. Chase, Separation of water from ultralow sulfur diesel using novel polymer nanofiber-coated glass fiber media, *ACS Appl. Mater. Interfaces* 8 (2016) 21683–21690.
- 133- Y. Yu, H. Chen, Y. Liu, V.S.J. Craig, Z. Lai, Selective separation of oil and water with mesh membranes by capillarity, *Adv. Colloid Interface Sci.* 235 (2016) 46–55.
- 134- M.L. Porter, M.G. Schaap, D. Wildenschild, Lattice-Boltzmann simulations of the capillary pressure–saturation–interfacial area relationship for porous media, *Adv. Water Resour.* 32 (2009) 1632–1640.
- 135- V.P. Schulz, E.A. Wargo, E.C. Kumbur, Pore-morphology-based simulation of drainage in porous media featuring a locally variable contact angle, *Transport Porous Med.* 107 (1) (2015) 13–25.
- 136- B. Emami, H.V. Tafreshi, Optimizing fiber cross-sectional shape for improving stability of air–water interface over superhydrophobic fibrous coatings, *Appl. Phys. Lett.* 100 (2012) 193104.
- 137- M. Cieplak, M.O. Robbins, Influence of contact angle on quasi-static fluid invasion of porous media, *Phys. Rev. B* 41 (16) (1990) 11508.
- 138- O. Chapuis, M. Prat, M. Quintard, E. Chane-Kane, O. Guillot, N. Mayer, Two-phase flow and evaporation in model fibrous media application to the gas diffusion layer of PEM fuel cells, *J. Power Sources* 178 (2008) 258–268.
- 139- H. Chraïbi, M. Prat, O. Chapuis, Influence of contact angle on slow evaporation in two-dimensional porous media, *Phys. Rev. E* 79 (2009) 026313.

- 140- R. Holtzman, E. Segre, Wettability stabilizes fluid invasion into porous media via nonlocal, cooperative pore filling, *Phys. Rev. Lett.* 115 (2015) 164501.
- 141- K.A. Brakke, *Surface Evolver Manual*, Version 2.70, (2013).
- 142- D.G. Venkateshan, M.M. Amrei, A.A. Hemeda, Z. Cullingsworth, J. Corbett, H.V. Tafreshi, *Colloids Surf. A* 511 (2016) 247–254.
- 143- J. Lee, Y. Lu, S. Kashyap, A. Alarmdari, Md.O.F. Emon, J-W Choi, Liquid bridge microstereolithography, *Additive Manufacturing* 21 (2018) 76-83.
- 144- M.D. Dickey, A. Raines, E. Collister, R.T. Bonnecaze, S.V. Sreenivasan, C.G. Willson, High-aspect ratio polymeric pillar arrays formed via electrohydrodynamic patterning, *J. Mater. Sci.* 43 (2008) 117–122.
- 145- J.M. Gac, A. Jackiewicz, L. Werner, S. Jakubiak, Consecutive filtration of solid particles and droplets in fibrous filters, *Separation and Purification Technology* (2016), 234–240.
- 146- R. Finn, Capillary surface interfaces, *Not AMS* 46 (1999) 770–781.
- 147- M.A. Fortes, Axisymmetric liquid bridges between parallel plates, *J. Colloid Interface Sci.* 88 (1982) 338-352.
- 148- E.J. De Souza, L. Gao, T.J. McCarthy, E. Arzt, A.J. Crosby, Effect of Contact Angle Hysteresis on the Measurement of Capillary forces, *Langmuir* 24 (2008), 1391–1396.
- 149- E.J. De Souza, M. Brinkmann, C. Mohrdieck, A. Crosby, E. Arzt, Capillary forces between chemically different substrates, *Langmuir* 24 (2008) 10161–10168.
- 150- E.J. De Souza, M. Brinkmann, C. Mohrdieck, E. Arzt, Enhancement of capillary forces by multiple liquid bridges, *Langmuir* 24 (2008) 8813-8820.
- 151- A.L. Yarin A.L. B. Pourdeyhimi, S. Ramakrishna, *Fundamentals and Applications of Micro and Nanofibers*; Cambridge University Press: Cambridge, 2014.
- 152- S.H. Yousefi, H. Vahedi Tafreshi, Modeling electrospun fibrous structures with embedded spacer particles: Application to aerosol filtration, *Separation and Purification Technology* 235 (2020) 116184.
- 153- S.H. Yousefi, C. Tang, H. Vahedi Tafreshi, B. Pourdeyhimi, Empirical model to simulate morphology of electrospun polycaprolactone mats, *Journal of Applied Polymer Science* 136, no. 46 (2019) 48242.
- 154- S.H. Yousefi, D.G. Venkateshan, C. Tang, H.V. Tafreshi, B. Pourdeyhimi, Effects of electrospinning conditions on microstructural properties of polystyrene fibrous materials, *J. Appl. Phys.* 124 (2018) 235307.

- 155- N. Ojaghlo, H.V. Tafreshi, D. Bratko, A. Luzar, Dynamical Insights into the Mechanism of a Droplet Detachment from a Fiber, *Soft Matter* 14 (44) 8924-8934.
- 156- M. Shafiei, N. Ojaghlo, S.G. Zamfir, D. Bratko, A. Luzar, Modulation of structure and dynamics of water under alternating electric field and the role of hydrogen bonding, *Molecular Physics* 117,22 (2019) 3282–3296.
- 157- M.E. Foulaadvand, N. Ojaghlo, Structural and elastic properties of a confined two-dimensional colloidal solid: A molecular dynamics study, *Physical Review E* 86 (2), 021405
- 158- H. Aziz, H.V. Tafreshi, Competing forces on a liquid bridge between parallel and orthogonal dissimilar fibers, *Soft Matter* 15 (2019) 6967-6977.
- 159- M. Jamali, H. Vahedi Tafreshi, B. Pourdeyhimi, Droplet mobility on hydrophobic fibrous coatings comprising orthogonal fibers, *Langmuir* 34 (2018) 12488-12499.
- 160- B. Qian, K.S. Breuer, The motion, stability and breakup of a stretching liquid bridge with a receding contact line, *J. Fluid Mech.* 666 (2011) 554–572.
- 161- B. Emami, A.A. Hemedi, M.M. Amrei, A. Luzar, M. Gad-el-Hak, H.V. Tafreshi, Predicting Longevity of Submerged Superhydrophobic Surfaces: Surfaces with Parallel Grooves, *Phys. Fluids* 25 (2013) 062108.
- 162- H. Aziz, H. Vahedi Tafreshi, Role of particles spatial distribution in drag reduction performance of superhydrophobic granular coatings, *International Journal of Multiphase Flow* 98 (2018) 128-138.
- 163- M.A. Samaha, H.V. Tafreshi, M. Gad-el-Hak, In situ, noninvasive characterization of superhydrophobic coatings, *Review of Scientific Instruments* (2011), 045109.
- 164- F.O. Ochanda, M.A. Samaha, H.V. Tafreshi, G.C. Tepper, M. Gad-el-Hak, Fabrication of Superhydrophobic Fiber Coatings by DC-Biased AC-Electrospinning, *Journal of Applied Polymer Science* (2012), 1112-1119.
- 165- H. Aziz, M.M. Amrei, A. Dotivala, C. Tang, H.V. Tafreshi, Modeling Cassie droplets on superhydrophobic coatings with orthogonal fibrous structures, *Colloids Surf. A* 512 (2017) 61-70.
- 166- H. Aziz, N.M. Farhan, H.V. Tafreshi, Effects of fiber wettability and size on droplet detachment residue, *Experiments in Fluids*, 59, 7 (2018) 122.
- 167- N.M. Farhan, H. Aziz, H. Vahedi Tafreshi, Simple method for measuring intrinsic contact angle of a fiber with liquids, *Experiments in Fluids*, 60, 5 (2019) 87.
- 168- M. Jamali, A. Moghadam, H. Vahedi Tafreshi, B. Pourdeyhimi, Droplet adhesion to hydrophobic fibrous surfaces, *Applied Surface Science* 456 (2018) 626-636.

169- N.M. Farhan, H. Vahedi Tafreshi, Universal expression for droplet–fiber detachment force, *J. Appl. Phys.* 124 (2018) 075301.

170- N.M. Farhan, H. Vahedi Tafreshi, Using magnetic field to measure detachment force between a nonmagnetic droplet and fibers, *Langmuir* 35 (2019) 8490-8499.

## Appendix A: Vita

### Ali Moghadam

PhD Candidate

Mechanical and Nuclear Engineering Department, Virginia Commonwealth University

Office: 804-827-2029; Cell: 718-781-2033; Email: [moghadama@vcu.edu](mailto:moghadama@vcu.edu)

#### EDUCATION

- **PhD, Mechanical & Nuclear Engineering** (2016–2019)  
Virginia Commonwealth University  
GPA: 4 out of 4
- **MS, Mechanical Engineering** (2013–2016)  
University of Tehran, Tehran, Iran  
GPA: 18.07 out of 20
- **BS, Mechanical Engineering** (2002–2006)  
Amirkabir University of Technology (Tehran Polytechnic), Tehran, Iran  
GPA: 17.05 out of 20

#### WORK EXPERIENCE

- **Graduate Research Assistant**, VCU, Richmond VA, USA (2016–2019)
- **Researcher**, Nonwovens Institute, Raleigh, NC, USA (2016–2019)
- **Graduate Teaching Assistant**, VCU, Richmond VA, USA (Jan. 2019–Dec. 2019)
- **Research/Teaching Assistant**, University of Tehran, Tehran, Iran (2013–2016)

#### RESEARCH INTERESTS AND ACTIVITIES

- Porous Media and Multiphase Flow
- Computational Fluid Dynamics
- Interfacial Phenomena

#### SKILLS

- **Computer Programming:** FORTRAN, C, PYTHON, MATLAB, Mathematica
- **Engineering Software:** Surface Evolver, ANSYS Fluent, ANSYS DesignModeler
- **Experimental:** High-speed imaging and image processing, Surface characterization, Data acquisition
- **General:** MS Office, Tecplot

#### PEER-REVIEWED JOURNAL PUBLICATIONS

- **A. Moghadam**, S.H. Yousefi, H. V. Tafreshi, and B. Pourdeyhimi, Characterizing Nonwoven Materials via Realistic Microstructural Modeling, *Separation and Purification Technology*, 211,602 (2019).

- **A. Moghadam**, M. Jamali, H.V. Tafreshi, and B. Pourdeyhimi, A New Approach to Modeling Liquid Intrusion in Hydrophobic Fibrous Membranes with Heterogeneous Wettabilities, *Colloids and Surfaces A*, 558, 154 (2018).
- M. Jamali, **A. Moghadam**, H.V. Tafreshi and B. Pourdeyhimi, Droplet Adhesion to Hydrophobic Fibrous Surfaces, *Applied Surface Science*, 456, 626 (2018).
- **A. Moghadam** and H.V. Tafreshi, On Liquid Bridge Adhesion to Fibrous Surfaces under Normal and Shear Forces (Under review).

#### **SELECTED CONFERENCES AND WORKSHOPS**

1. **A. Moghadam**, H.V. Tafreshi, B. Pourdeyhimi, Characterizing Nonwoven Fibrous Materials via Realistic Microstructural Simulation, American Filtration and Separations Society (AFS), April 01-04 (2019), Cherry Hill, NJ, USA.

#### **GRADUATE COURSEWORK**

##### **University of Tehran, Iran**

Continuum Mechanics, Advanced Fluid Mechanics, Advanced Thermodynamics, Advanced Numerical Methods, Computational Fluid Dynamics, Conductive Heat Transfer.

##### **Virginia Commonwealth University, USA**

Topics in Nuclear Engineering, Mechanical and Nuclear Engineering Materials, Heat and Mass Transfer.2